USING INSAR AND CLOSURE PHASE TO MEASURE CHANGING SOIL MOISTURE, VEGETATION MOISTURE, AND PERMAFROST

A DISSERTATION
SUBMITTED TO THE DEPARTMENT OF ELECTRICAL ENGINEERING
AND THE COMMITTEE ON GRADUATE STUDIES
OF STANFORD UNIVERSITY
IN PARTIAL FULFILLMENT OF THE REQUIREMENTS
FOR THE DEGREE OF
DOCTOR OF PHILOSOPHY

Elizabeth Paige Wig
December 2025

Epigraph

Despite all our accomplishments, we owe our existence to a six-inch layer of topsoil and the fact it rains.

Paul Harvey, radio broadcaster

Abstract

Characterizing changing moisture in soil and vegetation is the key to understanding a number of processes: optimizing irrigation for agriculture, managing and mitigating wildfire risk, characterizing permafrost dynamics, ensuring infrastructure stability, monitoring floods and droughts, and improving models of hydrology and climate. Point measurements of soil moisture are common, but the spatial coverage of these sensors is sparse. Measurements of vegetation moisture are even rarer and often require labor-intensive cuttings sampling vegetation and drying it in ovens. Meanwhile, the most prevalent remote sensing of moisture from space comes from radiometer measurements, whose coarse resolution cells cover tens of kilometers, missing the nuances of spatially heterogeneous environments. Therefore, a way to measure moisture at fine resolution would be valuable.

Moisture changes have been a nuisance measurement for scientists measuring deformation of the Earth using interferometric synthetic aperture radar (InSAR). InSAR interferes two synthetic aperture radar images of the same area at different times, and the phase difference between the images can measure ground deformation. Radar signals are very sensitive to water, and when moisture changes, the scattering from the ground surface, vegetation canopy, and ground subsurface change – sometimes appearing to look like deformation. We can isolate this signal by calculating a quantity called the InSAR closure phase. In this thesis, I show that we can model InSAR closure phase simply with a two-layer scattering model. I show that, using this model, we can predict that moisture that changes asymmetrically in time will lead to an apparent bias in the InSAR interferometric and closure phase and a trend in the cumulative phase. Such asymmetric moisture changes can arise from rainfall over soil that slowly dries down, or from increasing moisture stored in plants above the soil that is removed quickly due to a harvest or leaf-fall. I show that we can estimate changing moisture using a cumulative sum of the modeled data.

I then validate this model using real soil moisture data and show that we can estimate soil moisture in situ from cumulative InSAR closure phase. I examine a large test region in Oklahoma, where the detrended cumulative closure phase from Sentinel-1 data demonstrates some agreement with in situ soil moisture measurements. The fit across these validation sites can then be used to validate soil moisture across the entire swath. While the match between cumulative closure phase and soil moisture is strong at many sites, some have a weaker match, implying a terrain dependence

on the quality of fit. This terrain dependence may be largely dependent on overlying vegetation.

To explore this question further, I next compare cumulative closure phase measurements with in situ measurements of moisture in vegetation. I use partial correlations to show that changing soil and vegetation dielectric constant can both control the closure phase, suggesting that in some places the closure phase signal may be dominated by soil moisture, while in other places it may be dominated by vegetation.

Wildfires are increasing in frequency and intensity, putting lives, infrastructure, and environments at risk. Gridded wildfire fuel moisture data would help with management and mitigation of wildfires. Here, I show some progress towards making gridded wildfire fuel moisture using InSAR closure phase, showing that at one test site, the fuel moisture can be found from a combination of the in situ soil moisture and the closure phase.

One important application of soil moisture is measurement of permafrost. In permafrost, the active layer thickness (ALT) is defined as the maximum summer thaw depth, and is important to measure to quantify carbon emissions from permafrost, to understand the effects of permafrost thaw and displacement on infrastructure, and to understand ecosystem change in this rapidly changing environment. Permafrost active layer thickness can be measured through an inversion of soil moisture and seasonal subsidence, both of which can be measured with InSAR. In this thesis, I interpret a data set of permafrost seasonal subsidence, active layer thickness, soil moisture, and water table depth, from an airborne mission looking at seasonal change over 63 swaths in the North American Arctic-Boreal region. Lower soil volumetric water content associated with deeper active layers suggests that Arctic soil may become drier as the climate warms. Burned areas have higher soil water content than unburned areas. Greening trends appear associated with smaller seasonal subsidence, thinner active layers, and wetter soil.

Finally, looking to the future, I discuss mission requirements for future repeat-pass InSAR missions. Permafrost is a unique environment: very spatially heterogeneous, with consistent seasonal surface displacement alongside long-term trends, with few stable reference points. As a result, InSAR missions optimized to study permafrost will need to address its unique needs.

This thesis is thematically concerned with a few ideas: first, that simple models of electromagnetic wave propagation can uncover subtle and complex emergent characteristics of remotely sensed materials; second, that one researcher's noise is another's signal; and finally, that InSAR is a tool not only for the static, solid Earth, but for the various ecosystems, soil, and vegetation cover that lie between a radar in space and the bedrock.

Acknowledgments

A Ph.D. is often considered a lonely or solitary experience, and I am fortunate that my experience was the opposite: my time in this program has been full of wonderful people and communities, and I feel very lucky to have shared this time with them. I am so grateful for all the people who were generous with their time, knowledge, and resources to help me throughout this endeavor.

Thank you to my parents, the Drs. Jennifer and Timothy Wig, for always encouraging me develop new skills and knowledge. Thank you to my husband, Zach, for all your support throughout this PhD, culinary and otherwise. Thanks, too, to my sisters, grandparents, and extended family on Taira and Wig sides for their support. Thank you to all the friends I've made throughout the PhD program: in the Geophysics and Electrical Engineering departments, in the Women in EE club, at the climbing wall, and around campus. Thanks especially to Julia Costacurta and Laura Blackstone for being my go-to support system for all the ups and downs of grad school. And to the WEE friends (Cassandra, Michelle, Geneva), outdoor adventure buddies (Zoe, Sonia, Jenny, Skyler, Carson, Cait, Garett, Mitchell, Sam), Epigraph book club (Elliot, Rachael, Yasmine, Christina, Claire), and longtime friends (Lauren, Steph, Damla, Perri, Ted, Sofia). Thank you to friends within Stanford's geophysics and electrical engineering department who have made this community so wonderful: Matt Lees, Aakash Ahamed, Mike Morphew, Javier Peralta, Sylvia Zhang, Rishudh Thakur, Johnny Mells; Thomas Teisberg, Nicole Bienert, Riley Culberg, Sean Peters, Danny May, Natalie Wolfenbarger, Sunme Zhao, Olivers Pranis, Jordan Tucker, Annie Cheng, Michelle Park; Taiyi Wang, Rebeca Ursu, Eric Berg; Paul Summers; Paige Given; William Meng, Shubo Yang; and many more friends who have made the community a home. I would also like to thank the administrative staff within both departments for all their help with the logistical side of study: Jeremy Samos (especially for the geography games), Liliane Pereira, Ros McCambridge, Meo Kittiwanich.

Thank you to Stacey Huang and Karissa Pepin for helping me to learn about the joys and struggles of processing InSAR when I first joined the group. Thanks to my later labmates for your friendship and for broadening my horizons through the new directions you took: Farrah Harris, Arba Shkreli, Kate McCarthy, Sarina Kapai. Thanks to all my lab alumni and extended lab family for being a great community: Stacey, Karissa, Roger, Lauren, Yujie, Ann, Piyush, Shadi, Sang-Ho, Molly, Scott, Miranda, Khai Zher.

Thank you to the Arctic-Boreal Vulnerability Experiment (ABoVE) Permafrost Dynamics Observatory (PDO) team – Kevin Schaefer, Roger Michaelides, Richard Chen, Lingcao Huang, Leah Clayton, Mark Serreze, Andy Parsekian, Brittany Fager, Mia Yuhuan Zhao, Mahta Moghaddam, and Lin Liu, to name a few, for all your help with my work on permafrost. Your generosity in sharing your expertise is greatly appreciated.

Thank you the community at NASA JPL, especially to Paul Rosen, who organized the NISAR radar short course in fall 2023, and to Yunling Lou, Karen An, and Richard Chen, who hosted me for an internship in the summer of 2024. I'm also grateful for the broader community found through my time with JPL, with too many people to name here.

Thank you to Alex Konings, whose insights on remote sensing of hydrology taught me so much about the landscape of soil and vegetation moisture remote sensing and validation, and whose course was a favorite from my time at Stanford.

Thank you to Dusty Schroeder, who has been so generous in welcoming me into his research group and sharing insights into research and life alike during my time at Stanford. Your group has become a second home for me here.

Roger Michaelides deserves thanks in many of the above categories: as a mentor, lab alum, permafrost/InSAR/closure phase expert, and friend who took me under his wing in the weird remote days of the COVID-19 pandemic and helped me figure out more or less my entire PhD. Roger, I don't even know how to begin to thank you for all of your mentorship and support over the years. You are an inspiration, and I'm so excited to see everything your group does in the years to come.

Finally, I can't thank my advisor, Howard, enough. I have learned so much from Howard through his teaching and by example. Over time, I have only come to appreciate Howard more and more: his keen discernment of which research questions are most interesting to ask, his scientific insights into solving problems in the most simple yet elegant way possible, his ability to stay deeply involved in the technical aspects of research even while taking on significant responsibilities on large projects, his commitment to enabling his students to pursue whichever directions we are most interested in while also providing guidance when we get lost in the weeds, his door that is always open. Howard, I am so, so grateful to have had you as an advisor.

Funding: I'm grateful for fellowship support for graduate school through the National Defense Science and Engineering Grant and the Stanford Graduate Fellowship, especially Scott A. and Geraldine D. Macomber, who generously endowed my fellowship. My work has also been supported by NASA grant NNX17AC59A and by grants from the Stanford Woods Institute for the Environment.

Contents

List of Tables

List of Figures

Chapter 1

Introduction

Planet Earth is dynamic, from deformation of the Earth's crust to changes in its ecosystems. Understanding all the ways the earth is changing is important for all of us who make our home on Earth. In many cases, a changing planet has large effects on humans; in many cases, human activity changes the planet. These changes are myriad: global irrigation expands into water-stressed regions as droughts increase [139, 84]; extreme wildfires double in frequency and intensity [36]; thawing permafrost leads to ground subsidence and carbon release into the atmosphere [76, 117]. Moreover, these changes often are influenced by a similar interplay of basic phenomena. For example, all of these changes are affected by the amount of water stored in soil and vegetation. In the case of global agriculture, knowing soil moisture can better inform irrigation policies, enabling more responsible water usage and better crop yield. In the case of fire, dry vegetation catches fire more easily; measuring moisture of fire-prone areas can map which areas have highest risk, and knowing how moisture is changing on the ground is instrumental in this process. Permafrost changes in freeze/thaw are moderated by moisture stored in the soil [32] and by insulating vegetative layers above the ground. Measuring soil moisture, then, enables characterization of permafrost; characterizing soil and vegetation moisture alongside permafrost deformation can unlock insights into the ever-changing permafrost environment [27, 136].

InSAR (interferometric synthetic aperture radar) is a measurement tool uniquely capable of measuring minute changes on Earth's surface over time. Long used to study surface deformation due to earthquakes and volcanoes [21], InSAR has more recently been seen as a potential source of soil moisture measurements. While many research applications treat changing moisture on the ground as nuisance signal for surface deformation signals, soil and vegetation moisture measurement are of interest for a number of other applications. The goal of this dissertation, then, is to show that one person's noise is another's signal, and that the moisture signals within InSAR measurements can provide us with valuable information about changes on Earth's surface. The contributions to scientific knowledge center on isolating moisture through the calculation of InSAR closure phase to

measure moisture in soil and vegetation, with applications to wildfires, agriculture, and permafrost.

1.1 Contributions and Thesis Roadmap

The specific contributions of this thesis are as follows:

1. We present a simple SAR scattering model for closure phase arising from the interference of surface and subsurface scattering in a dielectric, and use this model to show that cumulative InSAR closure phase time series can be used to estimate soil moisture. We also show that this simple model predicts that asymmetric patterns of soil wetting and drying can lead to a long-term trend in closure phase, which would create a bias in InSAR time series. This is presented in Chapter 3.

2. We demonstrate that cumulative InSAR closure phase time series can be used to estimate soil moisture, using 37 soil moisture stations in Oklahoma for validation. This is presented in Chapter 4.

3. We show that cumulative InSAR closure phase can likewise be used to estimate vegetative moisture content, both in the context of vegetation dielectric constant (Chapter 5) and vegetative fuel moisture (Chapter 6).

4. We interpret results from a large-scale L-band InSAR survey of permafrost, which used remotely sensed soil moisture and land subsidence to derive permafrost soil moisture, seasonal subsidence, and active layer thickness. We discuss how these variables relate to other permafrost characteristics, such as vegetation greening and browning, land cover, and wildfire recovery, and how this can inform our understanding of changing permafrost landscapes (Chapter 7).

Chapter 2

Background on Radar

We would like to be able to map the world from space using radar. In this section, we provide a conceptual overview of radar, synthetic aperture radar (SAR), and interferometric synthetic aperture radar (InSAR), as well as of wave scattering through common media encountered by radar waves[1].

2.1 Radar

The term "radar" originated to describe RAdio Detection And Ranging, a method of detecting and determining the range and direction of objects' reflections from transmitted radio waves. Originally invented around the time of the Second World War, radar has found applications far beyond its original military use cases.

A basic radar system can be conceptualized as in Figure 2.1. A transmitter produces a waveform at a radio or microwave frequency (this waveform has transmit power P_T). This waveform can represent a constant or varying frequency. The waveform is then passed to an antenna, which

[1] Unless otherwise specified, material in this section was derived from [124] and course notes from Stanford's EE258: Radar Remote Sensing course taught by Howard Zebker

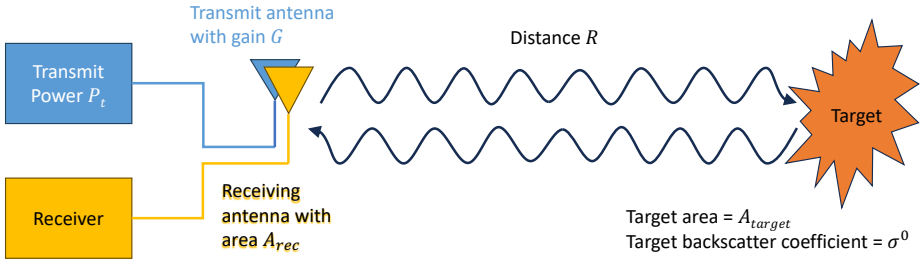

Figure 2.1: Block diagram of a simple radar system.

transmits the wave into its environment. The antenna focuses the wave to some degree (according to its gain G), and the wave propagates through the environment to a target of some sort, located at a distance R from the transmitter. Energy scatters from the target according to (1) its cross-sectional area from the view of the transmitter A_{target} and (2) its backscatter coefficient σ^0. The backscatter coefficient is determined largely by surface properties of the target, such as its shape or roughness. Some of the energy incident upon the target is scattered toward the radar receiver, which may be at the same or a different location than the transmitter. In Figure 2.1, the radar is monostatic, so its transmit and receive antenna are colocated. The antenna receives all of the signal that impinges on its area A_{rec}. From this signal path, we can derive the **radar equation**[2], which tells us how much power we receive (P_R) from the target using our radar system.

$$P_R = P_T G \frac{1}{4\pi R^2} A_{target} \sigma^0 \frac{1}{4\pi R^2} A_{rec} \tag{2.1}$$

A few insights become apparent from this equation. First, the distance of a target from a radar has a large impact on the strength of the radar signal. For a monostatic radar, the signal power decreases according to $\frac{1}{R^4}$. This is due to assumed spherical spreading of the radar wave from the transmit antenna and after scattering from the target. The spreading can be somewhat made up by having an antenna that focuses its signal well – i.e., that has a large gain:

$$G = \frac{4\pi A}{\lambda^2} \tag{2.2}$$

for antenna area A and radar wavelength λ.

A larger antenna area is therefore desirable for a more focused radar wave. The antenna's effective area, or effective aperture, is the area over which it is effectively collecting electromagnetic signals from its environment. In addition to the physical size of the antenna, effective area also accounts for the antenna's efficiency.

If we aim our radar at a target, we can therefore measure the power returned from that target. Aiming at a more reflective target will result in a "brighter" or more powerful return signal than at a less reflective target at the same distance. We can imagine that, if we have an antenna that focuses well, we can aim it at different small areas on a large surface and measure P_R at these different points to create a map of the surface. This map will tell us which areas of the surface are more and less reflective.

Unfortunately, it is rare that we are mapping a target in an isolated environment free of noise. The real world is full of signals at all frequencies, and as a result, our receiving antenna will pick up noise from the environment and from inside of the radar system, which can obscure the radar

[2]There is no singular radar equation; there can be many variations of "the radar equation" according to the design specifications of the radar system in question. Generally, a radar equation concerns itself with the relationship of the power received at a radar receiver to the power transmitted from the transmitter. This can depend on system and environmental parameters, including but not limited to system efficiencies, propagation spreading losses, and gains.

signal. In order to measure the strength of the signal, we compare the signal power to the power of the noise in the environment using the *signal-to-noise ratio*. When calculating the signal-to-noise ratio of a radar system, the received power P_R represents the signal strength. The noise inherent to the radar system N depends on the Boltzmann constant k, the system temperature T_{sys}, and the signal bandwidth B.

$$N = kT_{sys}B \tag{2.3}$$

The signal-to-noise ratio is then

$$SNR = \frac{P_R}{N} \tag{2.4}$$

and is often expressed in decibels, dB. A larger signal-to-noise ratio indicates that the return signal will be detected clearly by the radar system, while a smaller ratio indicates a weaker signal that may be obscured by the noise.

For a basic radar system on Earth trying to measure a target that is a short distance away, the factor of R^4 in the denominator of (2.1) may be moderately large (for example, R may be between several meters and several kilometers), but we can also build a large antenna to boost the gain, use a large power source, wide bandwidth, or low-temperature system, or adjust other parameters in the radar equation to achieve a good signal-to-noise ratio.

If, however, we wish to measure very distant targets, as is the case when mapping Earth from space or an aircraft, this calculus becomes more difficult. As the range increases to hundreds of kilometers or more, the signal power still decreases by R^4. We note that it is difficult to launch very large power sources or antennas into space.

This makes it challenging to use hardware alone to make a radar system with strong signals to measure Earth from space. Fortunately, hardware modification is not the only tool at our disposal. We will show that we can use clever signal processing to increase the signal strength beyond the capabilities of basic hardware, enabling us to make fine-resolution radar images from the air and space.

2.2 Radar Imaging

2.2.1 Radar Ranging, Resolution, and Pulse Compression

In the previous section, we discussed how the radar equation (2.1) can be used to calculate the power received from a target measured by a radar system. In addition to measuring the power received, we can also measure how long it takes for the radar wave to reach the target. We can then use this travel time τ to determine the distance to the target. In air or vacuum, the distance from a monostatic radar to a target is

$$R = \frac{c\tau}{2} \tag{2.5}$$

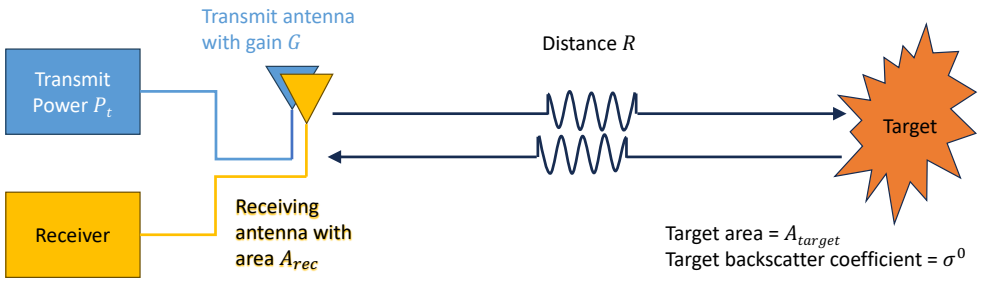

Figure 2.2: Pulsed radar system.

where c is the speed of light, and the factor of 2 accounts for two-way travel to and from the target.

If our radar is sending out a continuous wave (for example, a sine wave at a given frequency), it might be difficult to determine the time of flight. The radar is constantly transmitting at power P_T, a signal is constantly returning at power P_R, and which time of transmit corresponds to which time of return is ambiguous.

If, instead of transmitting a constant signal, we send a short pulse, it becomes easier to distinguish distance. We define a **pulse** as a signal sent for a fixed period of time. Figure 2.2 shows a radar sending a single, sinusoidal pulse toward a single target, which reflects the pulse back toward the receiver. For this single target, we can determine the distance to the target based on when the pulse returns.

However, if there are multiple targets within the radar field of view, this becomes a challenge: for example, if there is another target a short distance farther than the first, such that the returning pulses from the two targets overlap, it may be difficult to distinguish the number and distance of the targets. If we would like to eventually image an entire swath of the ground from the air or space, it will contain *many* targets, and there may be continuous responses from all of them. Disambiguating the overlapping, identically shaped sine waves from one target and another becomes a very challenging feat!

We can solve for the resolution in range by recognizing that we can't distinguish signals from overlapping pulses. Assuming we travel through free space, the wave speed is c, the speed of light. For a pulse of duration T traveling two ways (to and from the target), then, the ability to discriminate in range is designated as the resolution δ_r:

$$\delta_r = \frac{cT}{2} \tag{2.6}$$

This provides a source of motivation to be cleverer with our pulse processing: the goal is to be able to disambiguate a number of targets within the same scene. We would like to do this even if the targets are close to each other, so the returning pulses are overlapping. It may be advantageous, therefore, for our pulse to take a different form than a single, sinusoidal signal.

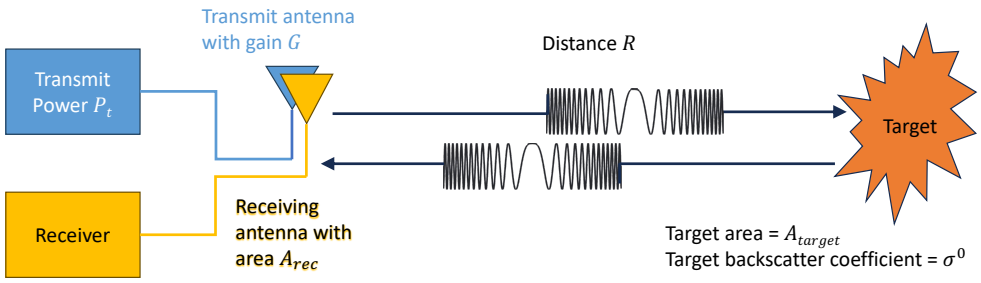

Figure 2.3: Chirped Radar System.

We can achieve this using a **chirp**, a signal that linearly changes in frequency over time. Figure 2.3 shows the radar system with a chirp waveform in place of the sinusoid.

A radar looking to the Earth will often point towards the ground at an angle, so there are points it illuminates at nearer and farther ranges. Figure 2.4 shows what happens when a radar sends a chirp to everything it illuminates in a beam. The wave that reaches the nearer section of ground returns earlier, and the chirp that illuminates the farther ground area from the radar returns later.

To be more specific, Fig. 2.3 and Fig. 2.4 show the real part of the chirped signal. The true radar signal is complex, containing both a real and imaginary part. A chirp signal s sent from the transmitter over time (t) can be defined as:

$$s(t) = e^{2\pi j f_c t + 2\pi j \alpha t^2}, |t| \leq \frac{T}{2} \tag{2.7}$$

for some center frequency of the radar f_c, mathematical constants e and π, imaginary constant j, pulse length T, and **chirp rate** or **chirp slope** α. The first part of this complex exponential, which is proportional to t, defines the carrier frequency around which the changing frequency of the chirp is centered. The second part, proportional to t^2, defines the rate of frequency change through the chirp. A larger chirp slope means a faster rate of change through the frequencies contained in the chirp. Typically, the chirp is bounded in time to sweep through a particular range of frequencies surrounding the center frequency.

Because the chirp is a complex signal, it has a constant amplitude (the absolute value of $s(t)$ is always 1). Taking the real and imaginary parts decomposes it into sine and cosine components.

We can disambiguate targets using this chirp signal through a process called **pulse compression**, which focuses the signal. Pulse compression is easiest to visualize as a time-domain convolution. If we split the chirp up into "bins" based on return time, with the first range bin coming from the start of the earliest return and the last bin from the end of the last return, we can add up the signal that returns within a given time and assign it to a bin, as shown in step 7 of Fig. 2.4.

Figure 2.5 shows a conceptual visualization of how pulse compression functions in the range direction for a radar.

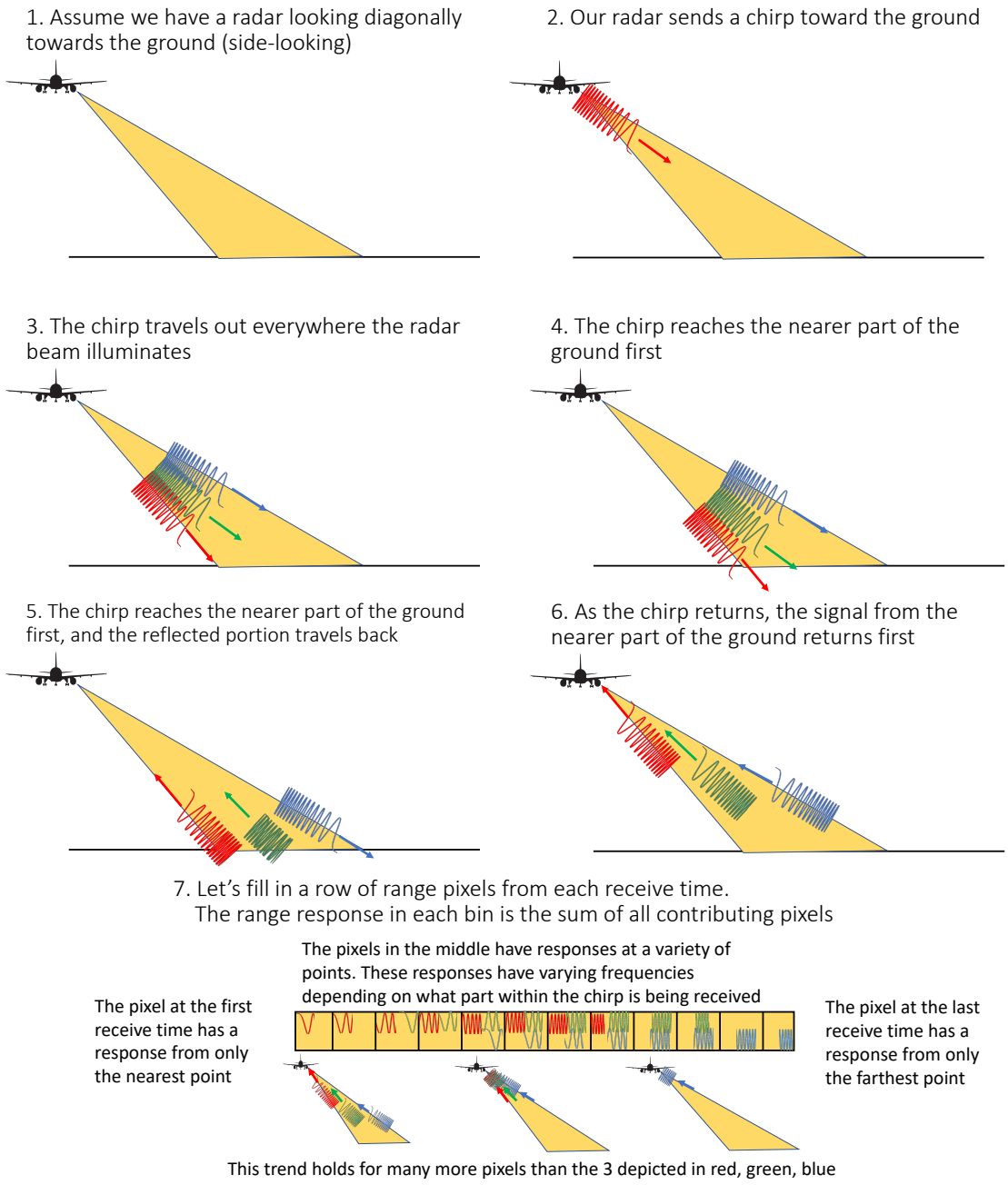

Figure 2.4: Visualization of a radar pointing to the side sending a chirp, and the travel path of the chirp to various points on the ground within the radar beam. For easier visualization, the chirp shown is one-sided ($t > 0$ in Eq. 2.7)

We want to be able to separate the targets based on where they're centered

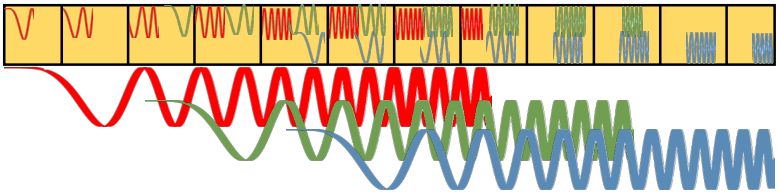

If we align this set of targets with our chirp function, we can see that the values are well-aligned when the red chirp is here, the green chirp is here, and the blue chirp is lined up here. But the signals in the bins, from all the different return points, still add up randomly:

We can convolve the received signal with a reference chirp to isolate targets…

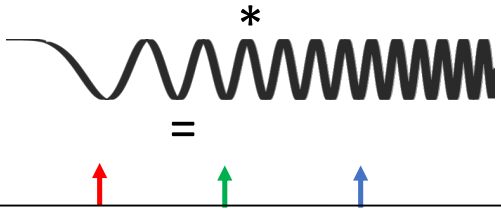

After convolution with the **reference chirp** – comparing the received signal to the signal we sent from our radar – three clear impulse responses from three distinct ground locations are clearly visible!

We can make this even more efficient in the frequency domain: Convolution in the time domain translates to multiplication in the frequency domain. Below, we see our received signal convolved with the transmitted (reference) signal, a symmetric chirp – for visualization, this reference signal is split into a real and imaginary part in blue and red. Convolution follows the top line, and results in a **range compressed** final signal with distinct targets.

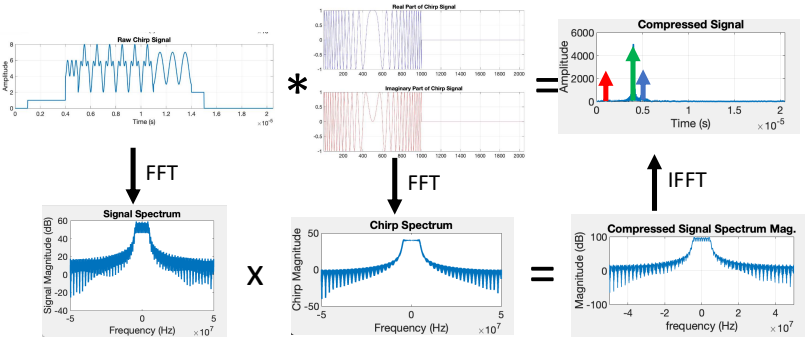

By taking fast Fourier transforms (FFTs) of the reference and return signal, we can simply multiply them to find the compressed signal in the frequency domain. Then, an inverse Fourier transform restores the compressed signal. Processing in the frequency domain is more computationally efficient.

Figure 2.5: Visualization of pulse compression. Pulse compression focuses data to a fine resolution in the range direction (perpendicular to the direction of travel) for a radar.

Mathematically, pulse compression can be viewed as convolution of the received signal with the reference signal, which is the waveform sent to the radar. The compressed signal for a received signal $s_{received}(t)$ from a signal sent from the radar $s_{ref}(t)$ is

$$s_{compressed}(t) = s_{received}(t) * s^*_{ref}(t) \tag{2.8}$$

for convolution operator $*$ and conjugate of s defined as s^*. The reference signal is given by (2.7), and is the same chirp signal sent by the radar.

Convolution in the time domain can equally be represented by multiplication in the frequency domain, which has the benefit of faster processing. Instead of convolving the received signal with the reference, we can instead take the Fourier transform of each, multiply, and take the inverse Fourier transform of the result (this is also represented in Fig. 2.5). Taking the Fourier transform of each signal such that $s \to S$ yields

$$S_{compressed}(t) = S_{received}(t)S^*_{ref}(-t) \tag{2.9}$$

A Fourier transform of the received and reference signals, multiplication, and an inverse Fourier transform yield a finely focused signal in the range direction. This frequency encoding enables us to have a longer pulse that is still discriminated from overlapping pulses. Instead of the resolution being dictated by the pulse duration, it now relies on the bandwidth, B, encompassing the range of frequencies encoded. The new range resolution

$$\delta_r = \frac{c}{2B} \tag{2.10}$$

and can be improved by increasing the bandwidth, without reducing the pulse duration. Before, a reduced pulse duration would result in finer resolution but less energy transmitted to the target, resulting in a weaker signal. Range compression enables a long pulse duration, with more energy sent to the target over time, without compromising resolution.

2.2.2 Two Dimensions of Radar Imaging

Whether implemented via convolution or multiplication in the Fourier domain, this process of range compression focuses the image relative to distance from the radar. For radar imaging, there are two dimensions. The first is the range direction, whose signal is focused via the process detailed in the previous section. The range direction is perpendicular to the direction of radar travel; for this reason it can also be referred to as the **across-track** direction. The second dimension is along the path of radar travel and can be called the **azimuth** or **along-track** direction.

As the radar travels along the flight track, it sends a series of pulses. Each pulse is compressed to focus the data in the range dimension, disambiguating nearby targets that both return signals

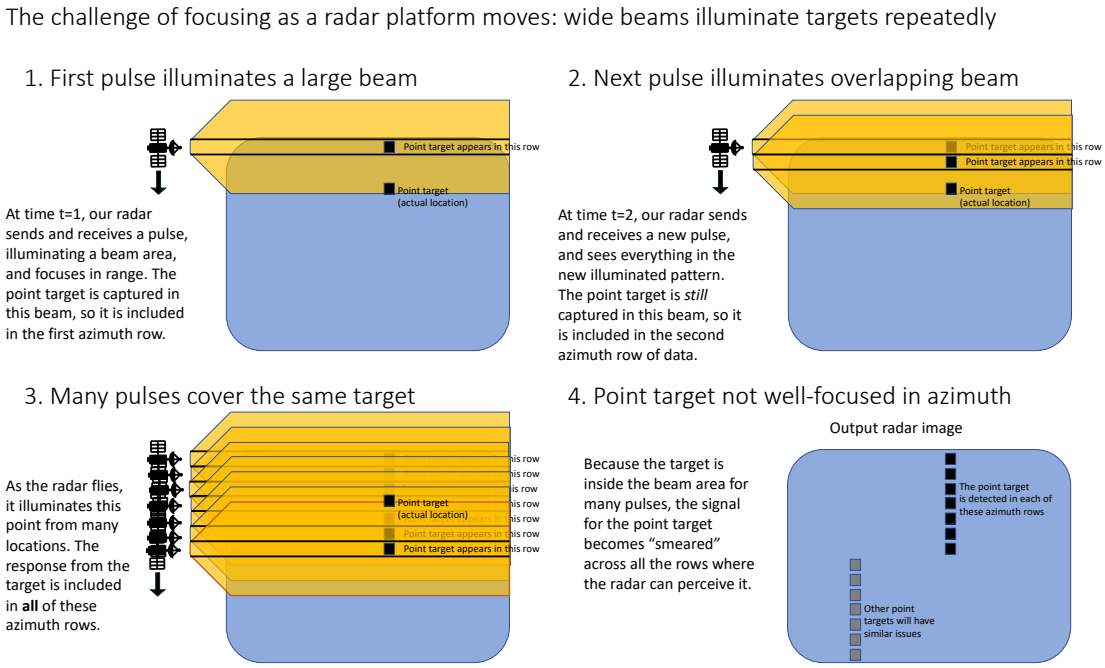

Figure 2.6: Visualization motivating azimuth focusing in radar.

to the radar at overlapping times. A similar phenomenon can happen in the azimuth direction, but across multiple pulses. Each pulse from the radar illuminates a ground area with some beam width, but the pulses are usually sent frequently enough that a given target is likely to fall within the beam of multiple consecutive pulses as the radar passes over it. For this reason, focusing of radar data in the azimuth direction is also required to achieve a fine resolution. The next section provides an overview of two different ways that azimuth compression can be achieved using synthetic aperture radar focusing techniques.

Because range processing occurs using a single radar pulse, while azimuth processing involves focusing the data across multiple pulses spaced out in time, these two processing techniques are sometimes also referred to as **fast time** and **slow time** processing.

2.2.3 Azimuth Compression: Synthetic Aperture Radar

The motivation for azimuth focusing is similar to range focusing: signals that the radar receives from different targets may overlap, and the radar may receive signals from a small target across a variety of times, leading to ambiguity in determining the target location from the travel time. Figure 2.6 shows the motivating problem behind synthetic aperture radar. With conventional (real aperture) radar, a larger antenna produces a better-focused signal, increasing the gain in the direction of the

target. When imaging targets from space, however, the gain achieved from building a larger antenna is dwarfed by the large distance to the target. To finely focus on a target many kilometers away, an antenna would need to grow unrealistically large in size.

In SAR processing, we are restricted to antenna sizes that are reasonable to mount on a platform and fly or launch, so the antenna beam is accordingly wide rather than narrowly focused. In Fig. 2.6, we can see that as the platform moves past a target, it sends many successive pulses. Each of these pulses is focused in range using the range compression process outlined from the previous slide. The pulses illuminate a relatively large beam area at the target, so responses from every point illuminated in the beam is recorded as being present in the radar's signal at a given location in the platform's trajectory. As a result, the signal from each target is recorded in a series of successive pulses from the platform, creating ambiguity about which location along the trajectory (i.e., in the azimuth direction) most directly illuminates the point target. Moreover, there are usually many different targets in a scene, creating additional ambiguity around picking out the response from one location in the target area. The azimuth resolution of a real-aperture radar is given as:

$$\delta_{az} = \frac{\lambda R}{l} \tag{2.11}$$

for antenna length l, radar wavelength λ, and range to target R. A larger antenna will help resolve the target, but a large R (as is often the case when imaging a target from the air or space) limits the resolution.

A SAR image that has been focused in range but not in azimuth will look "streaky," as the points in the range direction are narrowly constrained, but smeared out along the azimuth direction. Figure 2.7 shows an example.

Fortunately, we can use information from the travel path of the platform to determine the true layout of the target area at fine resolution. This thesis will discuss two methods of azimuth focusing, range-Doppler processing and backprojection. Both rely on the fact that the antenna's location changes relative to the target over time.

Range-Doppler Processing

For range-Doppler processing, we assume that the platform is moving at a constant velocity relative to the target, and sending pulses repeatedly at a rate defined as the **pulse repetition frequency** (PRF). As the radar moves past a given target, it sends a series of pulses that include the target in the antenna beam. Figure 2.8 shows the key insight to range-Doppler processing. When the target is ahead of the radar along the flight track, the radar and target have relative motion towards each other, and so the signal that the radar receives has a positive Doppler shift. As the radar passes the target, the platform motion is perpendicular to the look direction towards the target, so there is no Doppler shift in the received radar signal from the target. Finally, after passing the target, the

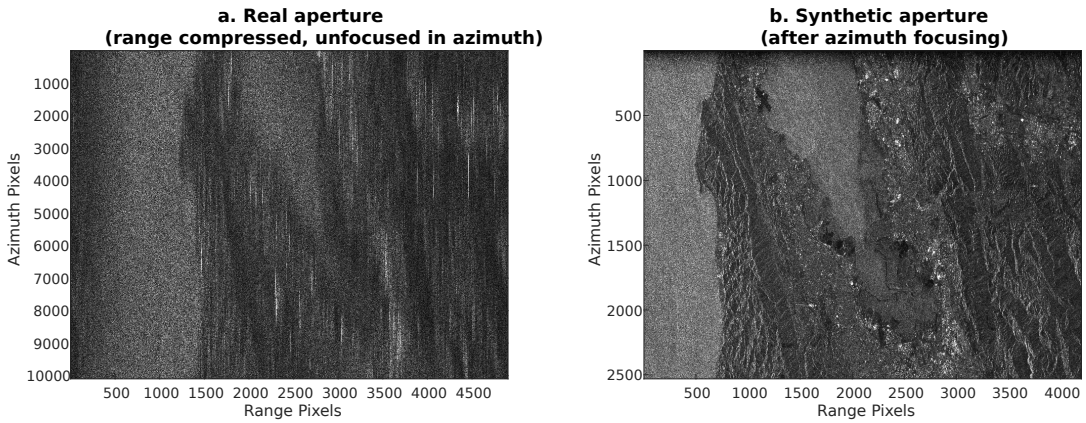

Figure 2.7: (a) A SAR image of the San Francisco Bay Area from the European Remote Sensing (ERS) satellite that has been focused in range but not azimuth looks streaky because the radar illuminates it over a long time. (b) Azimuth compression focuses the signal coming from each target to achieve a fine-resolution image.

radar is moving away from the target, and the signal from the target has a negative Doppler shift.

Mathematically, assuming a constant flight path relative to the ground, the distance to each point changes linearly over time. Defining the signal along the azimuth direction to have zero phase when the target is directly perpendicular to platform motion (neither ahead of or behind the platform; directly along the line of sight at the closest distance between platform and target) to have a range of R_0, we can find the signal along azimuth as

$$s(t) = e^{-j(\phi_0 + \frac{2\pi}{\lambda R_0} v^2 t^2)} \tag{2.12}$$

where v is spacecraft velocity, t is time where closest approach to target is at $t = 0$, ϕ_0 is an arbitrary initial phase, and λ is wavelength. The key to this equation is to notice that s(t) along the azimuth direction is proportional to a signal that is quadratic in time ($\propto t^2$). This means that the motion of the platform itself relative to the target is producing a chirp in time: a signal that is quadratic in phase is linear in frequency, because frequency is the rate of phase change. We can therefore use the known properties of the radar system (velocity v, range R_0, wavelength λ) to derive a matched filter for the signal in the azimuth direction. The reference signal takes form

$$s_{az,reference}(t) = e^{j\frac{2\pi}{\lambda R_0} v^2 t^2} \tag{2.13}$$

This reference signal can be used for azimuth compression, just as the reference signal in range could be used for range focusing. This matched filter then enables very fine focusing in the azimuth direction, as is demonstrated in Fig. 2.7. The resolution in azimuth δ_{az} after azimuth compression

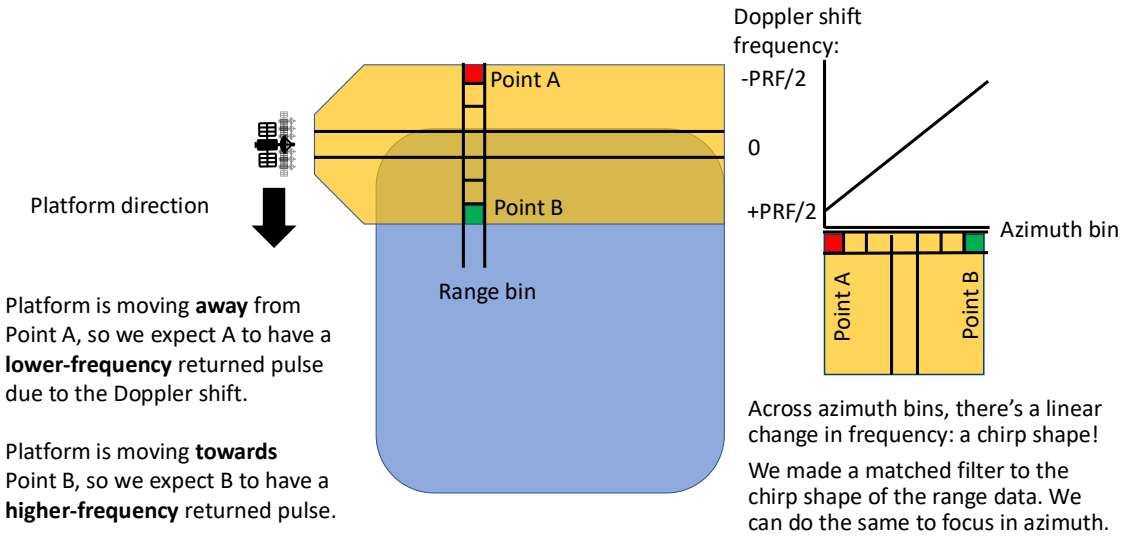

Figure 2.8: As the platform moves, the distance to the targets changes linearly over time. This means that over time, the Doppler shift from a specific target also changes the frequency linearly over time. A linear change in frequency over time results in a chirp signal.

is

$$\delta_{az} = \frac{l}{2} \tag{2.14}$$

Instead of an inverse relationship to antenna length, synthetic aperture radar has an azimuth resolution proportional to antenna length – meaning that shorter antennas will improve the resolution. This remarkable improvement is brought about because shorter antennas have a larger beam, so images can be reconstructed from more points along the radar path.

This Doppler view of azimuth focusing does make a few assumptions, and may require a few corrections after processing. These steps may include:

1. Range migration: Range migration is a result of the variation in range of a given point from the view of the platform. As the platform passes a given point, the distance to the point changes throughout the platform's pass – first more distant, then closer until closest approach, then more distant as the platform moves past the point. This results in a slight error in the apparent sorting of points into range bins, and can be compensated for by shifting the range bins, as shown in Fig. 2.9.

2. Motion compensation: Corrections may also need to be applied for motion of the platform if the platform deviates from its expected track at all. Correcting for motion compensation is especially important for airborne platforms, which can encounter more wind and atmospheric turbulence.

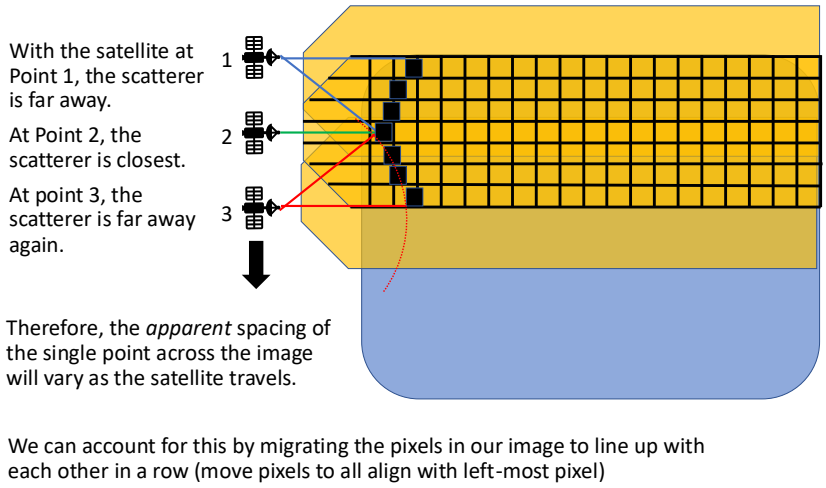

Figure 2.9: As the satellite passes, a given point will not always have the exact same range. Range migration compensates for the variation in range as a platform passes a target.

3. Coregistration: When comparing multiple SAR images (as in InSAR), if the flight tracks of the platform are different from one pass to another, the features in the resultant images may be misaligned. Coregistration aligns the images so that the corresponding pixels in each image contain the same features.

4. Geocoding: The final focused image is defined in a coordinate system relative to the radar, which may not correspond exactly to the ground coordinates of interest. Geocoding reprojects the coordinates from range and azimuth dimensions onto a relevant grid for the application, often latitude and longitude. In places with elevation variations, geocoding warps the image to map pixels into the correct latitude/longitude, accounting for variations in elevation that cause distortions in the radar image. The geocoding step may be combined with coregistration to generate coregistered images on a desired grid.

Backprojection

Backprojection processing is an alternate method to range-Doppler processing. While range-Doppler processes in the Fourier domain, assuming characteristics of the platform's travel in order to generate a matched signal, the backprojection algorithm corrects for the phase at each point pixel-by-pixel by adding a coherent phase compensation to the phase at each acquisition, so that phases from all acquisitions are optimally added in-phase at the target point. A visual can be seen in Fig. 2.10.

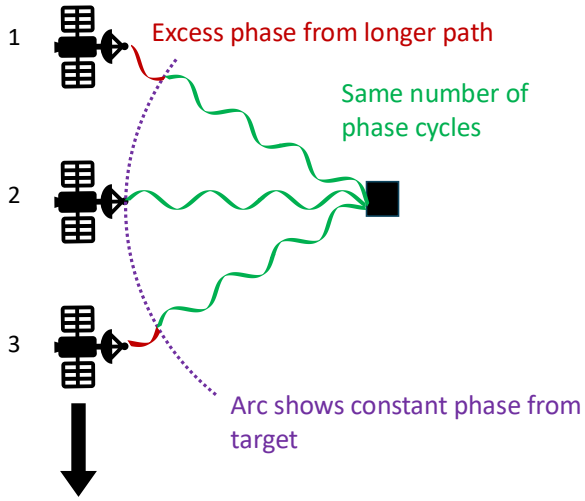

Figure 2.10: Concept of backprojection azimuth focusing. At each point in azimuth processing, a phase compensation is added to the signal so that all points focus to be in-phase at a given target. This process is repeated for each target point on the ground.

Following [142], the complex interferometric signal $i(x)$ can be produced from an acquisition s

$$i(x) = \sum_k s(r(x,k))e^{-jr(x,k)\frac{4\pi}{\lambda}} \tag{2.15}$$

for distance from sensor to target to target $r(x,k)$ as a function of pulse number k and pixel location x. At each received pixel location, the signals are summed from all pulses k that illuminate the target. The signal s at this location is scaled by the phase proportional to the travel time, so that any signal coming from the target at location x to the radar at any acquisition k has the same phase. This phase compensation process diminishes signals from targets located away from x, which would have varying responses to the phase, while amplifying the phase from x. This process is performed for each target x for all pulses k illuminating each target.

Backprojection has several advantages over range-Doppler processing. Range-Doppler processing assumes a constant, smooth flight track and constant PRF, and requires correction after processing if there are variances in these quantities. As long as the flight trajectory and time of sending pulses is known, variance in flight track and pulse repetition is automatically compensated for in backprojection, eliminating additional processing steps such as range migration and motion compensation, and allowing coregistration and geocoding to be combined into the same step as the focusing.

The disadvantage of backprojection is primarily in processing time. Filtering in the Fourier domain is comparatively efficient, while backprojection requires calculating distances to each pulse

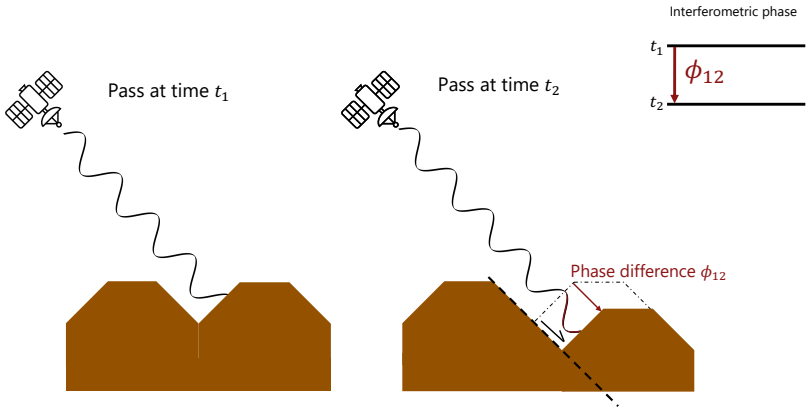

Figure 2.11: Diagram showing how phase difference is detected from ground motion using repeat-pass InSAR

from each ground point. While this $O(n^2)$ level of computation may be a greater challenge in computationally constrained environments, parallel computing and improved processing efficiency mean that, as of 2025, backprojection processing is computationally feasible in most scenarios.

2.3 Interferometric Synthetic Aperture Radar

Synthetic aperture radar images are complex, that is, containing an amplitude and a phase at each pixel. The phase is a function of distance: the radar wave completes many phase cycles on its way to its target, and the exact phase received at the radar is based on the radar wavelength and the two-way distance to the target. With repeat-pass Earth-imaging radar, the radar passes by the same target along nearly the same path at a later time. If the ground in that target area has moved, the two-way distance to the radar track changes, and the radar will receive a signal from that target with a different phase, as shown in Fig. 2.11.

If we represent the amplitudes of the two focused radar images as a_1 and a_2, and the phases as ϕ_1 and ϕ_2, we can describe the signals s_1 and s_2 from the two radar passes as:

$$s_1 = a_1 e^{-j\phi_1} \tag{2.16}$$

$$s_2 = a_2 e^{-j\phi_2} \tag{2.17}$$

To interfere these two signals, we can simply cross-multiply the first signal by the complex conjugate of the second:

$$s_1 s_2^* = a_1 e^{-j\phi_1} a_2 e^{j\phi_2} = a_1 a_2 e^{-j(\phi_1 - \phi_2)} \tag{2.18}$$

The phase of this interfered signal is proportional to the difference in distance between the target

and the radar during the first and second passes. The relationship between the differential phase and ground motion is:

$$\phi_{12} = \phi_1 - \phi_2 = \frac{4\pi}{\lambda} d \tag{2.19}$$

where λ is the radar wavelength, d is the ground deformation, and ϕ_{12} is the differential phase in radians. By computing the differential phase between two SAR images at every pixel, we can form a map of the phase differences at every point on the ground. We refer to this technique as **interferometric synthetic aperture radar (InSAR)**[3], and we refer to the map of phase differences as an **interferogram**.

For accurate repeat-pass InSAR measurements, all repeat passes should be approximately along the same track. The distance between the track the platform follows from one acquisition to another is called the **spatial baseline**. The time between acquisitions is called the **temporal baseline**. While a small spatial baseline is generally desired, the optimal temporal baseline depends on the phenomena being captured – the goal is to capture change on the ground from one time to another.

The phase difference $\phi_1 - \phi_2$ in radians may exceed 2π if the path to the ground changes length by more than one phase cycle. We can only measure phase of the complex interfered radar signal ϕ_{12}, however, modulo 2π (or varying between $-\pi$ and π. In practice, this means that there is a $2\pi N$ (for integer N) phase ambiguity in the interferometric phase. In the interferogram image, a continuous change in phase will appear as bands of phase cycles modulo 2π. A band of one complete phase cycle is called a fringe. The pattern of fringes is a contour map of the displacement along the radar line of sight, with each contour corresponding to a displacement of half of the radar wavelength. Figure 2.12 displays an interferogram with phase contours, which we call a **wrapped interferogram**. When the displacement is continuous across the image, counting the number of fringes yields the number of 2π phase cycles. Using (2.19), we find that each fringe corresponds to $\frac{\lambda}{2}$ in displacement.

To translate the phase cycles in a wrapped interferogram into absolute displacement, we can use a process called **phase unwrapping**. Phase unwrapping aims to turn the continuous phase cycles into a smooth map of true relative displacement within the interferogram. Phases are no longer constrained between $-\pi$ and π and instead vary relative to some reference point within the interferogram.

The unwrapped phase can then be translated to displacement along the direction of the radar line of sight: every 2π in phase corresponds to a wavelength λ in two-way wave travel to and from the ground, so the line-of-sight displacement $d = \frac{4\pi}{\lambda}\phi$ for unwrapped phase ϕ. The displacement measured from the unwrapped interferogram from Fig. 2.12a is shown in Fig. 2.12b. In this displacement figure, red represents uplift and blue represents sinking of the ground. This unwrapped interferogram shows sinking of the Kilauea caldera from an eruption on the Big Island of Hawaii

[3]Before repeat-pass InSAR, synthetic aperture radar passes over the same area from different locations could be interfered to construct the topography of the area [143]. Such techniques, which are sometimes also referred to as InSAR, are still used today to create digital elevation models (DEMs). For the sake of this thesis, when we say "InSAR" we are referring to repeat-pass interferometric SAR.

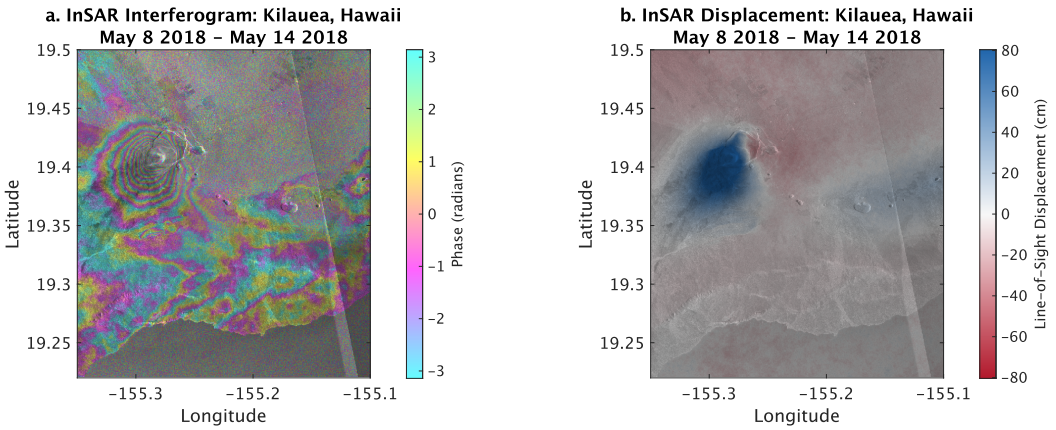

Figure 2.12: InSAR interferogram

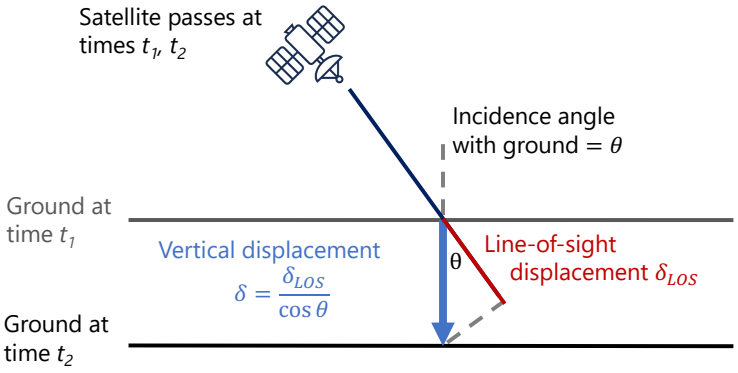

Figure 2.13: Projection of vertical displacement into InSAR line-of-sight.

in 2018. To the east of the caldera, the lighter blue region denominates the East Rift Zone, which was also deforming at this time. Several more corrections and calibrations may be required to ensure that an interferogram's unwrapped phase is accurate (for example, in this image, much of the northern area that is red for uplift is over a highly vegetated area with low signal quality, and would likely be filtered out; so would measurements inside the collapsed caldera, where too much change in the ground degrades signal quality). After these corrections, the line-of-sight deformation could be projected into the direction of deformation using geometry of the scene, such as the solution for the vertical displacement shown in Fig. 2.13. While the example in Fig. 2.13 is valid assuming purely vertical displacement, Earth deformation may occur in any dimension (vertical, north/south, east/west), so in practice, more than one InSAR measurement from different angles may be necessary to resolve the correct dimensions of displacement.

Because InSAR can detect changes as small as a fraction of a wavelength, it is sensitive to ground motion of a centimeter or less. The wavelength of the Sentinel-1 InSAR satellite used for much of

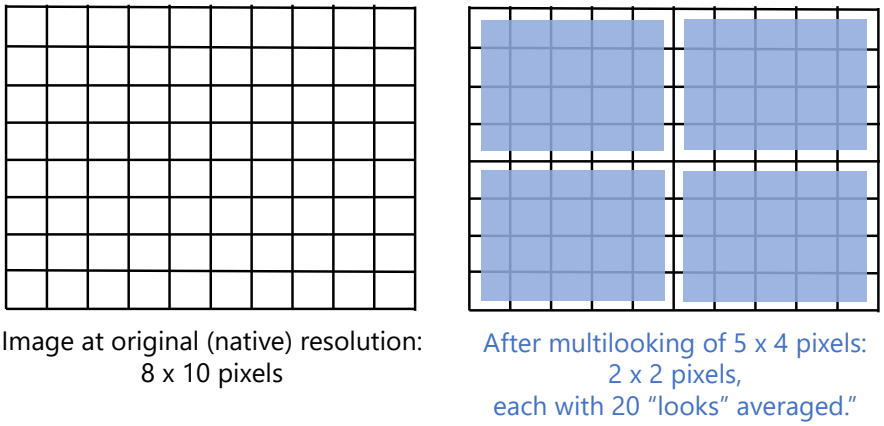

Figure 2.14: Schematic of InSAR multilooking.

the work in this thesis is 5.6 cm. Typically, noise sources such as atmospheric noise and system noise cause enough signal degradation that InSAR is accurate between on the order of 1 cm [146].

To improve signal quality, InSAR images are often multilooked. Multilooking (for example, Fig. 2.14 refers to spatial averages of all pixels within a given window, reducing the dimensions of the image by a factor of the averaging window size. Because SAR data sets frequently have large data volumes, multilooking makes the data size more manageable, as well as increasing signal-to-noise ratio inside the image, with the trade-off of a coarser resolution. Decreasing the dimension in averaging also ensures that the multilooked pixels are statistically independent, rather than containing redundant information (for example, if the image was put through a box filter).

One common measure of signal quality is the interferometric coherence, also called correlation, which measures how well-aligned the phases are in a multilook window. Coherence varies from 0 to 1, with a coherence of 1 indicating that all pixels in the window are exactly aligned in phase. Coherence ρ is derived from the equation

$$\rho = \frac{\langle s_a s_b^* \rangle}{\sqrt{\langle s_a s_a^* \rangle \langle s_b s_b^* \rangle}} \tag{2.20}$$

where s_a, s_b are the complex values of the full-resolution SAR images and angle brackets $\langle \cdot \rangle$ represents the spatial average inside of the multilook window [89]. The absolute value $|\rho|$ is the coherence, while the multi-looked interferometric phase can be calculated as $\angle\rho$. Coherence can be low where many scatterers are changing from one image to another inside of a multilook window, for example in vegetated areas. Coherence is typically higher over bare ground. Many unwrapping algorithms filter data based on coherence, so that they only unwrap the InSAR phase where they have a high confidence of the signal quality [24].

Using a set of multilooked interferograms covering the same area over a period of time, further

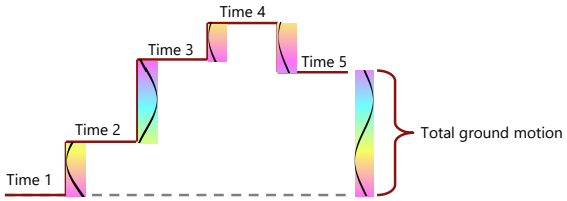

Figure 2.15: Cumulative displacement calculated at a pixel over 5 SAR scenes (four sequential interferograms)

analysis can be done over the time series of interferograms. One basic example of this is calculating deformation over a time period spanning multiple interferogram acquisitions. Because each interferogram represents a difference in ground deformation from one time step to another, adding up these differences over time yields the displacement over that time period. In this simple case, a time series of phases from sequential interferograms can be cumulatively summed to find displacement. Figure 2.15 shows how cumulative displacement is added up.

2.4 InSAR Applications and Error Sources

Repeat-pass interferometric synthetic aperture radar was first demonstrated in 1989, showing that repeat passes could be used to map small ground deformations from water-absorbing clays [46]. This method was soon applied to measure deformation from earthquakes [81, 145], ice sheets [50], volcanoes [80], and land subsidence due to aquifer compaction and fluid change in the ground [48]. Mapping of permafrost deformation was also demonstrated, both in the form of rock glacier creep [111] and seasonal permafrost uplift and subsidence [130].

As the applications of InSAR expanded, so did the techniques to ensure its accuracy. Errors in InSAR can come from almost any stage of the process of making images, from system thermal noise on-board the radar to errors in unwrapping. The scientific community therefore made efforts to quantify noise from decorrelation [140] and atmospheric noise [146], and to reduce other sources of error and noise. Some techniques that have been widely adopted include using persistent or permanent scatterer interferometry, which seeks to analyze only pixels whose scattering characteristics are consistent and strong across images [45], as well as small-baseline subset analysis, which considers all pixels in an interferogram, but finds time series solutions based on subsets of interferograms with sufficiently small spatial and temporal baselines to ensure low decorrelation between images [8].
Noise and error sources in InSAR include:

1. Radar speckle: not strictly noise, these random variations in the signal come from uneven scattering distributions across image resolution cells.

2. Thermal noise from the radar system: This noise is random and based on the temperature of

the radar system.

3. Random noise from atmosphere: This noise is generally assumed to be zero-mean and comes from random fluctuations in the molecules making up the atmosphere.

4. Spatially correlated tropospheric noise: Variations in humidity in the troposphere can lead to path delays in SAR images that are spatially correlated within an image and can also be correlated with topography; these can generally be assumed to be random over the time between radar acquisitions [93].

5. Ionospheric noise: Noise from free electrons in the ionosphere can lead to defocusing in the azimuth directions in individual SAR scenes, and to phase ramps in interferograms [132]. One way to mitigate ionospheric effects is with split-spectrum techniques [44].

6. Decorrelation: Areas where the scatterers composing a radar pixel change from one acquisition to another may be subject to decorrelation, where the phases before and after the change appear random or uncorrelated. This is common in vegetated ground, as plants might grow, shed leaves, blow in the wind, or otherwise change which scatterers make up a resolution cell. Decorrelation can also occur as a result of lava flows, snow fall or melt, landslides, and construction, or as a result of a spatial baseline between acquisitions [140].

7. Unwrapping errors: Errors in phase unwrapping may occur especially at phase discontinuities (such as earthquake faults), in noisy areas, or places with dense interferogram fringes due to rapid change. Sometimes they are visually apparent, while other times these errors are very difficult to spot [104].

8. Apparent bias due to scattering changes in pixel. While many of the noise sources in this list are zero-mean and random, studies have found errors in InSAR time series that are consistent over time [4]. These errors have been called "systematic bias" and "fading signals;" in this thesis, we will show that they may arise as a result of changes in independent scatterer populations within a pixel, such as moisture change in a material resulting in different scattering from its surface and subsurface.

A source of error in InSAR deformation that is of particular interest to this thesis is the last one listed: phase arising from scattering changes in a medium, such as changes in soil moisture. Although InSAR is often thought of as primarily interacting with the Earth's solid surface, the radar waves, in fact, may interact with multiple layers of materials. With vegetation above the surface and varying soil layers comprising the ground itself, the surface is in many places more complex. Radar interactions may involve more than simple direct scattering from whatever material the wave reaches first; instead, radar waves may propagate through a medium before scattering. To better understand this, we take a closer look at scattering through dielectric media.

Figure 2.16: Example of surface and subsurface scattering in water. In Stanford's pool, surface reflections of trees are visible, as are lane lines at the bottom of the pool. In Lake Lagunita, reflections of clouds, trees, and Hoover Tower are visible on the surface of the lake, and mud and sticks are visible from the bottom. Photos taken by Elizabeth Wig.

2.5 Characterizing Common Media

Over most of the Earth's land surfaces, some combination of vegetation and soil is visible to radar. Therefore, characterizing radar interactions with these materials are important. At radar wavelengths, soil and vegetation are largely composed of **dielectric** materials, meaning they are non-conductors of electricity. When an electromagnetic wave encounters a dielectric material, typically some portion of the wave energy scatters or reflects from the surface back into the air, while another portion scatters or refracts into the material, propagating inside of it. If the dielectric material has a lower interface (like a conductor) lying underneath it, some of the wave will scatter back from this lower interface, scatter or refract through the surface, and propagate out to the air, where it may interact with a sensor. Therefore, signals from both a surface and a subsurface are visible.

This holds true at visual wavelengths, too. Figure 2.16 shows two images of water around Stanford's campus: the Arrillaga pool, and Lake Lagunita. In both images, reflections from the surface are apparent, as is a view of the bottom of the water: the swim lanes in the pool, and the dirt and sticks at the bottom of the lake. The eye sees a combination of signals from the surface and the subsurface.

Like water at visual wavelengths, soil and vegetation are semi-transparent to radar wavelengths, resulting in reflection from surfaces and subsurfaces. Electromagnetic propagation through dielectric materials is governed by the Fresnel equations based on the relative *dielectric constant* ϵ_r (also called relative permittivity), which is composed of real and imaginary parts such that $\epsilon_r = \epsilon' + j\epsilon''$ for imaginary unit j. The real part, ϵ', determines the speed of wave propagation through a medium

(which changes the wavelength within the medium, as a wave's frequency is constant through the media it travels through). As we shall see, it also determines the index of refraction into or out of the medium at a boundary of the medium, as well as the transmission and reflection coefficients, which determine the proportion of energy that propagates forward into, and backscatters from, the medium.

When a wave encounters an interface between dielectric media, some portion of the wave propagates into the medium, while another portion reflects back. The reflection coefficient Γ determines the amount of energy reflected back (The power reflection coefficient $|\Gamma|^2$ determines the power reflected). For normal incidence:[4]

$$\Gamma = \frac{n_1 - n_2}{n_1 + n_2} \tag{2.23}$$

for refractive indices $n_1 = \sqrt{\epsilon_1}$, $n_2 = \sqrt{\epsilon_2}$. The transmission coefficient $T = 1 + \Gamma$ determines the amount of energy transmitted into the dielectric. Travel through a dielectric makes waves travel more slowly: when a wave enters a dielectric, it maintains the same frequency but has a shorter wavelength. Finally, according to Snell's Law, waves that enter a dielectric at incidence angle θ_i will refract inside the dielectric, traveling at transmission angle θ_t according to:

$$n_1 \sin\theta_i = n_2 \sin\theta_t \tag{2.24}$$

The relative dielectric constant ϵ_r is defined relative to free space, whose dielectric constant is defined as $\epsilon_0 \approx 8.854 \times 10^{-12}$. The true dielectric constant of an arbitrary medium ϵ is defined as the relative dielectric constant times the permittivity of free space ϵ_0, so that $\epsilon = \epsilon_r \epsilon_0$. In radar remote sensing, it is generally safe to assume that radar waves are traveling through air or space before interacting with a medium. The dielectric constant of air is approximately the same as free space, so $\epsilon_r = 1$ (and therefore $n = \sqrt{\epsilon_r} = 1$; air is not very lossy at radar wavelength, and the propagation speed is roughly similar to that of vacuum.

While this manuscript generally models propagation in terms of distances, phases, and ϵ_r values, some applications model propagation in terms of wavenumbers. A wavenumber k describes the spatial frequency of waves within a medium, which depends on the frequency and the dielectric constant. For waves with a free-space wavelength λ and complex refractive index $n = \sqrt{\epsilon_r}$,

$$k = \frac{2\pi}{\lambda} n \tag{2.25}$$

[4] At non-normal incidence, Γ has an additional factor that varies based on incidence angle θ_i and transmission angle θ_t as well as wave polarization. For s-polarized waves, where the polarization is normal to the plane of incidence,

$$\Gamma_s = \frac{n_1 \cos\theta_i - n_2 \cos\theta_t}{n_1 \cos\theta_i + n_2 \cos\theta_t} \tag{2.21}$$

For p-polarized waves, where the polarization is parallel to the plane of incidence,

$$\Gamma_p = \frac{n_2 \cos\theta_i - n_1 \cos\theta_t}{n_2 \cos\theta_i + n_2 \cos\theta_t} \tag{2.22}$$

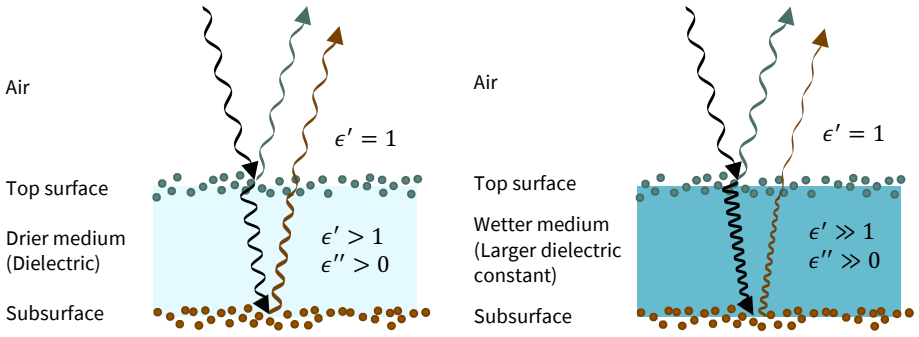

Figure 2.17: Radar wave interaction with medium.

In soil and vegetation, the values for ϵ' are often in the range of 2 to 60, while the values for ϵ'' range from 0 in dry material to 30 in very wet material. [53, 123, 30]. The main driver of these differences is the relative proportions of air, water, and other matter in the soil or vegetation. Air has a very low dielectric constant, $\epsilon_r \approx 1 + 0j$, while water has a very high dielectric constant at microwave frequencies. Treating a vegetation layer as a bulk medium, air is highly dominant by volume, while most soils have some pore space but a more significant proportion of solid material.

A dielectric medium made up of more than one of these materials can be described using a mixing model, which linearly scales the bulk dielectric constant according to the proportions of constituent materials. A model for soil or vegetation containing pores that are sometimes filled with water and sometimes air will, therefore, vary in bulk dielectric constant depending on the proportion of water to air filling those pores. The bulk dielectric constant will be much higher in a wetter material than a drier one. A simple bulk dielectric model can look like Fig. 2.17. A wave reaches a dielectric medium (e.g. soil) from the air. Part of the signal reflects from the top of the medium, while part scatters into the medium; the amount scattered forward and back is dependent on the reflection and transmission coefficients. Inside the medium, the wave travels along a steeper path due to the nonzero dielectric constant, and it has a shorter wavelength. The wave also decays with the distance it travels in the lossy medium. In this diagram, the wave reflects from a lower subsurface within the medium, propagates back up through the medium, and a portion of it forward scatters through the interface with air to return to the radar. The signal that returns to the radar is therefore a mix of the responses from the surface and the subsurface reflections.

We will see the effect of these scattering changes on InSAR signals in future chapters.

Chapter 3

A Model for InSAR Closure Phase

Note: Parts of this chapter draw from a paper coauthored with Roger Michaelides and Howard Zebker [134].

3.0.1 InSAR Closure Phase

In most InSAR applications today, two complex SAR images are interfered from repeated passes over the same area, and the phase difference between the images is often interpreted as deformation of the ground surface [46, 8]. We commonly estimate deformation by computing radar interferograms, taking into account tropospheric and ionospheric delays, errors in phase unwrapping, satellite position uncertainties, decorrelation due to scattering changes over time, and system noise. The residual phase values are ascribed to temporal differences in radar path length and are interpreted as surface deformation [144].

A further combination of interferograms into cyclic groups of three leads to cancellation of most of these phases (as well as the deformation signal) and produces a *closure phase* [41, 154, 89]. The closure phase can be viewed as a nuisance term when calculating deformation, but more importantly, it can be exploited to better understand a wider range of surface changes beyond ground deformation. Key among these are changes in water content and distribution in the soil and in vegetation canopies. The closure phase is the argument of the triple product Γ_{123}, which is the output from a circular combination of three interferograms from three SAR scenes [152]. Summing over a finite number N of adjacent pixels,

$$\begin{aligned}\Gamma_{123} = &\left(\frac{1}{N}\sum_{n=1}^{N} I_{12_n} e^{j\phi_{12_n}}\right) \times \\ &\left(\frac{1}{N}\sum_{n=1}^{N} I_{23_n} e^{j\phi_{23_n}}\right) \times \left(\frac{1}{N}\sum_{n=1}^{N} I_{31_n} e^{j\phi_{31_n}}\right)\end{aligned} \tag{3.1}$$

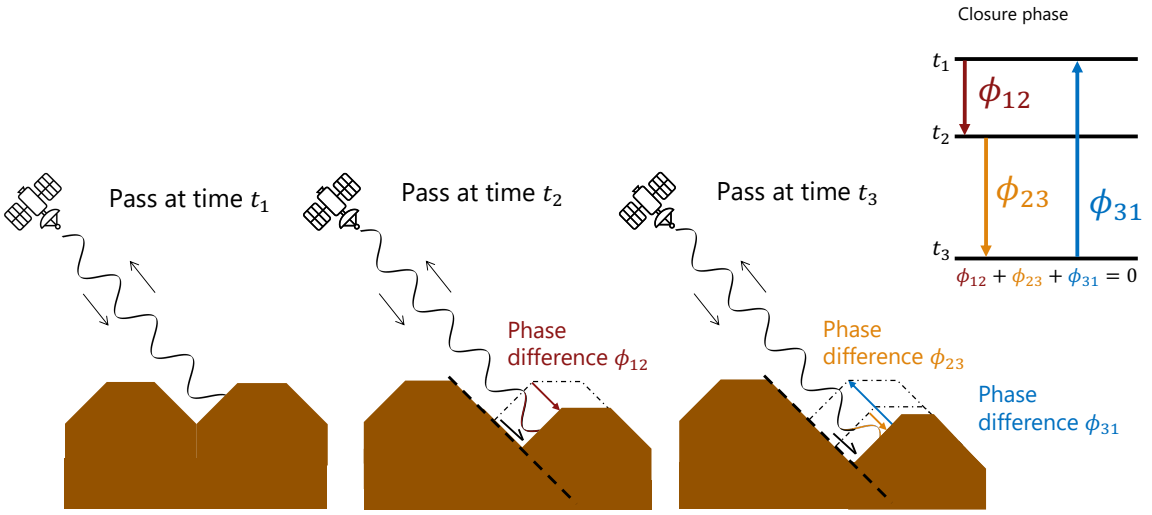

Figure 3.1: Visual of calculation of closure phase. Closure phase is produced by calculating the phases in a loop around a set of (usually three) interferograms.

for individual interferogram amplitudes at the n^{th} pixel $I_{12_n}, I_{23_n}, I_{31_n}$ and phases $\phi_{12_n}, \phi_{23_n}, \phi_{31_n}$. The closure phase ϕ_{123} can equivalently be viewed as a sum of the individual multilooked interferogram phases ($\bar{\phi}_{12}, \bar{\phi}_{23}, \bar{\phi}_{31}$, where a bar indicates that the phase is of the sample average found via multilooking) around the loop:

$$\phi_{123} = \bar{\phi}_{12} + \bar{\phi}_{23} + \bar{\phi}_{31} \overset{\text{may}}{\neq} 0 \tag{3.2}$$

For full-resolution processing with no spatial averaging ($N = 1$), the closure phase is identically zero (Fig. 3.1. The closure phase can become nonzero when regions of pixels are averaged spatially (as in multilooked images) before the net phase is computed [40, 41]. While it is still possible for the closure phase to equal zero in the presence of multilooking, it is no longer mathematically guaranteed.

Some component of nonzero closure phase can be attributed to random processes and noise, such as spatial baseline decorrelation and thermal noise [154, 140]. This stochastic component has an expected value of 0 after sufficient spatial averaging. The nonzero closure phase also has a systematic component with non-zero mean, which has been called the "systematic bias" [4, 154, 151] and has been linked to soil moisture [40, 86, 152, 153] and vegetation [39, 89].

Generally, at least two independent scattering mechanisms in a pixel are needed for systematic nonzero closure phase [41], or multilook pixels where the individual resels have different deformation histories [151, 12]. Changing moisture content in a material, whether soil, canopy, or snow, will change the bulk dielectric constant of the medium [30, 123, 52]. This, in turn, changes the echoes from the surface and subsurface, affecting both the energy reflected vs. transmitted at the surface,

and the electrical path length within the subsurface [40, 154, 153]. The interference signal can give rise to a systematic nonzero closure phase. Similar effects would result from a vegetation canopy overlying the ground surface, or from any other layered material with multiple time-varying contributions to the scattered signal. The soil moisture scattering mechanism is invoked in [151], which finds that the systematic bias correlates with cumulative rainfall time series. Figure 3.2 shows a schematic of layered media producing non-zero closure phase.

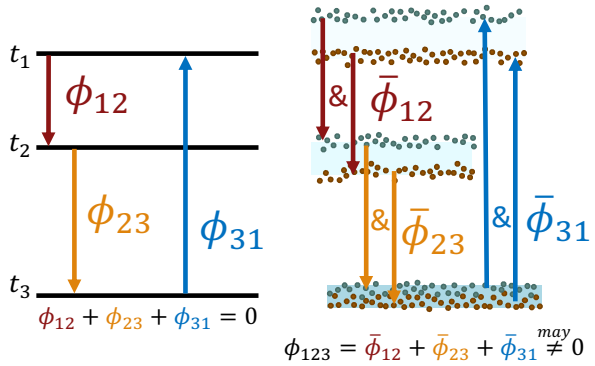

Figure 3.2: Closure phase cycle around three InSAR images. The three interferograms have phases ϕ_{12}, ϕ_{23}, and ϕ_{31}. For single-look processing (left), the closure phase is zero [154]. When contributions from multiple pixels are summed to produce multilooked phases $\bar{\phi_{12}}, \bar{\phi_{23}}, \bar{\phi_{31}}$, the closure phase may become nonzero. The black and blue dots represent two different scattering populations changing independently of one another (e.g. the blue dots may be soil wetting and the black may be ground surface); the ends of the arrows on the right may misalign because the interference signals between surface and subsurface scatterers change as the soil moisture changes.

Many previous works aim to correct the phase "bias" that leads to phase misclosure and causes errors in interferograms. Such errors are usually small compared to the atmospheric noise component in an individual interferogram, but the bias can compound over a time series [4]. Some works characterize or correct this bias [4, 151, 152, 154, 89, 3, 79, 43]; many leverage the full stack of interferograms or longer temporal baselines, which often empirically observe lower systematic phase biases [4]. Others invert for soil moisture explicitly, sometimes incorporating additional information such as interferometric phase [153], coherence magnitude [153, 39], SAR backscatter [39, 10], calculations of decorrelation phase [89, 86], or meteorological information [67]. External data are used to solve for the ambiguity where more than one soil moisture time series may generate the same closure phase even in the absence of noise [40, 41, 153].

This work considers the closure phase as a source of signal rather than error. We compute the closure phase only among three consecutive SAR images, so the temporal baselines remain short (typically $<$ 1 month). Shorter baselines have been shown to lead to a larger nonzero closure phase, which empirically fades as temporal baseline increases [4, 41].

We propose a new approach to finding soil moisture based on a cumulative sum of closure phase.

Because changing soil moisture can produce nonzero closure phase, we hypothesize that the closure phase is correlated to the change in soil moisture. An analogy can be found in interferometric phase. Changing elevation of the ground produces a nonzero interferometric phase corresponding to the changed position of the ground from one acquisition to another. To find displacement over time, this velocity can be integrated (or cumulatively summed) over a time series. Analogously, here we assume that time-varying dielectric properties of the Earth's surface produce a nonzero closure phase, which corresponds to the *change* in the dielectric properties. Because changes in soil moisture (or other volume scatterers) are related to closure phase, we cumulatively sum closure phase over time to derive a time series of soil moisture.

3.1 Model

We present a model of systematic closure phase resulting from volume scattering at different depths in a medium of time-varying bulk dielectric constant. In our model, time variation of soil moisture causes changes in dielectric constant ϵ_r (also called relative permittivity) of the soil between layers. The interference between the independent scattering populations at the surface and subsurface gives rise to non-zero closure phase. The two-scatterer model is the simplest configuration that produces systematic closure phase, and it allows us to easily investigate closure phase processes analytically. Treatments of more complex models[1] can be found in, e.g., [40, 90].

We model the soil dielectric constant as a function of soil moisture at C-band (5.5 GHz) from an average of several soil types found in Cihlar and Ulaby [30]. We assume that the maximum value of soil moisture in that paper, 0.4 g/cm^3, corresponds to total saturation. Fig. 3.3 shows the dielectric constant as a function of soil moisture; we use the convention of a negative imaginary part to ensure attenuation rather than growth during propagation.

Figure 3.4 shows the geometry of the model. The wave partially backscatters from the soil surface and partially propagates into the soil, interacting with volume scatterers in the soil. The effective depth of the phase centers varies with changing dielectric constant. Interference between the surface-scattered and volume-scattered components of the wave returning to the radar produces a signal. We use a simple plane wave model to find the amplitude and phase of the return signal to the radar. The surface reflection has normalized radar cross section σ_s^0, and the subsurface reflection has normalized radar cross section σ_d^0. We assume free space above the surface with dielectric constant unity, while in the medium, the dielectric constant is $\epsilon_r = \epsilon' - j\epsilon''$.

The received signal for a radar system will be the sum of the surface and subsurface reflections and is dependent on the propagation loss and phase shift from two-way travel in the medium. If we normalize the signal such that the phase at the upper surface is 0, the signal received s can be expressed as:

[1] The model here could be produced following [40] with scattering density profile $f(z)$ comprised of δ functions at the surface and subsurface.

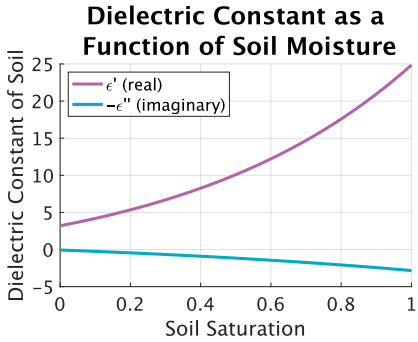

Figure 3.3: Model for relative permittivity (dielectric constant) ϵ_r of soil as a function of soil saturation. We define a gravimetric soil moisture of 0.4 from Cihlar and Ulaby's model as equivalent to a saturation of 1.0 [30].

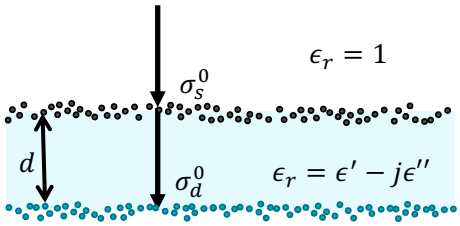

Figure 3.4: Schematic of simple propagation model: Plane wave scatters partially from surface and partially transmits into the soil and scatters from lower surface. Two-way propagation through the soil means that the portion of the return that comes from subsurface scattering has different phase and amplitude properties than the portion that is directly scattered from the soil surface. The soil complex dielectric constant depends on soil composition and soil moisture.

$$s = s_s + s_d e^{-j\frac{4\pi}{\lambda}nd} \tag{3.3}$$

where s_s and s_d, the surface and depth amplitude terms, are random variable draws from complex Gaussian distributions of variance σ_s^0, σ_d^0, $n = \sqrt{\epsilon_r}$, λ is wavelength in a vacuum, and d is the layer depth. For further simplification of the algebra, define a normalized depth $x = \frac{4\pi}{\lambda}d$, then

$$s = s_s + s_d e^{-jnx} \tag{3.4}$$

The signal is thus the sum of the surface echo and a suitably delayed and attenuated subsurface echo. If we have two successive measurements of the same surface, we can form an interferogram, finding the product of the first measurement and the conjugate of the second measurement:

$$\begin{aligned} s_1 s_2^* &= (s_s + s_d e^{-jn_1 x})(s_s^* + s_d^* e^{jn_2^* x}) \\ &= s_s s_s^* + s_s s_d^* e^{jn_2^* x} + s_d s_s^* e^{-jn_1 x} + s_d s_d^* e^{-jn_1 x + jn_2^* x} \end{aligned} \tag{3.5}$$

We have assumed here no decorrelation of either the surface or subsurface echo: if there is any temporal decorrelation, it will simply add uncorrelated noise to our measurement. Equation (3.5) describes the interferogram measurement for a specific single-look pixel; it varies with pixel location because the cross section amplitudes s_s and s_d are statistically varying. If we compute the expected value of the interferogram, which is what results in practice from spatially multilooking the interferogram (assuming independent surface and subsurface scatterers), equation (3.5) reduces to

$$\langle s_1 s_2^* \rangle = \sigma_s^0 + \sigma_d^0 e^{-jn_1 x + jn_2^* x} \tag{3.6}$$

where we have assumed that the complex reflectivities of the surface and subsurface terms are uncorrelated; this assumption allows us to eliminate the cross-terms. From (3.6), we see that the interferogram consists of a surface term plus a delayed and attenuated subsurface term. If the dielectric constant is the same at both measurement times, the real parts of the scaled refractive indices n_i cancel, and the net interferogram phase will be zero. The amplitude of the subsurface term, dependent on the imaginary part of the refractive index, represents the two-way attenuation of the reflected wave. If the dielectric constant varies temporally, then the interferogram phase will be nonzero and will depend on the change in the real part of ϵ_r.

The phase of the expectation of the interferogram in (3.6) is not related to any surface deformation; rather, it results from interference of the subsurface and subsurface echoes. If there is little penetration into the subsurface, as when the imaginary part of the dielectric constant is large, the "fading" signal is negligible, but if there is a substantial subsurface echo, the artifact can be significant.

We now further consider the closure phase of a triplet of interferograms. Even with the fairly simple expression in (3.6), the closure term is complicated enough as to be nonintuitive, but we can write it out in full as:

$$\begin{aligned}
&\langle s_1 s_2^* \rangle \langle s_2 s_3^* \rangle \langle s_3 s_1^* \rangle = \\
&\quad (\sigma_s^0)^3 \\
&+(\sigma_s^0)^2(\sigma_d^0)[e^{-j(n_2 - n_3^*)x} + e^{-j(n_1 - n_2^*)x} + e^{-j(n_3 - n_1^*)x}] \\
&+(\sigma_s^0)(\sigma_d^0)^2[e^{-j(n_1 - n_2^* + n_2 - n_3^*)x} \\
&\qquad + e^{-j(n_2 - n_3^* + n_3 - n_1^*)x} + e^{-j(n_3 - n_1^* + n_1 - n_2^*)x}] \\
&+(\sigma_d^0)^3 e^{-j(n_1 - n_2^* + n_2 - n_3^* + n_3 - n_1^*)x}
\end{aligned} \tag{3.7}$$

This is easily computed given the radar cross sections of the surface and subsurface and the dielectric constant at each measurement time. We plot an example of the triplet phase in Fig. 3.5, for normalized depth values x ranging from 0 to 100, $\sigma_s^0 = \sigma_d^0 = 1$, and for a dielectric constant increasing by 10% for each successive measurement. We find:

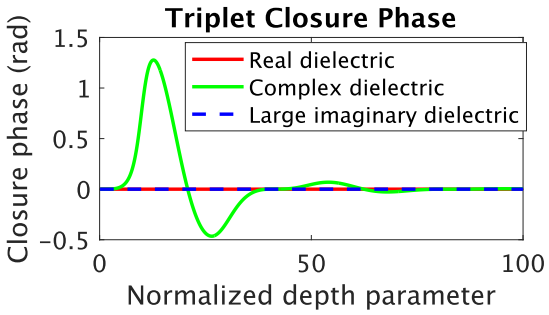

Figure 3.5: Triplet closure phase for three dielectric media. The red curve is for purely real dielectric, green for a "representative" lossy dielectric, and blue for a highly absorptive medium. For the real case, there is no loss and the subsurface term adds in or out of phase with the surface echo, depending on layer depth. The representative lossy case amplitudes fall off slowly with depth such that for shallow layers interference with the surface signal is significant, while for the highly absorptive medium, little subsurface signal is observed.

1. red: purely real dielectric (no loss, $\epsilon_r = 10$). The phase of the subsurface echo changes, but its amplitude does not. It may interfere in or out of phase with the surface, but the closure phase will be zero.

2. green: complex dielectric with an intermediate imaginary part ($\epsilon_r = 10 - j0.2$). The interference signal decreases with depth as the signal attenuates; the closure phase is nonzero and depends on both the layer depth and the dielectric constant.

3. blue: dielectric constant with large imaginary component ($\epsilon_r = 10 - j20$). The return is dominated by the surface term, as the subsurface term rapidly attenuates.

This model demonstrates that we can explain the presence of non-deformational signals in InSAR measurements as interference between a surface and subsurface echo. The interference is sensitive to the dielectric constant of a lossy medium and the depth of any subsurface scatterers.

3.1.1 Simulated Closure Phase Time Series

To test this model, we generate a theoretical time series of soil moisture values, containing rapid increases in soil moisture to simulate rainfall events and gradual dry-downs. Many studies (e.g. [83, 110, 47]) have observed that soil moisture tends to follow this pattern. We generate a soil moisture time series with three rainfall events occuring at 1/8, 3/8, and 3/4 of the way through the time series (the choice of timing is arbitrary) followed by exponential decay. Figure 3.6a shows the example time series of soil moisture, along with the real and imaginary parts of the soil dielectric constant.

We calculate the closure phase from the soil moisture time series displayed in Fig. 3.6a using equation (3.7) with dielectric constants calculated from [30]. Figure 3.6b shows the closure phase

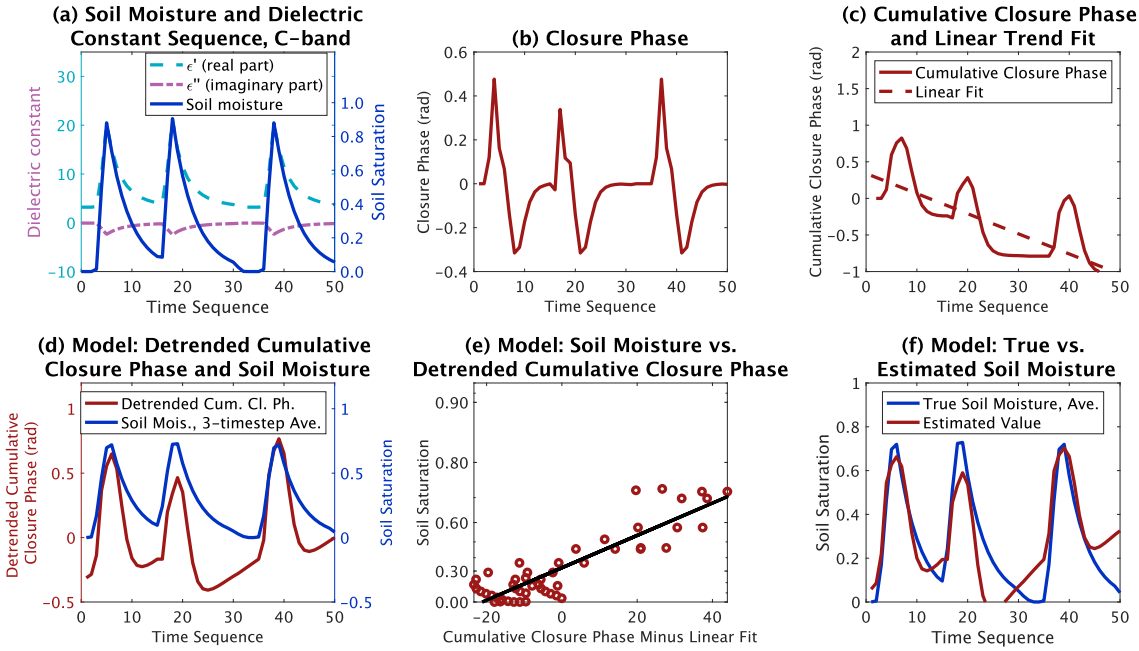

Figure 3.6: (a) Modeled time series of soil moisture (solid blue line), with real and imaginary parts of dielectric constant over time (dashed lines).
(b) Modeled closure phase derived from modeled soil moisture. The peaks are misaligned in time with the peaks in soil moisture, and there are large negative spikes that do not directly correspond to negative spikes in soil moisture.
(c) Cumulative sum of closure phase from model, and fitted trend line. This line is subtracted to find detrended cumulative closure phase.
(d) Detrended cumulative closure phase with soil moisture. Soil moisture is temporally filtered by averaging the three time steps in the closure phase triplet.
(e) Scatter plot on log scale of detrended cumulative closure phase vs. time-averaged soil moisture. The fit line is in black; the correlation coefficent $R = 0.87$.
(f) True soil moisture and estimated soil moisture from the model. The correlation coefficient between estimated and true soil moisture is $R = 0.87$, and the root-mean-square error (RMSE) of the estimated soil moisture is 0.15.

predicted by the modeled soil moisture, given the two-layer model of closure phase expected value. The closure phase in this model does not appear to match the soil moisture; although it exhibits three peaks related to the three rainfall events, there are negative spikes in the closure phase that do not appear in the soil moisture time series.

This result is unsurprising, however, if the closure phase time series corresponds to the *change* in the soil moisture time series – closure phase is a function of the changes in soil moisture among the three dates in the triplet. In this case, a cumulative sum over time of the closure phase corresponds more directly to the soil moisture, rather than to its derivative. The calculation of cumulative closure phase at timestep τ is:

$$\phi_{cumulative_{123}}(\tau) = \sum_{t=0}^{\tau} \phi_{123}(t) \tag{3.8}$$

where $t = 0$ corresponds to the time step of the first triplet. We display the cumulative closure phase calculated from (3.8) in Fig. 3.6c. If we model the soil moisture time series as symmetrically increasing and decreasing at the same rates (e.g. shaped like a sine or triangle wave), there is no trend in the closure phase, as the increasing and decreasing terms in the time series cancel over time. However, a rapid increase followed by a slower decrease in soil moisture produces an increasing trend. The trend is a result of nonlinearity in the modeled closure phase; appendix Section 3.2 derives this result. We show a linear fit to the cumulative closure phase with a dashed line in Fig. 3.6c. To correct for the long-term trend over the full range of measurements, we subtract the fit line to find a signal we call the *detrended cumulative closure phase*.

The detrended cumulative closure phase is derived from triplets acquired over three successive times in the time sequence. To compare the soil moisture with this signal, we therefore average the soil moisture across the three time steps that the closure phase includes. Figure 3.6d shows the detrended cumulative closure phase in red and the three-time step averaged soil moisture in blue.

The detrended cumulative closure phase time series is correlated with the soil moisture time series. The peaks in soil moisture are aligned with the troughs in detrended cumulative closure phase. Figure 3.6e shows a scatter plot of modeled soil moisture vs. detrended cumulative closure phase; the correlation coefficient between the two quantities is $R = 0.87$. The scatter plot and fit line are both relative to soil moisture fraction on a log scale. We use the fit line from Fig. 3.6e to generate an estimate for soil moisture, shown in Fig. 3.6f. The estimate has a root-mean-square error of 0.15, and the correlation coefficient between estimated and true soil moisture is also $R = 0.87$.

Next, we will explore how this model can lead to a long-term trend in InSAR data.

3.2 Nonlinearity and Apparent Bias in the Closure Phase Model

Equation 3.7 shows an equation for closure phase in terms of the changing dielectric constant of a medium. We expand a Taylor series of the exponentials in Eq. 10:

$$e^{-z} = 1 - z + \frac{z^2}{2} + ... \tag{3.9}$$

We calculate the first-order ($e^{-z} \approx 1 - z$) expansion for shallow depth ($x \sim 10^{-4}$). Eq. 3.7 becomes:

$$\begin{aligned}
&\langle s_1 s_2^* \rangle \langle s_2 s_3^* \rangle \langle s_3 s_1^* \rangle \approx (\sigma_s^0)^3 \\
&+(\sigma_s^0)^2(\sigma_d^0)[(1 - j(n_2 - n_3^*)x) + (1 - j(n_1 - n_2^*)x) \\
&\qquad + (1 - j(n_3 - n_1^*)x)] \\
&+(\sigma_s^0)(\sigma_d^0)^2[(1 - j(n_1 - n_2^* + n_2 - n_3^*)x) \\
&\qquad + (1 - j(n_2 - n_3^* + n_3 - n_1^*)x) \\
&\qquad + (1 - j(n_3 - n_1^* + n_1 - n_2^*)x)] \\
&+(\sigma_d^0)^3[1 - j(n_1 - n_2^* + n_2 - n_3^* + n_3 - n_1^*)x]
\end{aligned} \tag{3.10}$$

We also define real and imaginary parts of the refractive index $n_k = n_k' - jn_k''$. Then the closure phase simplifies significantly:

$$\begin{aligned}
\langle s_1 s_2^* \rangle \langle s_2 s_3^* \rangle \langle s_3 s_1^* \rangle &\approx (\sigma_s^0)^3 \\
&+(\sigma_s^0)^2(\sigma_d^0)[3 - 2(n_1'' + n_2'' + n_3'')x] \\
&+(\sigma_s^0)(\sigma_d^0)^2[3 - 4(n_1'' + n_2'' + n_3'')x] \\
&+(\sigma_d^0)^3[1 - 2(n_1'' + n_2'' + n_3'')x]
\end{aligned} \tag{3.11}$$

This simplification shows that the first-order approximation of the closure phase has no imaginary component, and therefore its phase is always zero. Any closure phase therefore results from higher-order terms, explaining the nonlinearity we observe in our model and in our results (this nonlinearity is also observed in, e.g. [39, 13]).

Indeed, with the small-x approximation, the second-order term is responsible for most of the closure phase observed in a time series, and produces a biased closure phase that, when cumulatively summed, gives rise to a trend. Figure 3.7a shows the cumulative closure phase calculated from our exponential model, from the first-order ($1-z$) approximation, and from the second-order ($1-z+\frac{z^2}{2}$) approximation.

Figure 3.7b shows the cumulative closure phase; again, the second-order approximation matches the full exponential model, while the first-order approximation does not produce non-zero closure

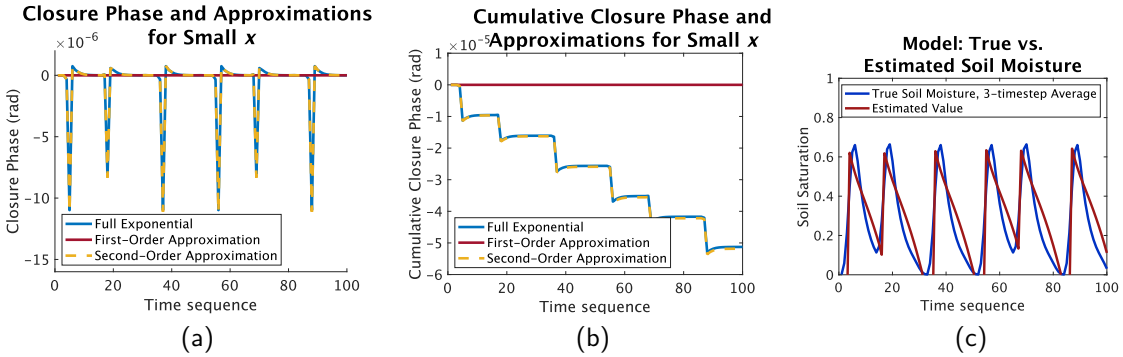

Figure 3.7: (a) Time series of closure phase with first- and second-order approximations to the exponentials for small x. The first-order approximation is entirely real, so the closure phase is always zero. (b) Time series of cumulative closure phase, with first- and second-order approximations. (c) True and estimated soil moisture for sample time series demonstrating the nonlinear response of closure phase to changing dielectric constant.

phase. Figure 3.7c shows the time series of soil moisture that produced these closure phases, as well as the estimate of that soil moisture from our methods.

The second-order approximation is significantly more complex to write out, but what emerges from it is that the imaginary part of the signal relies on higher-order powers of the change in dielectric constant. Taking one term as an example,

$$e^{-j(n_1-n_2^*)x} \approx 1 - j(n_1 - n_2^*)x - \frac{x^2}{2}(n_1 - n_2^*)^2 \tag{3.12}$$

We have shown that the $1 - j(n_1 - n_2^*)x$ terms will produce only real components. Any imaginary component of the triplet signal is therefore a function on the order of n_k^2 (or higher powers).

Because of this $O(n^2)$ proportionality for small x, a different rate of change of the dielectric constant in a triplet will result in drastically different closure phases. Doubling the change of dielectric constant in a triplet results in a fourfold change in the imaginary part of the triple product expected value (which produces the non-zero phase), while a tenfold difference in dielectric constant change would cause a hundredfold difference in the imaginary part. For larger x, higher-order terms may dominate (for example, [39] found a third-order approximation worked well in their results).

The result of this nonlinear relationship is that, if soil moisture increases and decreases at similar rates, the positive and negative closure phases will approximately cancel out, resulting in no bias. Of course, if these rates are exactly the same,

$$\phi_{123}(n_1, n_2, n_3) = -\phi_{123}(n_3, n_2, n_1) \tag{3.13}$$

That is to say, an exactly symmetric increase and decrease in soil moisture will produce a non-zero

closure phase, but will *not* produce a trend because the two values will cancel out over a time series.

However, if soil moisture rapidly increases to saturation, and then decreases to dryness over many smaller time steps, then the closure phase produced by the rapid increase would dominate over the smaller changes. Visually, this can be seen in the closure phase time series: the largest changes tend to produce the spikes in closure phase. Therefore, the bias in the closure phase and the trend in the cumulative closure phase result from asymmetric increases and decreases in dielectric constant that feed into a nonlinear function.

In Fig. 3.8 and 3.9, we show the first, middle, and last items in a set of simulated soil moisture time series going from asymmetric with rapid ascents and slow descents, to symmetric, to slow ascents and rapid descents. In the second row of each plot, we show the cumulative closure phase associated with each: the more asymmetric time series lead to a steeper trend in cumulative closure phase (and higher systematic bias in closure phase), while the symmetric time series has no trend or bias. This holds true for different soil moisture patterns; Fig. 3.8 shows a sinusoidal pattern, while Fig. 3.9 shows a triangle wave pattern. Figure 3.10 shows the slope of the cumulative closure phase, as a function of the symmetry. For a symmetric pattern of ascending and descending, the slope is 0, but asymmetry in either direction produces a trend. Where changes in both directions are gradual (up to ±25% more pixels ascending than descending in this plot), the slope seems to follow a smooth curve; beyond that, the edge cases surrounding the transitions from ascending to descending likely produce the less smoothly varying slopes [153].

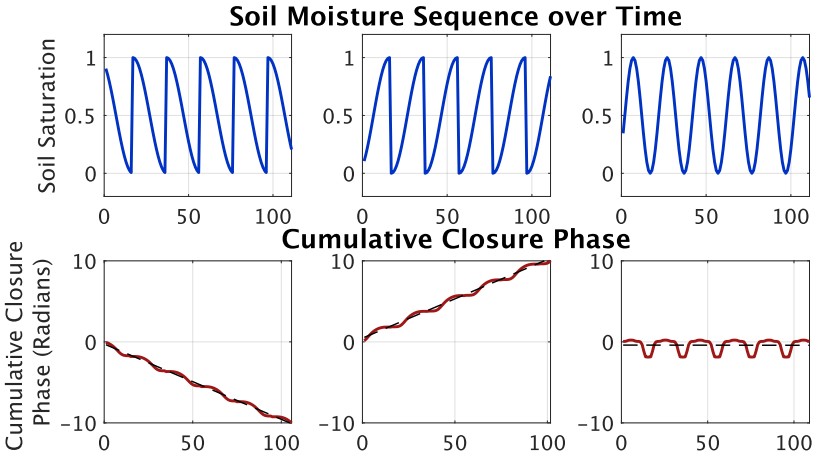

Figure 3.8: Soil moisture time series made up of sine waves with varying degrees of symmetry, and the resultant cumulative closure phase time series.

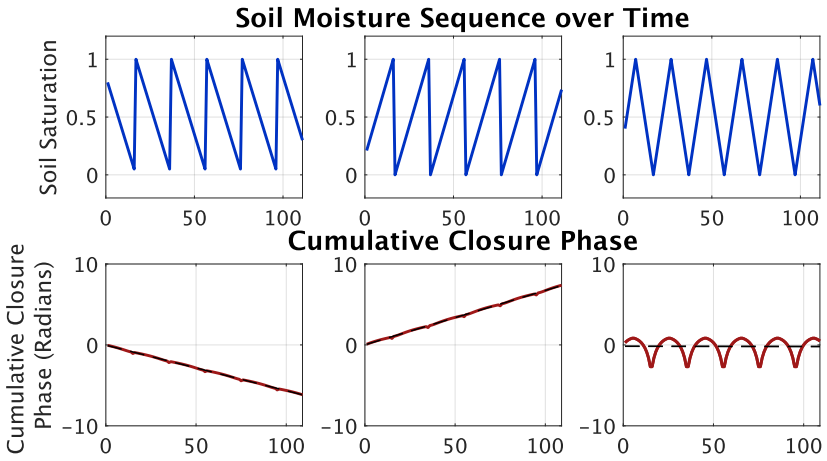

Figure 3.9: Soil moisture time series made up of triangle waves with varying degrees of symmetry, and the resultant cumulative closure phase time series.

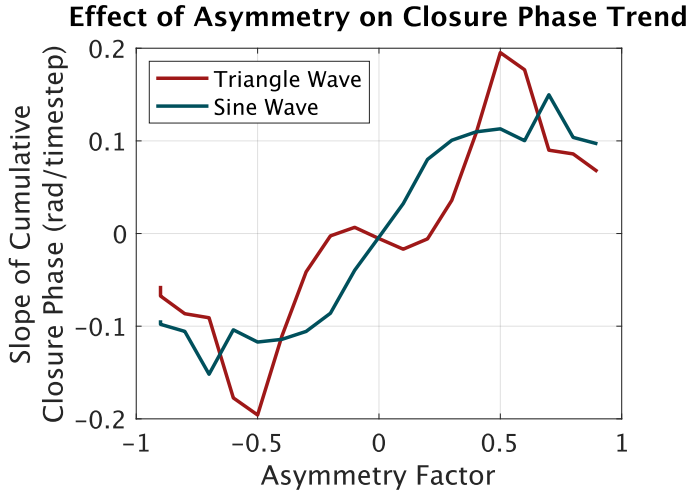

Figure 3.10: Slope of cumulative closure phase as a function of asymmetry, where degree of symmetry is determined by percentage of pixels ascending and descending for triangle and sine-shaped waves. 0 represents equal ascending or descending, +50 is 100% ascending, and −50 is 100% descending.

3.3 Modeled Closure Phase from a Real Soil Moisture Time Series

While so far this chapter has mostly shown soil moisture time series for idealized sequences of identically increasing and decreasing patterns of soil moisture, these changes are more varied in the real world. To display the range of possible outcomes of modeling, we show two plots of realistic soil moisture time series (in fact, these draw from real soil moisture time series in Acme and Norman, Oklahoma, discussed in Chapter 4) and discuss possible model outcomes.

Figure 3.11 shows the results of our model for a real soil moisture time series from the Acme site. At this site, the modeled detrended cumulative closure phase is correlated with soil moisture, and can be used to estimate soil moisture with reasonable accuracy (correlation coefficient between estimated and true soil moisture is 0.69, and RMSE error is 0.15). Figure 3.12 shows the model results at the Norman site. Here, the modeled detrended cumulative closure phase is actually *anti*-correlated with the soil moisture, with a correlation coefficient of $R = -0.55$. Nonetheless, we can still linear-regress the two to find an estimate for soil moisture, which has an RMSE of 0.22. The results from these two real soil moisture time series demonstrate that the model can estimate closure phase and retrieve soil moisture over the time series found in the data, which are saturated for extended periods and exhibit some seasonality. Moreover, this shows that, while closure phase can be generated by soil moisture, the nature of the relationship (positive versus negative correlations, for instance) may vary. In the next few chapters, we will examine some cases where moisture time series are both positively and negatively correlated with soil moisture.

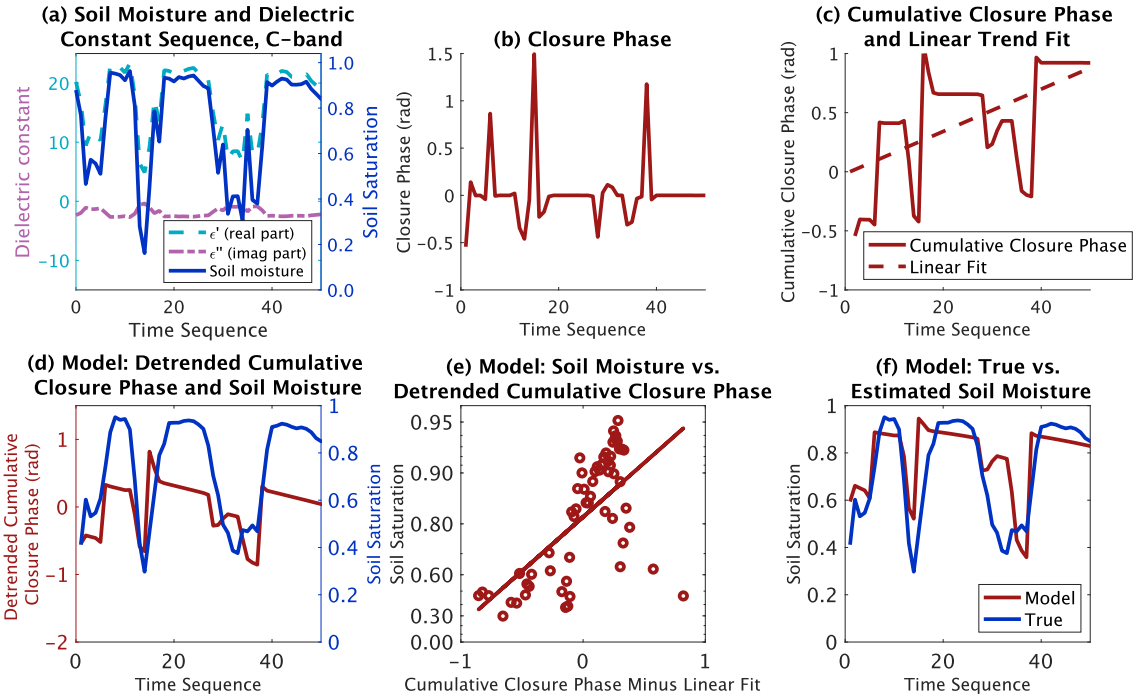

Figure 3.11: (a) Real time series of soil moisture at Acme Mesonet site (solid blue line), with real and imaginary parts of modeled dielectric constant over time (dashed lines).
(b) Modeled closure phase derived from Acme soil moisture.
(c) Cumulative sum of closure phase from model, and fitted trend line. This line is subtracted to find detrended cumulative closure phase.
(d) Detrended cumulative closure phase from model, with Acme soil moisture. Soil moisture is temporally filtered by averaging the three time steps in the closure phase triplet.
(e) Scatter plot on log scale of detrended cumulative closure phase vs. time-averaged soil moisture. The fit line is in black; the correlation coefficent $R = 0.65$.
(f) Soil moisture and estimated value from the model. The root-mean-square error (RMSE) of the estimated soil moisture is 0.15, and the correlation coefficient betwen measured and estimated soil moisture is $R = 0.69$.

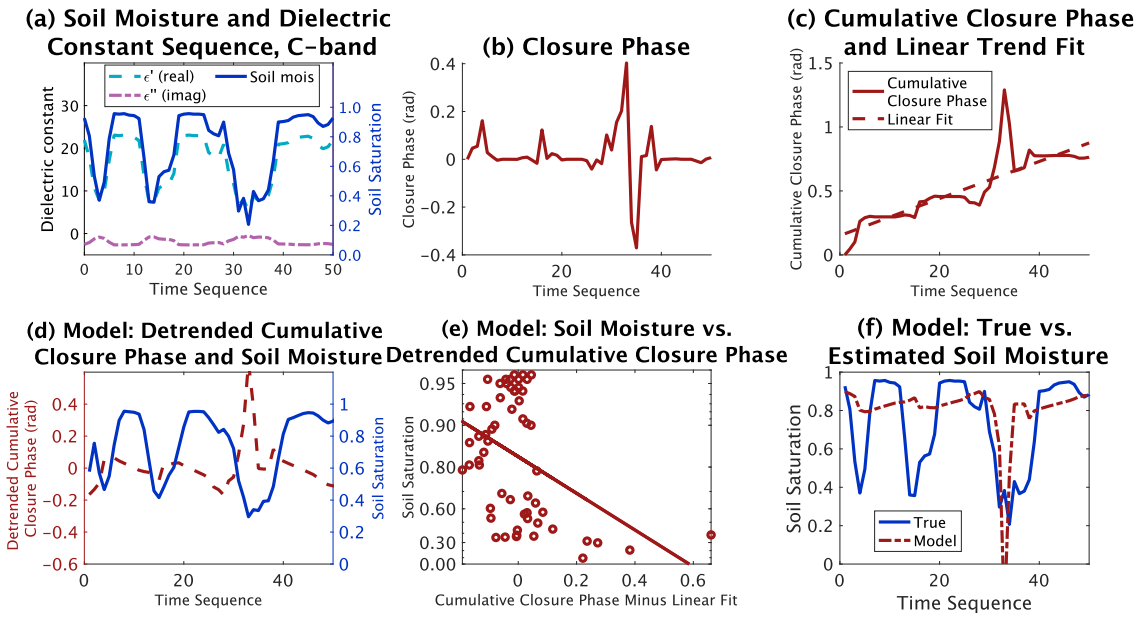

Figure 3.12: (a) Real time series of soil moisture at Norman Mesonet site (solid blue line), with real and imaginary parts of modeled dielectric constant over time (dashed lines).
(b) Modeled closure phase derived from Norman soil moisture.
(c) Cumulative sum of closure phase from model, and fitted trend line. This line is subtracted to find detrended cumulative closure phase.
(d) Detrended cumulative closure phase from model, with Norman soil moisture. Soil moisture is temporally filtered by averaging the three time steps in the closure phase triplet.
(e) Scatter plot on log scale of detrended cumulative closure phase vs. time-averaged soil moisture. The fit line is in black; the correlation coefficent $R = -0.55$.
(f) Soil moisture and estimated value from the model. The root-mean-square error (RMSE) of the estimated soil moisture is 0.22.

Chapter 4

Fine-Resolution Measurement of Soil Moisture from Cumulative InSAR Closure Phase

Note: This chapter is adapted from a paper coauthored with Howard Zebker and Roger Michaelides [134].

4.1 Background: Soil Moisture Sensing

The proportion of liquid water in soil can be measured by weight or by volume. Gravimetric soil moisture compares the weight of water in soil to the weight of dry soil; it is used in some soil moisture models [30]. Volumetric soil moisture relates the volume of water in soil to the total volume of soil and is used for measurements from the Soil Moisture Active Passive (SMAP) satellite [37]. Soil saturation relates the volume of water to the volume of pore space; it varies between 0 and 1 [1]. The *in situ* Mesonet system in Oklahoma uses a fractional water index related to saturation [61]. All three of these metrics are linearly proportional; gravimetric and volumetric measurements are related through the bulk density of dry soil, and saturation relates to volumetric soil moisture through the porosity. In this paper, we convert all measurements to saturation for comparison with a straightforward 0 to 1 scale.

Passive remote sensing of soil moisture is limited in resolution to the footprint of a radio antenna; the SMAP radiometer has a native resolution of 36 km [22, 7]. *In situ* measurements may have a smaller footprint, but often have incomplete spatial coverage reliant on the installation and upkeep of sensors. Active remote sensing of soil moisture can deliver higher resolution ($\sim$ 10 m) and more complete spatial coverage.

4.2 Methods

We compare cumulatively-summed closure phase to measured soil moisture at an InSAR swath across the middle of Oklahoma (Fig. 4.1). The Mesonet system of environmental monitoring systems [19] provides daily *in situ* soil fractional water index at 5 cm depth at 37 sites across this swath. Fractional water index varies between 0.00 for very dry soil to 1.00 for fully saturated soil; we interpret it as saturation [61]. To account for variations in soil moisture, and because the InSAR phase triplets were acquired over periods of at least 24 days (three passes with a 12-day typical repeat cycle), we temporally average the soil moisture measurements across 31 days centered on the date of the middle image in the phase triplet. Each InSAR triplet spans almost a month; this temporal averaging starts three days before the first date in the triplet and ends three days after the last in order to find an average value representative of all three dates.

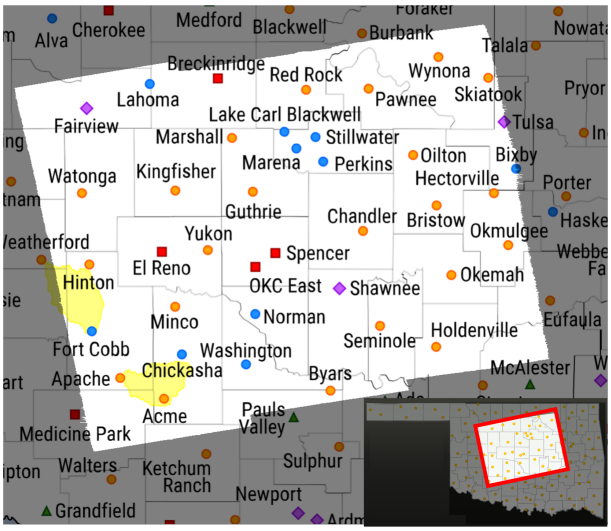

Figure 4.1: Location of 37 Mesonet ground sites and InSAR swath (highlighted region) in Oklahoma. Map image from Oklahoma Mesonet website [19]. The dot colors and shapes correspond to organizations that administer the sites and are not relevant to this study.

Fig. 4.2 shows a flowchart of our process. We derive the phase triplets from raw L0 Sentinel-1 data ($\lambda = 5.5$ cm) using the Stanford InSAR processor [141], which we process using 50x20 looks in range and azimuth, respectively, for a final pixel size of approximately 300x300 m [34]. We apply an additional spatial averaging filter of M pixels over the multilooked closure phase; empirically, this results in stronger correlations between soil moisture and closure phase (see Fig. 4.9 in the Results section). Unless otherwise specified, the results presented use $M = 81$ (9x9 square filter). A comparison of parameters is discussed in Section 4.3.2, where we use squares centered on the pixel with side lengths of 1, 5, 7, 9, and 29 ($M = 1, 25, 49, 81, 841$).

To construct phase triplets, we use only time-adjacent data, so that the temporal baselines are

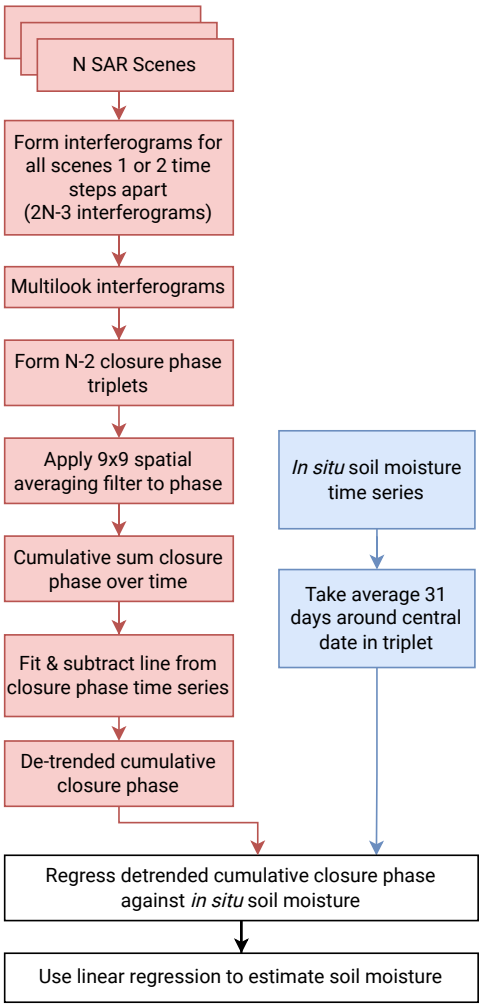

Figure 4.2: Flowchart of data reduction approach

short. Since we are using Sentinel-1 data, the temporal baseline between two SAR images is generally ~ 12 days, so the time across the whole consecutive phase triplet is generally ~ 24 days. Occasional gaps in Sentinel coverage, such as a several-month gap in winter 2019, led to a few triplet sets in our study area including longer temporal baselines. Shorter temporal baselines are preferable for this study, since they empirically produce a larger phase misclosure.

If we cumulatively sum the closure phase over time, the signal exhibits an increasing trend over time at nearly all sites, consistent with our model. The trend emerges from a nonlinear relationship between changing soil moisture and InSAR phase; see Section 3.2 for a mathematical explanation. Differing rates of wetting and drying drive the trend here and in our model. We remove this consistent upward trend by fitting and subtracting a line from each cumulatively-summed closure phase. We can then compare the detrended cumulative closure phase to the *in situ* soil moisture. We compare the detrended cumulative closure phase to the soil moisture by calculating the correlation coefficient R between the two time series (where they are anticorrelated, an R closer to -1 indicates a higher degree of correlation). We also perform a linear fit between the soil moisture (measured on a logarithmic scale) and the closure phase. This linear fit is used to estimate the soil moisture. We evaluate this estimate using the root-mean-square error (RMSE) as well as the correlation coefficient; together, these inform us of both absolute and relative accuracy of the estimates.

We use extended triple collocation to estimate the accuracy of the soil moisture estimates [119, 82]. We compare three independent measurement systems: the estimated soil moisture derived from detrended cumulative closure phase (using Sentinel-1 C-band InSAR phase data), the 9-km enhanced SMAP passive soil moisture product (which uses L-band radiometry to measure brightness temperature of the ground [22]), and the Mesonet *in situ* soil moisture measurements, which use heat dissipation sensors [150]. We assume, because the remote sensing methods use different methodologies (passive/active, phase/amplitude) and different wavelengths, that their errors are independent of each other and of the errors in the *in situ* measurement system.

4.3 Results

Figure 4.3a shows the cumulative closure phase at all 37 sites. We fit a trend line to each and then subtract the fitted signal. Figure 4.3b shows the fitted line with the cumulative closure phase at the Seminole site.

Figure 4.4 shows the detrended cumulative closure phase plotted with the soil moisture for the Seminole site. The two quantities appear anticorrelated. The detrended cumulative closure phase approximately tracks *in situ* data.

We create a scatter plot of the two parameters graphed in Fig. 4.4 with soil moisture on a log scale (Fig. 4.5). We then fit a line to the scattered data and use the fit line to estimate soil moisture from the closure phase, shown in Fig. 4.6. While the estimate does not track the *in situ* data exactly,

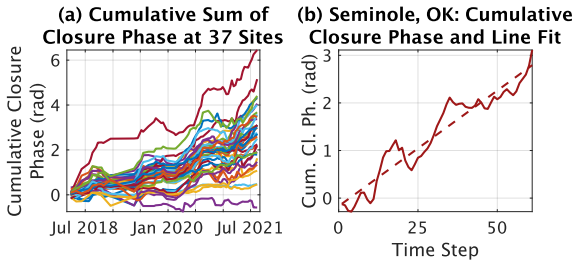

Figure 4.3: (a) At almost all sites, closure phase exhibits an increasing trend, suggesting some type of bias in the signal. (b) We fit and subtract a line to detrend the cumulative closure phase.

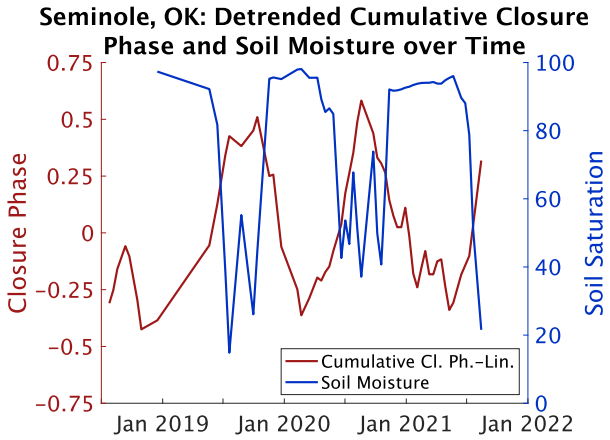

Figure 4.4: Detrended cumulative closure phase appears to be strongly anticorrelated with soil moisture.

particularly at times with very low soil moisture, the estimate does appear to identify accurately when soil moisture is increasing and decreasing. The correlation coefficient between measured and estimated soil moisture at the Seminole site is $R = 0.76$ and the RMSE (root-mean-square error) of the estimated soil moisture is 0.16.

While the Seminole site analysis retrieves an overall fairly accurate estimate of soil moisture from closure phase, other sites in the same swath have more mixed results. Figures 4.7a and 4.7c show the scatter plot match between detrended cumulative closure phase and soil moisture at two other sites, Lahoma and Hinton. These locations have a much weaker correlation between the detrended cumulative closure phase and the soil moisture. The corresponding estimates, shown in Fig. 4.7b and 4.7d, are consequently less accurate. The Lahoma site demonstrates an intermediate fit quality close to the mean of all sites, with a good estimate during some time periods but not others. The correlation coefficient between detrended cumulative closure phase and soil moisture at Lahoma is $R = -0.40$ and the RMSE of the estimated soil moisture is 0.18. The Hinton site represents a poor quality of fit, with correlation coefficient between detrended cumulative closure phase and soil

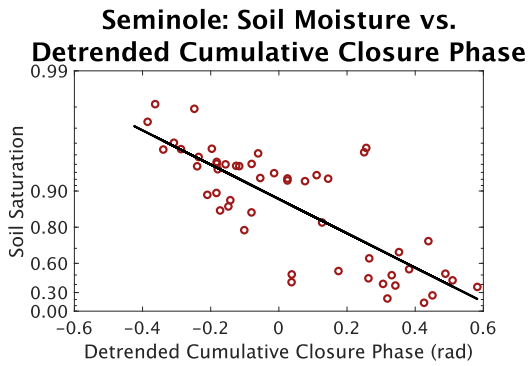

Figure 4.5: Scatter plot on log scale of detrended cumulative closure phase vs. soil moisture. The detrended cumulative closure phase appears to have a strong correlation with soil moisture ($R = -0.77$).

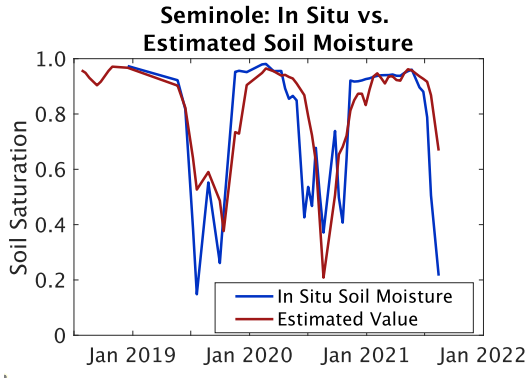

Figure 4.6: The estimate of soil moisture based on closure phase at the Seminole site appears to track true soil moisture quite closely, though it does not always capture areas of low soil moisture. The correlation coefficient between measured and estimated soil moisture is $R = 0.76$ and the RMSE is 0.16.

moisture of $R = -0.15$ and RMSE of 0.23.

The most-correlated site using this data set and method (50x20 looks; 31-day average of *in situ* soil moisture surrounding the center date in the triplet; 9x9 spatial filter of detrended cumulative closure phase) is Seminole, which has a correlation coefficient between detrended cumulative closure phase and soil moisture of $R = -0.77$. The least-correlated site has a correlation coefficient of -0.03; 35 of the 37 sites have anticorrelations between soil moisture and detrended cumulative closure phase; the other two have a slight positive correlation. The mean correlation coefficient between detrended cumulative closure phase and soil moisture is -0.35; the mean amplitude of the correlation coefficient (so that positive and negative correlations do not cancel) is 0.37. The mean correlation coefficient between measured and estimated soil moisture is 0.36; the mean RMSE is 0.18. Table 4.1 shows the quality of fit between measured and estimated soil moisture via correlation coefficient R and RMSE

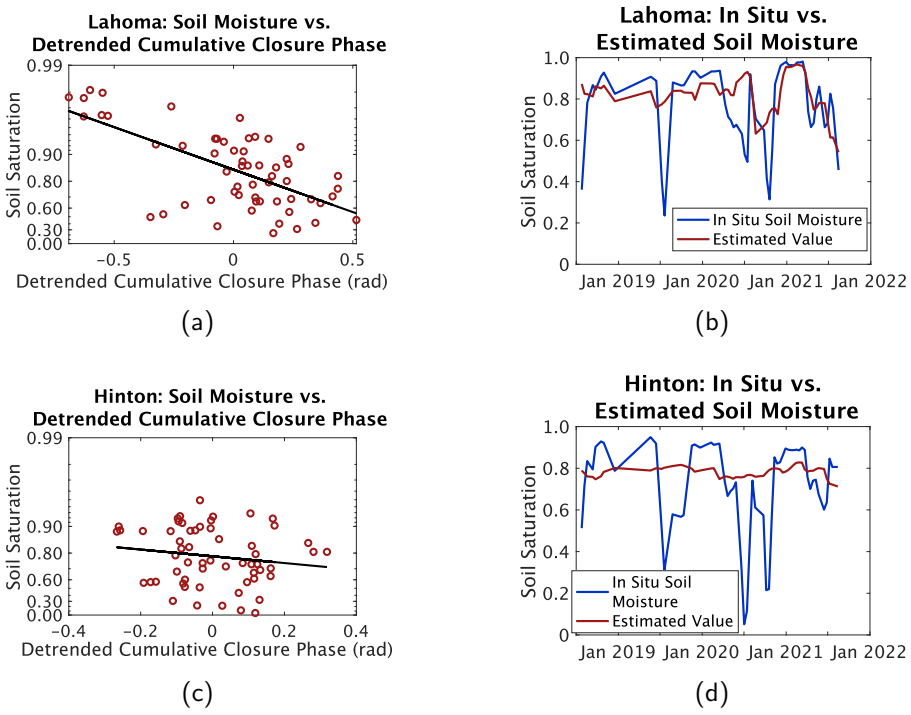

Figure 4.7: (a) The Lahoma site has a weaker correlation between the closure phase parameter and the soil moisture ($R = -0.40$). (b) Estimation at the Lahoma site does not perform as well. The estimate seems to loosely track the shape of the soil moisture, but does not estimate it accurately. The correlation coefficient between measured and estimated soil moisture is $R = 0.41$ and the RMSE is 0.18. (c) The Hinton site has nearly no correlation between the closure phase parameter and the soil moisture ($R = -0.15$). (d) Estimation at the Hinton site is unsuccessful. The correlation coefficient between measured and estimated soil moisture is $R = 0.11$ and the RMSE is 0.23.

for each site, as well as the land cover type at each site.

4.3.1 Standardizing the Fit between Soil Moisture and Detrended Cumulative Closure Phase

For this study, we are able to examine a large number of ground stations and individually match each detrended cumulative closure phase to soil moisture, but in most locations, we would not have so much *in situ* data available. Therefore, it would be useful to find a more universal connection between the InSAR data and the soil moisture.

Figures 4.5, 4.7a, and 4.7c show three examples of fit lines between detrended cumulative closure phase and soil moisture. While the *in situ* soil moisture time series generally are anticorrelated with the detrended cumulative closure phase, the optimal fit line for each site is slightly different. However, we can compare the fit lines across all sites to find an "average" conversion from closure phase to soil moisture. Figure 4.8 shows all fit lines plotted on the same graph, with their thickness set by the absolute value of the correlation coefficient between measured and estimated soil moisture.

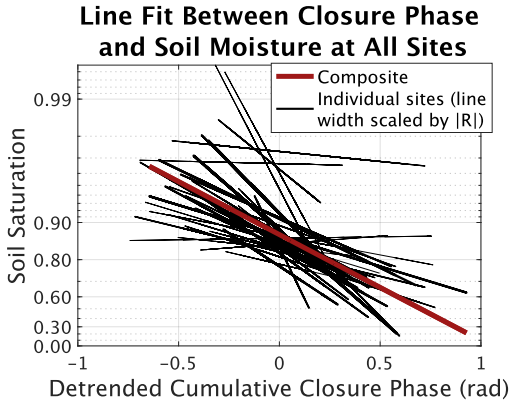

Figure 4.8: Fit lines between soil moisture and detrended cumulative closure phase at all sites in black lines; line thickness corresponds to correlation coefficient. Data from all sites with correlation between measured and estimated soil moisture $R > 0.5$ (eight sites in total) were used to generate the composite fit line in red.

The red line shows the fit line using data from all sites with correlation coefficient $R > 0.5$; eight of the 37 sites exceed this threshold. We choose to exclude the sites with weaker correlations from contributing to the composite line, since data fit from those sites are less likely to represent any true signal. Next, instead of using the tailored site-specific fit lines to estimate soil moisture from closure phase, we test using the same composite line across all sites.

When using the individually tailored fit lines, the correlation coefficient between measured and estimated soil moisture across all sites is $R = 0.36$. When using the composite fit line, the average correlation coefficient is also 0.36. This suggests that a factor converting closure phase to estimated

Table 4.1: Correlation coefficient R and RMSE between measured and estimated soil moisture at each site

Site	**Land Cover**	**R**	**RMSE**
Acme	Grasslands	0.57	0.19
Apache	Grasslands	0.44	0.18
Breckinridge	Grasslands	0.19	0.20
Bristow	Pasture	0.61	0.12
Byars	Pasture	0.33	0.21
Chandler	Pasture	0.47	0.16
Chickasha	Crops	0.24	0.27
El Reno	Grasslands	0.11	0.19
Fairview	Crops	0.24	0.19
Fort Cobb	Crops	0.38	0.15
Guthrie	Grasslands	0.49	0.20
Hectorville	Pasture	0.40	0.18
Hinton	Grasslands	0.11	0.23
Holdenville	Pasture	0.52	0.19
Kingfisher	Grasslands	0.40	0.22
Lahoma	Grasslands	0.41	0.18
Lake Carl Blackwell	Scrub	0.05	0.20
Marena	Grasslands	0.19	0.19
Marshall	Grasslands	0.17	0.25
Minco	Grasslands	0.59	0.15
Norman	Grasslands	0.46	0.26
Oilton	Pasture	0.32	0.18
OKC East	Developed	0.02	0.17
Okemah	Pasture	0.34	0.19
Okmulgee	Pasture	0.55	0.16
Pawnee	Grasslands	0.41	0.20
Perkins	Crops	0.30	0.15
Red Rock	Grasslands	0.50	0.18
Seminole	Grasslands	0.76	0.16
Shawnee	Grasslands	0.33	0.20
Skiatook	Pasture	0.65	0.12
Spencer	Grasslands	0.51	0.10
Stillwater	Grasslands	0.30	0.20
Washington	Pasture	0.28	0.17
Watonga	Grasslands	0.35	0.20
Wynona	Grasslands	0.09	0.20
Yukon	Grasslands	0.42	0.16
Average		**0.36**	**0.18**

Table 4.2: Mean correlation R between estimated and measured soil moisture, averaged across all 37 sites

Fit type	50x20 looks	25x10 looks
Individual line fit	0.36	0.28
Composite line fit	0.36	0.26

Table 4.3: RMSE between estimated and measured soil moisture, averaged across all 37 sites

Fit type	50x20 looks	25x10 looks
Individual line fit	0.185	0.193
Composite line fit	0.194	0.206

soil moisture could be applied broadly across sites in a region, without unduly damaging estimation quality. It is promising that the detrended cumulative closure phase behaves similarly enough across different sites that one simple linear-fit equation can be used to estimate soil moisture throughout the swath.

4.3.2 Variation of results with different processing parameters

We have shown that we can estimate soil moisture from detrended cumulative closure phase at some sites with significant (50x20 looks) multilooking of the triplet images, a 31-day average of *in situ* soil moisture, and a 9x9 spatial filter over the multilooked closure phase image. The choice of parameters is subjective, and other values may also produce good results.

Here, we compare variations in several processing parameters: we compare 50x20 looks (∼300x300 m pixel size) to 25x10 looks (∼150x150 m pixel size), both for the individual line fit at each site and the composite fit across all sites. The composite fit is calculated from sites with $R = 0.50$ for all sites with 50x20 looks, and $R = 0.40$ for 25x10 looks (the threshold is reduced in order to increase robustness; a threshold of 0.40 incorporates data from 11 sites, while a threshold of 0.50 only includes 2 sites at 25x10 looks). For this analysis, a 9x9 spatial filter over the closure phase and a 31-day temporal filter on *in situ* soil moisture apply. Table 4.2 shows the mean correlation coefficient between estimated and measured soil moisture using each method.

Some sites perform noticeably better with 25x10 looks, others with 50x20. The Seminole site has a correlation coefficient between measured and estimated soil moisture of $R = 0.76$ with 50x20 looks, while with 25x10 looks, the coefficient degrades to $R = 0.26$. Conversely, the Byars site has correlation coefficients of $R = 0.33$ with 50x20 looks and $R = 0.64$ with 25x10. In most cases, more multilooking tends to produce a better estimate for soil moisture.

Table 4.3 shows the RMSE between measured and estimated soil moisture, which varies across processing parameters similarly to the correlation coefficient.

Using 50x20 looks, Fig. 4.9 shows how varying the temporal averaging of soil moisture measurements and spatial averaging of closure phase affects the quality of soil moisture estimates. The average correlation coefficient between measured and estimated soil moisture at all sites is plotted against the number of days temporally averaged, with each line representing a different amount of spatial averaging. More temporal averaging smooths the soil moisture time series, which improves the fit; too much temporal averaging may lead to oversmoothing and artificially high correlations. The spatial averaging of closure phase (distinct from multilooking, which is calculated before the triple multiplication) at each time step leads to better fit quality as well. While this smooths the image, it does not necessarily lead to oversmoothing across time steps. With no spatial or temporal averaging, the correlation coefficient is 0.21; with more, it can reach 0.54. For reference, SMAP has an average correlation coefficent between remotely sensed and *in situ* soil moisture data at each site of $R = 0.67$ across these sites and dates. While the parameters used here are promising, optimizing these selections remains an open question.

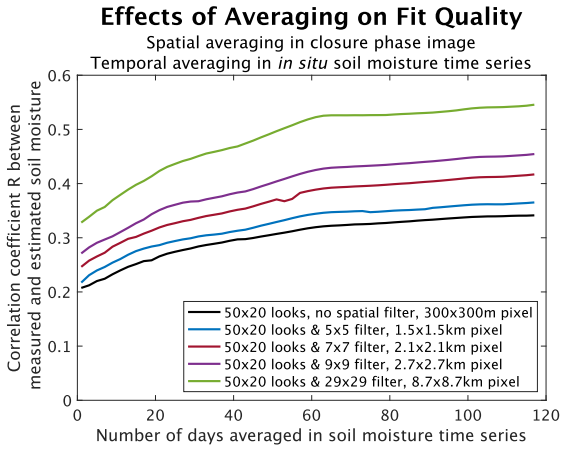

Figure 4.9: Plot showing how temporal averaging of soil moisture time series and spatial averaging of closure phase image affect fit quality across all sites. Generally, more averaging corresponds to a better fit.

4.3.3 Triple collocation

We use extended triple collocation with closure phase, SMAP, and the *in situ* soil moisture measurements to determine how well-correlated all three are to the "true" soil moisture signal [82]. We average the soil moisture measurements only on days where there is a SMAP acquisition within 30 hours of the Sentinel-1 acquisition. For the three acquisition times in each phase triplet, we find the nearest-in-time SMAP overpass and daily average soil moisture from Mesonet at each site. The closure phase is spatially averaged with a 29x29 pixel filter to yield 8.7x8.7 km pixels (multilooking of 50x20 looks is applied prior to calculating the closure phase), similar in scale to the enhanced

SMAP product's 9 km pixel size. We average the SMAP and Mesonet data at the three acquisition times in each triplet. We estimate soil moisture at all sites and all times for each method, and compare the three methods. We calculate saturation from SMAP's measurement of volumetric soil moisture and the U.S.G.S. Soil Properties dataset's measurement of porosity [16]. The *in situ* Mesonet data has a correlation coefficient of $R = 0.83$ with the true soil moisture signal, the SMAP data has a correlation coefficient of $R = 0.78$, and the estimated soil moisture from closure phase has a correlation coefficient of $R = 0.59$.

While the correlation between soil moisture estimated from closure phase and true soil moisture is weaker than that found from the *in situ* data or from SMAP, the closure phase product is highly correlated at some sites, and it delivers a finer and denser spatial resolution than either other method. There may be locations where the soil moisture estimate from detrended cumulative closure phase outperforms SMAP. For example, at the Yukon site, the estimated correlation between closure phase and true soil moisture (using extended triple collocation) is $R = 0.62$, while the estimated correlation between SMAP and true soil moisture is only $R = 0.48$ (the estimated correlation between the *in situ* measurement and true soil moisture is $R = 0.90$ at this site). Moreover, the closure-phase-derived estimate produces a better match to the *in situ* soil moisture ($R = 0.56$) than the SMAP measurement produces ($R = 0.53$). Between SMAP and the closure phase-derived estimate, $R = 0.31$. Figure 4.10 shows the estimated soil moisture from the *in situ* measurement (averaged over the three days of triplet acquisition), the SMAP data (also averaged across the three days of triplet acquisition), and the estimated soil moisture from detrended cumulative closure phase (with spatial averaging to 8.7 km square pixels to match the scale of SMAP). The SMAP data is scaled by its porosity, 0.41, found from the U.S.G.S. Soil Properties dataset, to calculate saturation [16]. Because this measurement appears to underestimate the fractional water index found by the *in situ* sensors, we also plot a dotted line where we scale with a porosity of 0.28 (this value was chosen to improve the match to the *in situ* measurements). The triple collocation results at the Yukon site show that the closure phase can estimate the true soil moisture more accurately than the SMAP measurement.

4.3.4 Variation of results with vegetation and land cover type

There is some correspondence between soil moisture estimate quality and terrain type. Figure 4.11 shows a land cover map of the swath, with a circle at each site colored to represent the quality of fit between the measured and estimated soil moisture. The best fits are largely at the right (east), where forest and pasture land cover types dominate, while the worst are along a roughly vertical line toward the west, where cultivated crops are the most prevalent land cover type. Grouping the sites into east and west with a dividing line at $-96.8°$ longitude, the eastern sites have an average correlation coefficient between measured and estimated soil moisture of $R = 0.46$, while the western sites have an average of $R = 0.32$. As for specific land cover types: for the 4 sites located on crop

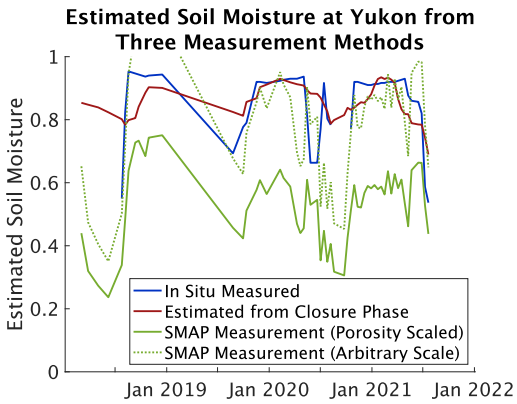

Figure 4.10: Estimated soil at Yukon site from detrended cumulative closure phase, *in situ* data from the Oklahoma Mesonet, and SMAP.

lands, the average correlation coefficient is $R = 0.29$; for the 21 sites on grasslands, $R = 0.37$; for the 10 sites on pasture, $R = 0.45$.

The relationship between vegetation and quality of fit is further demonstrated in Fig. 4.12, which shows that the NDVI vegetation index correlates with how well the closure-phase-based estimate fits the soil moisture measurements. This plot shows a weak negative correlation ($R = -0.45, p = 0.09$) between RMSE of estimated soil moisture and higher levels of vegetation according to the vegetation index, indicating that more vegetated areas have more accurate soil moisture measurements. There was no significant relationship between the average NDVI and the correlation coefficient R between measured and estimated soil moisture at each site.

4.4 Discussion

4.4.1 Spatial Scale

This proof of concept work involves a high amount of multilooking (50x20 looks) and post-processing spatial averaging, which leads to a pixel size that, while still at a fine resolution relative to passive radiometry, could nonetheless be improved if we could reduce the number of looks while maintaining good soil moisture estimation. Preliminary results show a slightly more modest correlation at many sites with 25x10 looks (average $R = 0.28$ between measured and estimated soil moisture). With less multilooking, the correlations became much weaker: with 10x4 looks, 31 days of temporal averaging of *in situ* soil moisture, and a 9x9 spatial filter, the average correlation coefficient between measured and estimated soil moisture at all sites $R = 0.18$, half of its value $R = 0.36$ with 50x20 looks.

While more research is needed to determine why some sites exhibit higher correlation between the *in situ* and SAR data at smaller spatial scales while others are more correlated at larger scales,

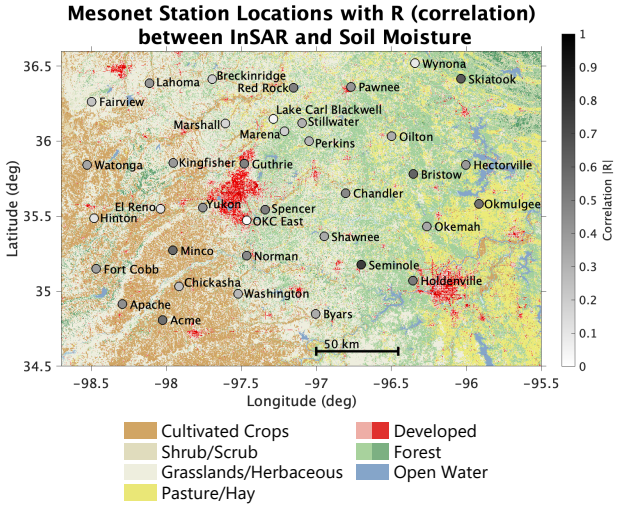

Figure 4.11: Land cover map of swath, with dots showing quality of fit as correlation coefficient $|R|$ between estimated and *in situ* soil moisture at each site. Landcover type may influence how well the InSAR data fits the soil moisture. NLCD land cover image courtesy of U.S. Geological Survey [133]. Location of the inset is shown in Fig. 4.1.

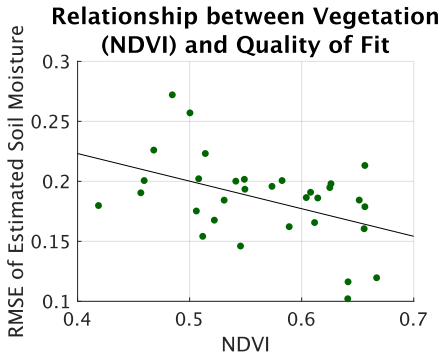

Figure 4.12: Plot of NDVI (a vegetation index that roughly represents "greenness") against the RMSE of estimated soil moisture. Generally, areas with higher vegetation index appear to have slightly lower error values. The correlation coefficient between NDVI and RMSE of estimated soil moisture is $R = 0.45$ with a p-value of 0.09. Average NDVI comes from MODIS 16-day composites via [14].

it is possible that it relates to the size of features in the area (e.g. fields, vegetation, human-made structures). Areas that are more homogeneous may perform well with more averaging to reduce the noise, while areas with more heterogeneous surface scattering properties may perform more poorly with more averaging, as the *in situ* soil moisture at one point may not be representative of the entire multilook window. The best window size may be the size of the features in the area, such as agricultural fields.

4.4.2 Closure Phase and Systematic Bias

Some studies have characterized a systematic bias in closure phase [4, 151], which leads to a trend in the cumulative closure phase. According to our model, this trend emerges from a nonlinear response to differing rates of wetting and drying. With our simple two-layer scattering model, non-zero closure phase arises specifically from the nonlinearity in the model, as shown in Section 3.2. Using our model, symmetric patterns of wetting and drying, where the soil moisture increases and decreases at the same rate (such as sinusoidal and triangle wave functions), do not produce a trend in the cumulative closure phase. Wetting typically happens quickly with rainfall, while drying is a slow decay; this asymmetry is the key to producing a trend in our modeled closure phase and may also drive the trend in the data. A better understanding of what causes the trend may allow us to leverage the information contained in the trend for improved estimates, rather than removing it.

The systematic bias has been noted to "fade" with longer temporal baseline interferograms [4]. A possible reason is that the temporal correlation of the subsurface scatterers disappears with a long temporal baseline, and the surface return dominates the signal in long-baseline interferograms. While this explanation fits within the framework of our model, it remains to be shown why the subsurface would decorrelate faster.

4.4.3 Vegetation

Non-zero closure phase can arise from interactions between the vegetation canopy and the ground instead of – or in addition to – the soil surface and subsurface. Soil moisture changes and vegetation changes are interdependent but not identical: for example, vegetation canopies retain water even after the soil dries. To accurately measure soil moisture, we would like to separate the vegetation signal from the soil moisture signal. In areas with dense vegetation, the vegetative signal may dominate the soil moisture contribution to closure phase (especially at C-band [124]); in others, the soil moisture signal may predominate. Small-scale variations in irrigation may further complicate the representativeness of an *in situ* point measurement versus a remotely sensed pixel.

Our results reinforce findings from other studies that characteristics of closure phase vary over terrain [4, 151, 11]. Some studies have found that estimation of soil moisture from closure phase performs unexpectedly well over highly vegetated or forested land [39, 79]; the lower errors we found at sites with higher NDVI and in the eastern, more-forested half of the swath corroborate this result.

Sensitivity of the closure phase measurements to changes in both vegetation and soil moisture may partially account for the lower correlation with the "true" soil moisture signal found from the extended triple collocation compared to SMAP and the *in situ* measurements. Analysis of data sets quantifying soil moisture alongside changes in vegetation, such as time series of NDVI or canopy moisture content, would help to distinguish the components of the signal.

4.4.4 Structural Limitations of Closure Phase

The scattering model used in this study is highly sensitive to small perturbations in the soil moisture time series. High sensitivity to specification of the soil moisture model is a known issue [153, 86]. A more robust scattering model would lend insight into the specific mechanisms that cause systematic closure phase.

Additionally, the measurement of soil moisture from closure phase is an underdetermined problem, where there are multiple possible soil moisture time series which may produce the same closure phase [153, 89]. For example, a triplet with the same dielectric constant at two of the three dates will produce zero closure phase, even if the third date differs [152, 40]. These structural issues may also be responsible for some of the results in areas with poorer soil moisture estimates. Other studies that include inversion of closure phase [153, 39, 89] explicitly use cost functions or boundaries to constrain this under-determined problem. The inversion presented here, which involves a cumulative sum and trend removal, makes no such mathematical constraints. Instead, it limits possible soil moisture values found from the closure phase with the assumptions that the time series is long enough to capture the range of closure phase, that it varies within that range, and that the characteristics of these variations are consistent over time. It is promising that soil moisture estimates can be found at many sites in spite of these limitations, but further analysis of their impact is an avenue for future research.

4.4.5 Other Future Work

Future work could include testing this technique in a wider range of environments subject to a diversity of ground cover, soil moisture, and surface scattering regimes.

Loss in coherence has been shown to correspond to soil moisture [118]. This work uses only the closure phase, but many other studies invert for soil moisture using coherence or amplitude and closure phase, suggesting that coherence may be a powerful complement to closure phase for characterizing soil moisture [40, 153, 67, 10].

The methods presented here generally apply at any wavelength, although what is detected at different wavelength scales is likely to be different. For example, soil moisture values can be found from deeper in the ground at L-band than at C-band, and L-band signals are less sensitive to vegetation, which may dominate the C-band closure phase signal [101, 53, 42, 55]. It is thus likely that this method would perform well at L-band, including on the NISAR mission.

Because three separate images are required, missions with a 12-day repeat such as Sentinel-1 and NISAR produce triplets over a minimum time span of 24 days. A future SAR mission with a shorter repeat cycle (for example, on the scale of 1-3 days) would produce a finer temporal resolution of closure phases.

4.5 Conclusion

We demonstrate that soil moisture can be estimated from InSAR using detrended cumulative closure phase. There is no need for *a priori* knowledge of soil moisture to create this estimate. Our model shows that an interference signal between surface and subsurface scatterers produces a closure phase in multilooked images. Much as cumulative InSAR phase describes variation in the ground surface over time, cumulative InSAR closure phase describes variation in the scattering properties of the ground over time. The detrending step prevents the cumulative closure phase from being biased by an increasing trend so that it can be matched to the soil moisture signal. The strength of this trend is related to asymmetries in wetting and drying, and is a result of the nonlinear nature of closure phase. We find an anticorrelation between the detrended cumulative closure phase and the soil moisture consistently, both using our model and sites in an Oklahoma InSAR swath. We can find an empirical fit between the *in situ* soil moisture and the detrended cumulative closure phase that can be used to estimate soil moisture from closure phase values.

The variation in quality of fit from site to site relates to vegetation and terrain characteristics. Pasture land tends to have better matches between closure phase and soil moisture, and crop land tends to be worse, while grasslands fall in between. Given the relationship between accuracy and terrain, a promising area for future work is to optimize the estimation of soil moisture across different land cover types, or to tailor the estimation to regions of interest based on their vegetation and land composition.

The cumulatively-summed closure phase could prove to be a powerful parameter to measure scatterers on the ground using InSAR. The high resolution of InSAR data could enable soil moisture retrieval at a scale important for agricultural, ecological, and flood and drought management applications.

Chapter 5

Measuring Changes in Vegetation Moisture from InSAR Closure Phase Time Series

Note: This chapter is lightly adapted from a conference paper coauthored with Roger Michelides and Howard Zebker [135] as well as validation data collected by the SMAPVEX team including Andreas Colliander, Michael Cosh, Natan Holtzman, Simon Kraatz, Vicky Kelly, and Alex Konings [58, 33].

5.1 Introduction

Remotely measuring changes in vegetation moisture is important for agricultural and environmental applications. While radiometry is sensitive to moisture, the resolution is low; optical and infrared measurements can be very fine-resolution but cannot directly measure moisture, instead relying on proxies such as brightness at wavelengths sensitive to chlorophyll. Because InSAR is sensitive to water, it is an attractive possibility for a more direct measurement of the water content contained in vegetation. Scattering from an upper vegetation canopy as well as from lower layers of vegetation or from the ground can result in radar phases similar to that produced by two layers of soil, so that changing moisture in a vegetation canopy can produce a non-zero closure phase. Some work has already considered the effects of InSAR closure phase on vegetation [39]; this chapter also draws from prior publication [135].

In this chapter, we will show that InSAR closure phase tracks several metrics of vegetation moisture from in situ measurements. We show data from two validation sites in the Harvard forest in central Massachusetts, discussing the relative impacts of vegetation moisture and soil moisture on InSAR closure phase. At the first site, cumulative InSAR closure phase at C-band, while not

correlated with soil moisture or L-band vegetation optical depth, is anticorrelated with the canopy wetness and well-correlated with the xylem dielectric constant. This suggests that the closure phase is modulated by changes in water content in the canopy. At the second site, there is a stronger relationship between soil moisture and InSAR closure phase, and the relationship between closure phase and vegetation is moderate but drops to zero when controlling for soil moisture; this suggests that the closure phase at this site is modulated by soil moisture.

5.2 Methods

5.2.1 Sensing Vegetation Moisture

While in situ sensors of soil moisture for validation are abundant, sensors of vegetation moisture are much less common. Validation campaigns for the Soil Moisture Active/Passive satellite (SMAP), called the SMAP Validation Experiment (SMAPVEX), provide some of the most consistent data for changing moisture content in a canopy and co-located soil moisture over time. While these measurements are optimized for comparison with the SMAP satellite, they are also useful for comparison to active radar data, such as the Sentinel-1 satellite.

The first data set used in this analysis, the SMAPVEX19-21 Vegetation Optical Depth data set [7] [58], provides a time series of measurements of vegetation optical depth (VOD), tree xylem dielectric constant, canopy wetness, and surface soil moisture over a period from April through October of 2019. This measurement coincides with 11 Sentinel-1 overpasses of the area. The VOD measurements come from an L-band tower; the tree xylem (stem) dielectric measurements from a probe in the tree; soil moisture from a probe in the ground; and canopy wetness from leaf wetness sensors placed on leaves. The study area is a temperate deciduous forest dominated by red oak in the Harvard Forest in central Massachusetts; the average summer temperature during the months of data collection was 17.9° C, and the annual precipitation in the region averages about 100 cm with no strong seasonality [59].

The second site used is from the SMAPVEX22 validation campaign, which measured soil moisture, real and imaginary parts of soil dielectric, and vegetation dielectric in a set of sites around the Harvard Forest, Massachusetts and Millbrook, New York [33]. The second site in this study comes from the Harvard data (Site K) and is seventeen kilometers south of the site from the first study. Figure 5.1 shows a satellite view of the two sites within Massachusetts, as well as zoomed-in images of each site.

5.2.2 InSAR Closure Phase

Following Chapter 4, a time series of InSAR closure phase triplets is computed from the Sentinel-1 data taken over the acquisition times of in situ data at each validation site. The Sentinel-1 data

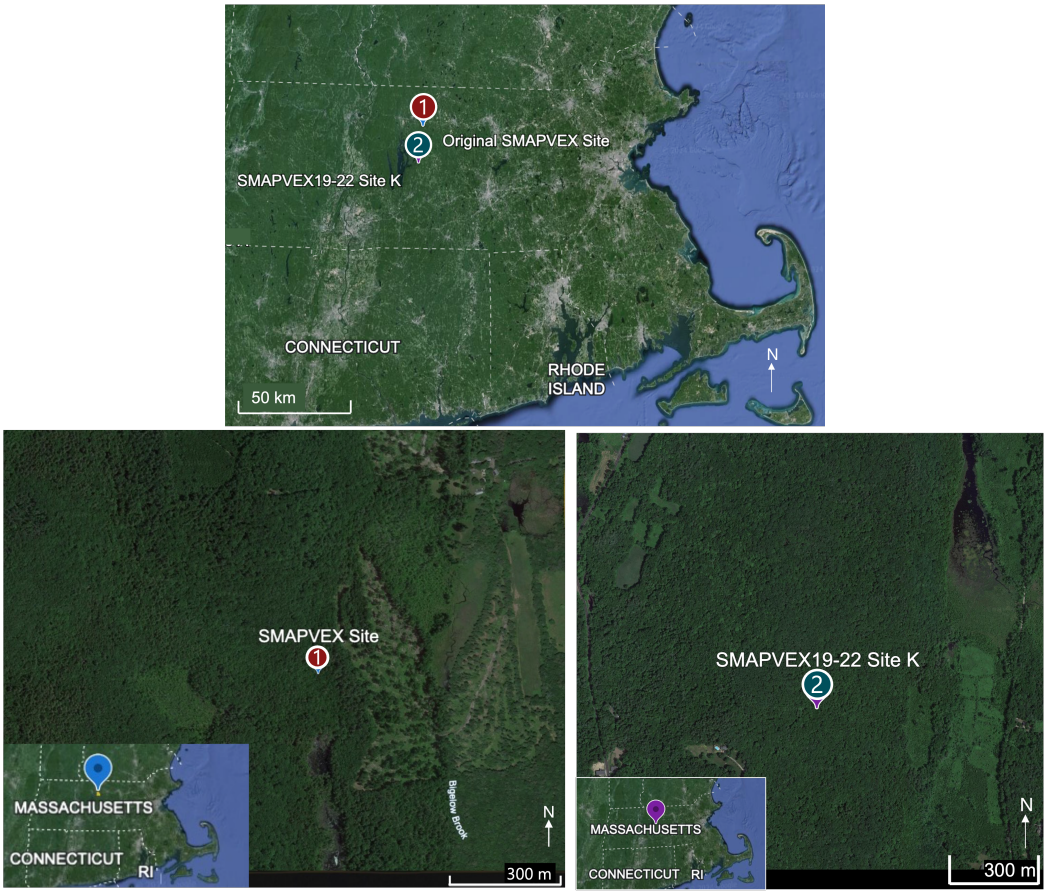

Figure 5.1: Map of area surrounding SMAPVEX observation site. Image from Google Earth, includes data from: Airbus, Google, Landsat/Copernicus, Data SIO, NOAA, U.S. Navy, NGA, GEBCO, June 2022.

comes from Path 135, frame 136 over all dates overlapping each SMAPVEX campaign. For the first site, the Sentinel-1 data comes from April 27, 2019–October 24, 2019. For the second site, the Sentinel-1 data includes all acquisitions from June 2, 2019–June 22, 2022. The triplets are computed only from sequential (nearest-neighbor in time) and second-nearest neighbor interferograms, so all temporal baselines are as short as possible. The closure phase time series is then cumulatively summed and compared to the moisture values. While, for soil moisture, we could detrend the closure phase over three years to compare to the soil moisture signal, the time period of the in situ vegetation measurements at the first site is too short to represent a full range of possible values, so we omit the detrend step from this process (the detrend is omitted from both sites for consistency). As predicted in the model, we find that a time-varying dielectric constant on the ground is associated with a closure phase.

The cumulative closure phase is compared to the SMAPVEX measurement quantities at the times closest to the Sentinel-1 acquisition times; mostly, these are within half an hour of each other. The SMAPVEX measurements for the three dates contained in the closure phase triplet are averaged for comparison to each triplet. The coherence of the interferograms over the Harvard Forest area are low, with an average coherence in the area surrounding the site of 0.07. Nonetheless, with multilooking (50 by 20 looks, with an additional spatial filter on the closure phase following Chapter 4), we can find statistically significant results.

5.3 Results and Discussion

5.3.1 Site 1: Vegetation Moisture Signal Dominant

Figure 5.2 shows the time series of cumulative closure phase, compared to the soil moisture, xylem dielectric constant, canopy wetness, and VOD. There is a statistically significant positive correlation between closure phase and the xylem dielectric constant with a p-value of 0.001. Moreover, the cumulative closure phase appears to track the xylem dielectric time series fairly closely. There is a statistically significant negative correlation between closure phase and canopy wetness with a p-value of 0.003. The relationship between cumulative closure phase and soil moisture is not significant. This suggests that the C-band closure phase data is mostly sensitive to the canopy and may not reach the ground. The vegetation moisture signal is dominant at this validation site.

5.3.2 Site 2: Soil Moisture Signal Dominant

The site from the second SMAPVEX validation campaign has data across several years between 2019-2022. The four variables collected in the campaign are slightly different: soil moisture, real and imaginary parts of soil dielectric, and real part of vegetation dielectric.

At this site, all in situ variables have statistically significant positive correlations with cumulative

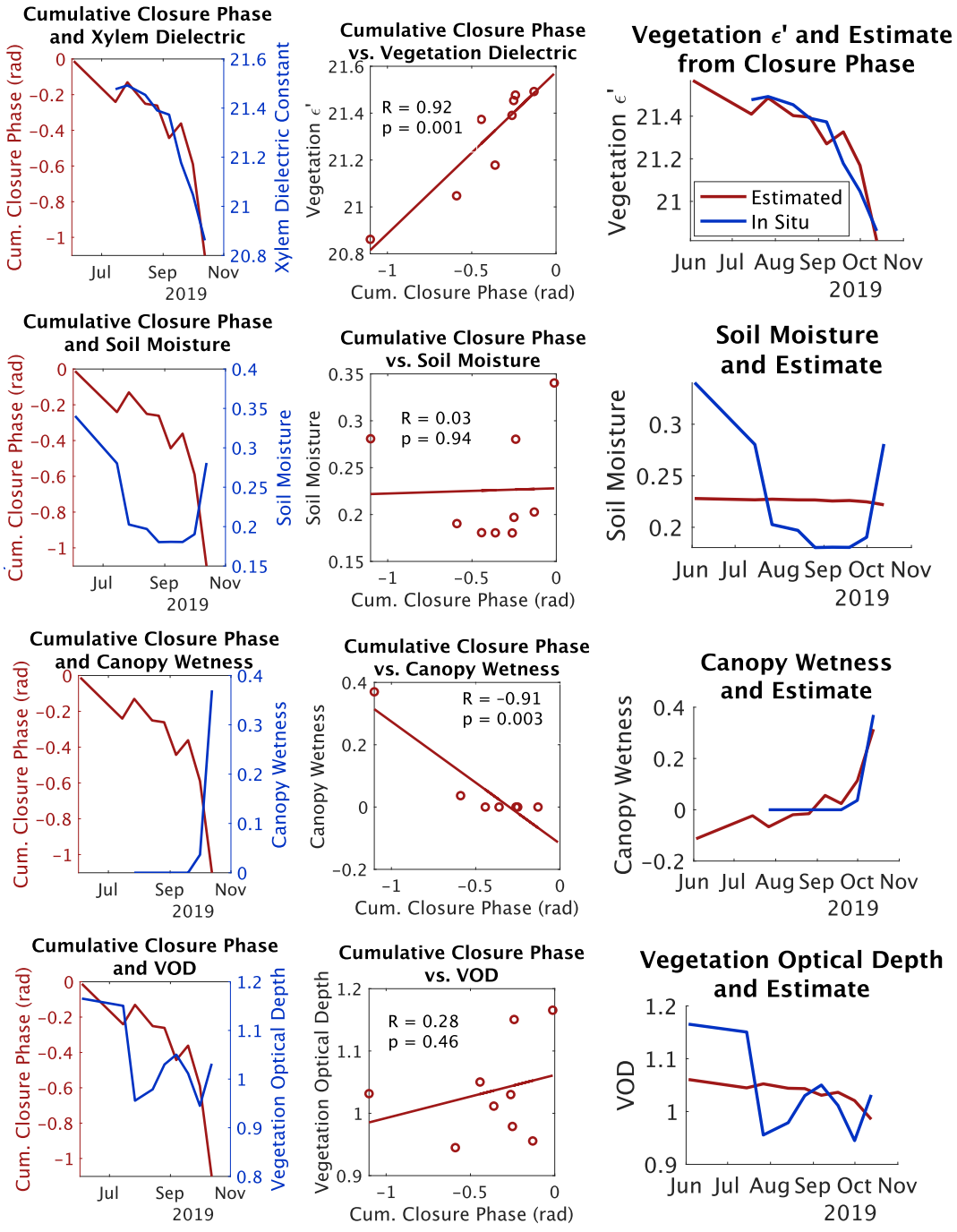

Figure 5.2: Plot of cumulative closure phase compared to soil moisture, xylem dielectric, canopy wetness, and VOD. First column: Left axis (red) shows cumulative closure phase; right shows in situ variable. Second column: Scatter plot between cumulative closure phase and each in situ variable. Third column: Estimates for each in situ variable from cumulative closure phase.

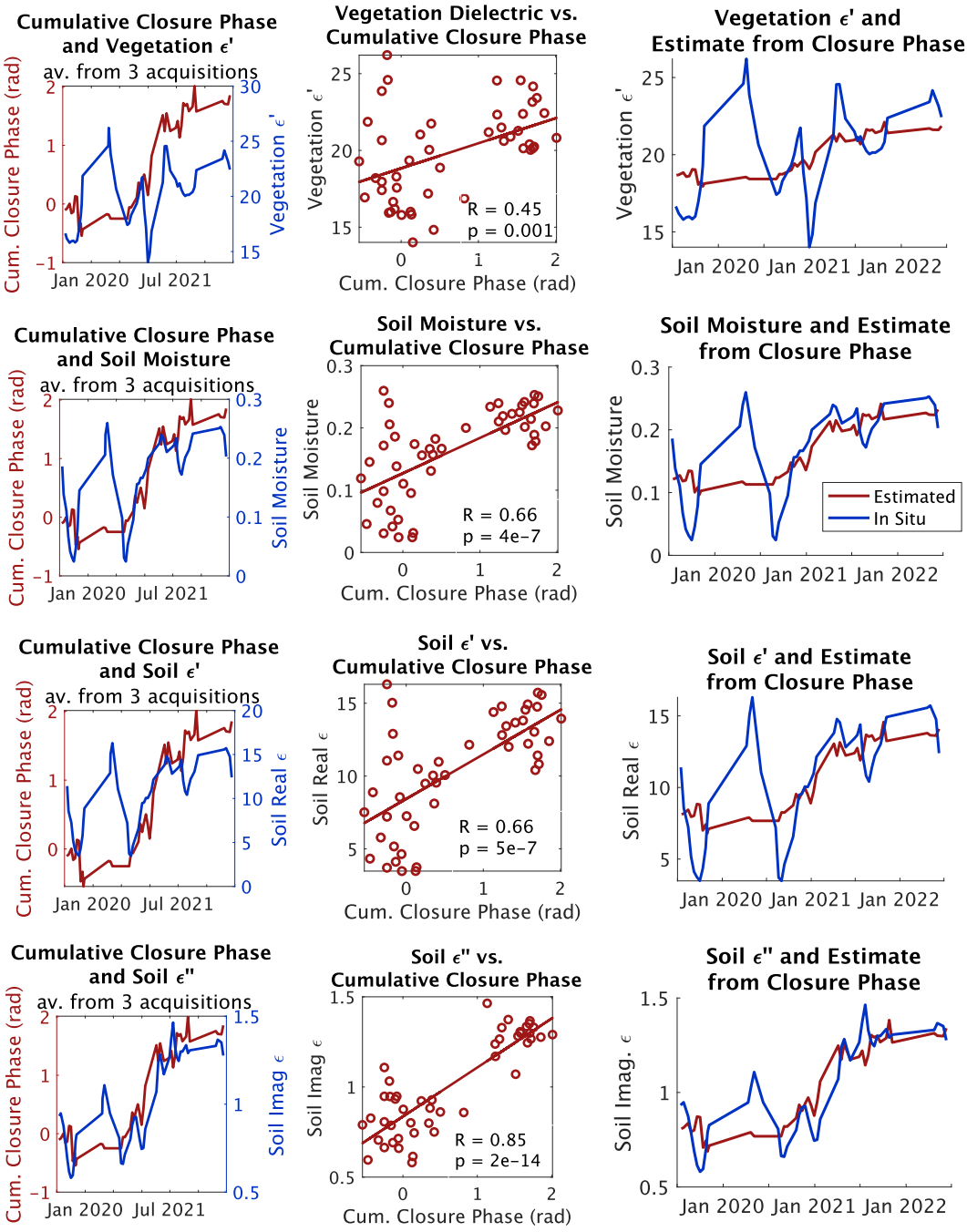

Figure 5.3: Plot of cumulative closure phase compared to soil moisture, soil real and imaginary dielectric constant, and vegetation real dielectric constant. First column: Left axis (red) shows cumulative closure phase; right shows in situ variable. Second column: Scatter plot between cumulative closure phase and each in situ variable. Third column: Estimates for each in situ variable from cumulative closure phase.

closure phase. The highest correlation is between cumulative closure phase and the imaginary part of soil moisture, with $R = 0.85$; visually, too, the closure phase estimate closely tracks the true ϵ''. The weakest correlation is with vegetation dielectric with $R = 0.45$, and the estimate from the closure phase follows the trend of vegetation dielectric but does not capture the extreme values.

Discerning which of these variables produced the closure phase is challenging, especially because soil and vegetation moisture are often correlated: in this case, the correlation coefficient between soil moisture and vegetation real dielectric is 0.70. We can start to build an understanding by considering partial correlations, finding the correlation between two variables while controlling for a third variable. The partial correlation between cumulative closure phase and vegetation, controlling for soil moisture, is not statistically significant. The partial correlation between cumulative closure phase and soil moisture, controlling for vegetation, is statistically significant with a correlation coefficient of 0.53. This suggests that the soil moisture may be "controlling" the closure phase signal, moreso than independent vegetation signals are. There are several possible explanations for this controlled correlation: it may be that the radar sees through the canopy to the ground, so the soil signals dominate the radar image. It may also be that the radar mainly sees the canopy, but the canopy signals are directly controlled by the soil (for example, as vegetation uptakes water from the ground). Whatever the cause, this site may be considered a soil-dominated site: signals from the soil can be considered the primary driver of closure phase.

5.4 Discussion

In this analysis of the relationship of closure phase to vegetation and soil moisture together, one site has a closure phase signal driven by soil moisture, while in another, the signal is driven by vegetation. This means closure phase could be used as a tool to measure either. It is therefore of interest to know which phenomenon the closure phase is more sensitive to at a given site. The differences between the first and second site in this study are not great. Both lie within the same forest, 17 kilometers apart. The first (vegetation-dominant) site is classified in the National Land Cover Database as containing evergreen, mixed, and deciduous forest within the multilook window, while the second (soil-dominant) site contains primarily deciduous forest [125]. Further analysis could elucidate which locations are soil- versus vegetation-dominant, enabling fine-resolution measurement of moisture across geographic areas.

Signals from vegetation that interfere with soil signals could also be responsible for the variable accuracy of soil moisture estimation at the test sites in Oklahoma in Chapter 4. It may be that the more well-estimated sites, such as those over pasture land, are more soil-dominated, while those with worse estimates, such as over crop land, are more vegetation-dominated.

The sensitivity of the radar phase to soil and vegetation also depends on the wavelength; Eq. 2.19 shows that longer wavelengths have a slower-changing phase. In practice, longer wavelengths

penetrate more deeply into soil and vegetation media. This may mean, for example, that at a particular site, C-band data from the Sentinel-1 satellite captures more signals from the canopy, while L-band data from the NISAR satellite penetrates further through the canopy and into the soil. Multi-frequency analysis is another promising future path for simultaneous measurement of soil and vegetation moisture.

The next chapter will examine a location where neither soil nor vegetation dominates the closure phase signal, which is measured at L-band from an airborne platform.

5.5 Conclusions

Closure phase is sensitive to vegetation and soil moisture in varying proportions, with some sites showing a stronger relationship to vegetation moisture, while others show a stronger relationship to soil moisture. Closure phase could therefore be an important tool in the mapping of either type of moisture. Remote measurement of changing vegetation moisture can be used to inform agricultural irrigation decisions, validate evapotranspiration models, or to understand environmental processes. Moreover, if we can pinpoint where and how changes in soil moisture and vegetation produce a closure phase, we can improve our technical ability to remove nuisance closure phase signals from interferograms when deformation measurements are desired [153].

Chapter 6

Gridded Wildfire Fuel Moisture from InSAR Closure Phase

Note: This chapter is lightly adapted from a conference paper coauthored with Yunling Lou, Richard Chen, Karen An, Howard Zebker, and Roger Michaelides [Todo: Cite IGARSS paper - should be available at IEEEXplore soon]

6.1 Introduction

With climate change, extreme wildfires are growing in frequency and intensity [36]. Greater fire risk occurs in areas that have a lot of fuel that is very dry; knowing the water content of fuels is thus important for managing risk throughout the fire cycle (pre-fire, active, and post-fire). Fuel moisture is a measurement of water stored in live and dead plant materials; it is typically measured as a percentage of the oven-dry weight of fuel particles [108]. Current measurements of fuel moisture are sparse and labor-intensive, often requiring visits to field sites to take physical cuttings of vegetation and dry them in an oven to measure their moisture content. Therefore, a gridded, remotely-sensed fuel moisture product would be valuable for providing fuel moisture information over a wider area. Fuel moisture information can be used to improve numerical fire modeling inputs, allocate resources for active and potential burns, and also inform prescribed burn activities. All of these components would help decision-makers evaluate and manage fire risk and reduce impacts over large geographic areas.

We have shown that InSAR closure phase is sensitive to changing volume scattering from moisture in vegetation, meaning it provides a good candidate measurement for estimating fuel moisture [39, 41, 134, 135, 152]. Following the layered scattering model from Chapter 3, we can consider vegetation canopy and soil as dielectric layers that interact with radar waves and produce closure phases. In

Figure 6.1: Photo of chapparal landscape around Mt. Diablo (Elizabeth Wig, 2020)

this chapter, we will show that a cumulative sum over a time series of InSAR closure phases at L-band can be used in conjunction with in-situ soil moisture to find vegetative live fuel moisture at a site in Mt. Diablo, California.

6.2 Methods

We use InSAR data from NASA's UAVSAR (uninhabited aerial vehicle synthetic aperture radar) instrument to derive a time series of closure phases, spanning 2009-2022. The InSAR closure phase processing is performed following Chapter 4 and [134]. A time series of sequential and skip-one interferograms, multilooked to a 50 m pixel size, is used to derive a closure phase time series of sequential triplets. The triplets are then cumulatively summed to compare to the moisture variables. Like in our vegetation study from Chapter 5, we do not detrend the cumulative closure phase, because we do not have frequent enough measurements to capture a significant trend over time. We look at two swaths with opposite flight headings (Hayward 05501 and Hayward 23501), with 23 acquisitions in each, over the Mt. Diablo area, a chapparal ecosystem in northern California.

The Clayton Ranch site in this area has both in-situ measurements of soil moisture acquired by NOAA [5] and of fuel moisture from the Fuel Moisture Repository Webportal [137]. Fuel moisture is measured in chamise plants and categorized into "old growth" and "new growth." Comparing the two types of growth, the measurement time series are similar, so we report the results from the old-growth plants here. The fuel moisture measurements are taken approximately every 2 weeks in the

spring, summer, and fall, and more infrequently in the winter; they are measured as a percentage. The soil moisture is measured at 10 cm and 20 cm depth every 2 minutes, and measurements started in 2014; we use the 10 cm depth measurements as we believe this is more representative of the penetration depth of the UAVSAR L-band instrument.

To compare these three types of measurement, some consideration of representativeness is needed: The in-situ soil and fuel moisture measurements are taken about 1.9 km away from one another, and the UAVSAR swath covers both. The UAVSAR native pixel size is 1.6x1 m, and we multilook to 50 m pixels. A greater challenge is temporal representativeness; time gaps between the UAVSAR and the fuel moisture measurements vary from 6 hours to over 1000 hours over the period of study. To ensure at least moderate representativeness, we filter out any measurements whose time gap is greater than 100 hours. Fortunately, the soil moisture had consistent measurements with short time gaps to both the fuel and InSAR measurements, although the soil moisture measurements started five years later, in 2014. We temporally average the fuel moisture and soil moisture measurements across the three acquisition dates in the InSAR triplet. To estimate fuel moisture, we find the nearest measurements in time of InSAR cumulative closure phase (measured to the center acquisition in the triplet) and of the fuel moisture and soil moisture. We perform a multiple linear regression of the soil moisture and closure phase at the Clayton Ranch site to estimate the fuel moisture. We evaluate the quality of the fit with correlation coefficients and percent error. The linear regression takes the form

$$m_{fuel} = Am_{soil} + B\phi_{cl} + C \tag{6.1}$$

for fuel moisture m_{fuel}, soil moisture m_{soil}, cumulative closure phase ϕ_{cl}, and empirically derived constants A, B, C. To test the quality of this linear regression, we evaluate the linear regression generated by one UAVSAR swath (Hayward 23501) as applied to closure phase data from a different UAVSAR swath (Hayward 05501) over the same moisture validation area. We choose to use correlation coefficients and linear regressions in this study because they can show us whether linear relationships are present among the variables of interest.

6.3 Results

6.3.1 Is closure phase produced by fuel and soil moisture?

Figure 6.2 shows the total cumulative closure phase in the Hayward 23501 swath from 2009-2022. Areas with more moisture change over the acquisition period would tend to have a larger cumulative closure phase, and locations with asymmetric patterns of moisture increase and decrease can result in particularly large cumulative closure phases over time according to our model. The brightest blue areas in this image are in the mountains and in islands in the Sacramento Delta, both places that may have had more changes in scattering due to moisture changes during the acquisition period.

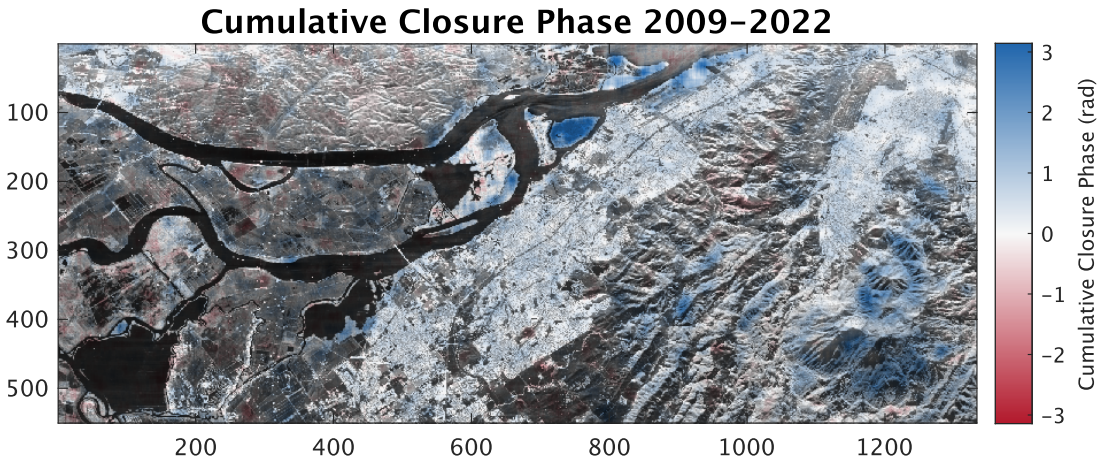

Figure 6.2: Cumulative closure phase over Mt. Diablo's Clayton Ranch validation site from Hayward_23501 swath.

Figure 6.3 (top) shows the time series of fuel and soil moisture at the Clayton Ranch validation site in this swath, alongside closure phase. At this site, the soil moisture at 10 cm depth and cumulative closure phase are anticorrelated with correlation coefficient -0.59, the correlation coefficient between old-growth fuel moisture and cumulative closure phase is -0.58, and the correlation between fuel moisture and soil moisture is 0.92. (Old and new-growth fuel moisture have correlation coefficient $R = 0.82$ and produce similar results in our investigation). While soil and fuel moisture are highly correlated, cumulative closure phase does not have a high enough correlation with either variable individually to produce very accurate estimates.

We also find that the partial correlation between cumulative closure phase and vegetation moisture, controlling for soil moisture, is $R = -0.84$. While both soil and fuel moisture are similarly correlated with closure phase in this region, closure phase is also sensitive to some of the ways in which they differ: this is why the correlation increases when controlling for soil moisture. As a result, while an estimate for fuel moisture from soil moisture would be fairly accurate, we can incorporate closure phase to make an even more accurate estimate.

As proof that closure phase arises from a combination of fuel and soil moisture, we test whether a linear combination of the two moisture types is sufficient to reproduce closure phase. Figure 6.3 (bottom) shows the result of this fit, with a correlation coefficient $R = 0.90$. This result suggests that the closure phase signal is dominated by a combination of fuel moisture and soil moisture signals, and that these signals together can generate an estimate for the closure phase.

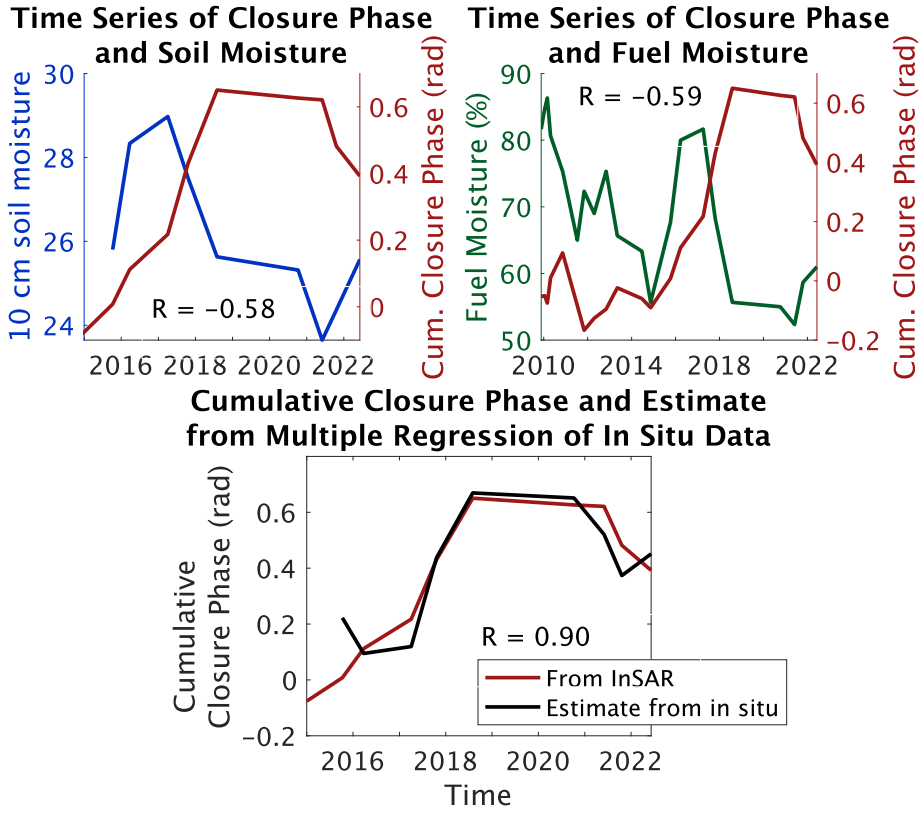

Figure 6.3: Top: Time series of soil moisture, fuel moisture, and closure phase in Hayward 23501 swath; correlations are present but neither moisture type can entirely reproduce closure phase. Bottom: Estimate of InSAR closure phase from linear combination of fuel moisture and soil moisture.

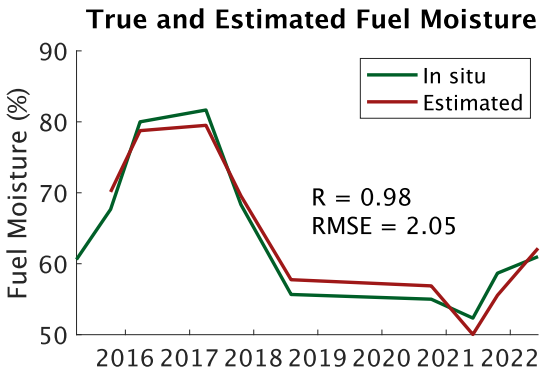

Figure 6.4: Estimate of fuel moisture at Hayward 23501 swath based on InSAR closure phase and in-situ soil moisture.

6.3.2 Can we invert for fuel moisture, using closure phase and soil moisture?

While it is reassuring to see that a combination of fuel and soil moisture can produce closure phase, the measurements that are generally most difficult to find are fuel moisture, as measuring fuel moisture involves labor-intensive cutting and drying of samples. Therefore, we would like to see whether we can measure fuel moisture without this labor-intensive process, using a combination of remotely sensed closure phase and in situ soil moisture. Figure 6.4 shows the result of a linear combination of closure phase and soil moisture to estimate fuel moisture. At this site, the derived regression for fuel moisture is:

$$m_{fuel} = 4.1 m_{soil} - 18.1 \phi_{cl} - 37.1 \tag{6.2}$$

Figure 6.5 shows the time series of the closure phase in the second swath compared with soil moisture and fuel moisture, and it shows the result of applying the inversion equation (6.2) from the first swath to the data from the second. In this case, the correlation coefficient between estimated and true fuel moisture is 0.96, and the RMS error is 5.0%. This is comparable to deriving a new regression equation from this swath (6.3), which has a correlation coefficient between estimated and in situ fuel moisture of 0.96 and an RMSE of 2.7. The regression equation derived from the second swath is:

$$m_{fuel} = 4.8 m_{soil} - 25.5 \phi_{cl} - 57.3 \tag{6.3}$$

These results show that the relationship between soil moisture, fuel moisture, and InSAR closure phase can generalize at least at the same location, and the relationship from an InSAR pass in one direction can accurately predict the relationship from a pass at a different time, with an opposite

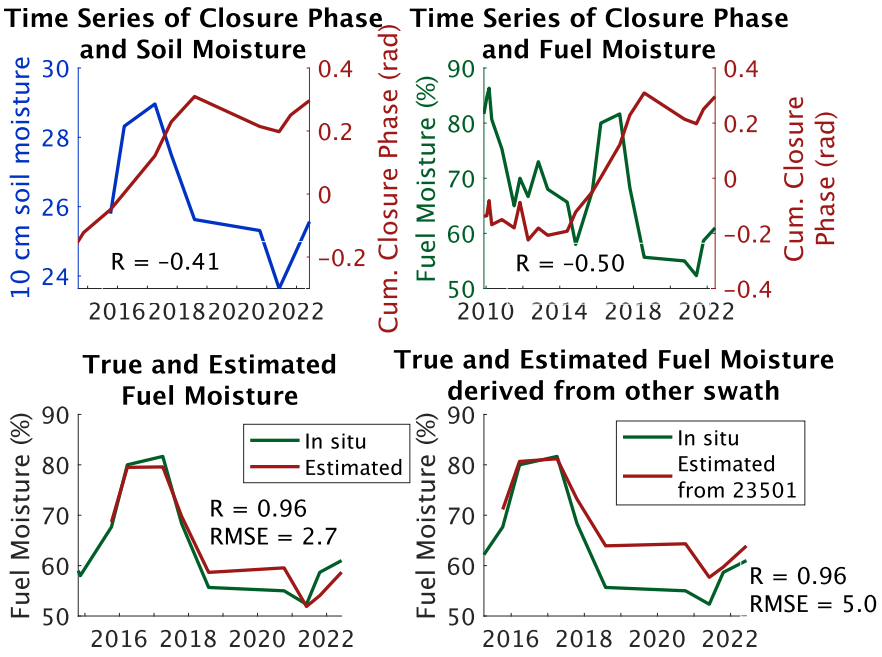

Figure 6.5: Top: time series of soil moisture, fuel moisture, and closure phase in Hayward 05501 swath. Bottom: estimate of fuel moisture based on InSAR closure phase and in-situ soil moisture from equations derived at this site (left, equation 6.3) and derived from relationship in Hayward 23501 swath (right, equation 6.2).

flight heading and viewing geometry. More data would help to define and understand the limitations of this relationship, enabling estimation across an InSAR swath.

6.4 Discussion

In studying the potential of using InSAR closure phase for fuel moisture, several limitations and opportunities became apparent. One limitation is the lack of simultaneous, co-located validation data of soil and vegetation moisture. Understanding the likely contributors to closure phase involves an understanding of both, but validation measurements of both over long time series are limited. The Clayton Ranch site, with measurements of the two nearly 2 km apart, was the closest fuel and soil moisture with available UAVSAR overpass that could be found after an extensive search for data. Moreover, other SAR applications where separation of vegetation and soil is desirable, such as amplitude-based approaches, would also benefit from co-located validation data of fuel and soil moisture.

This leads to one of the greatest challenges of this approach: separating signals from soil and vegetation. Soil and vegetation moisture are often correlated, and changing moisture in either can result in similar radar signals. While this study used an in-situ soil moisture sensor to isolate soil moisture contributions, it is possible that future work could simultaneously remotely sense soil and vegetation by incorporating multiple polarizations, radar wavelengths, or imaging modalities. Ideally, future work would produce a remotely sensed gridded map of wildfire fuel moisture, distinct from soil moisture.

6.5 Conclusions

We have shown that we can estimate fuel moisture from a combination of remotely sensed InSAR closure phase and in-situ soil moisture. InSAR closure phase can be produced by a combination of moisture in vegetation and in soil. This method could help estimate fuel moisture over large areas at fine resolution, important for modeling, predicting, and understanding the behavior of wildfires.

Chapter 7

The Permafrost Dynamics Observatory: Remote Sensing Big Data for the Active Layer, Soil Moisture, and Greening and Browning

Note: This chapter is adapted from a paper coauthored with Kevin Schaefer, Roger Michaelides, Richard Chen, Leah Clayton, Brittany Fager, Lingcao Huang, Andy Parsekian, Howard Zebker, Yingtong Zhang, Yuhuan Zhao [136].

7.1 Introduction

Permafrost, defined as any ground that remains below 0° C for more than two years, occurs in 24% of the Northern Hemisphere [148]. Permafrost consists of rock, ice, mineral soil, and organic matter. If permafrost thaws, the organic matter will decay, releasing carbon dioxide and methane into the atmosphere and amplifying surface warming, creating a positive permafrost-carbon feedback loop that may accelerate climate change [115, 116]. The Arctic has warmed at roughly four times the global average rate [29], and monitoring permafrost is essential to understand the impact of permafrost thaw on global climate. Because a large proportion of global permafrost is concentrated in remote areas, it is difficult to collect data over large geographic regions using ground surveys. Remote sensing enables us to study permafrost at high resolution and over large areas.

The World Meteorological Organization identified several essential climate variables to measure permafrost: permafrost temperature and active layer thickness (ALT) [17, 147]. The active layer is the surface soil in permafrost regions that thaws in the summer and refreezes in the winter. The ALT is the maximum depth of thaw at the end of the summer and generally varies between 20 cm and several meters [98]. Water in the soil expands when it freezes, so the ground heaves up in winter when the active layer freezes and subsides in summer when the active layer thaws, resulting in a seasonal subsidence on the scale of centimeters [76, 138]. This seasonal subsidence increases with ALT [72, 26]. Both ALT and seasonal subsidence increase with warmer air temperatures.

A key knowledge gap is whether the Arctic-Boreal region is becoming wetter or drier in a warmer climate [49]. Soil moisture modulates the thermal characteristics of the soil, affecting ALT and subsidence [2, 32]. Volumetric water content (VWC) is the ratio of water volume to total soil volume and varies between 0 for dry soil and 1 for pure water. Field measurements indicate VWC averaged over the entire active layer negatively correlates with ALT, but VWC averaged over the upper 12 cm of soil positively correlates with ALT [32]. The permafrost itself is impermeable, blocking the downward flow of water through the soil and resulting in nearly saturated soils with high VWC in the active layer. Water table depth (WTD) is the depth from the surface to fully saturated soil in the active layer. Many models predict that as permafrost thaws and ALT increases, moisture will infiltrate deeper into the soil and WTD will increase, resulting in drier surface soils [2]. Where permafrost thaws, water formerly constrained to the active layer can drain to deeper soil layers or to deep aquifers, leaving behind drier soil [65]. Drier soil may restrict plant growth and may accelerate organic matter decomposition and associated carbon dioxide and methane emissions [68, 116]. The warming Arctic may be converted from a carbon sink to a carbon source because of greenhouse gas emissions from decomposing organic matter, so characterizing the mechanisms driving this change is important [116, 92].

Permafrost thaw can be triggered by warming, and extremely warm summers in particular can initialize thaw slumps and ice-wedge degradation [155, 69]. Thaw can also be triggered by fire, which can induce thermokarst formation and wetland succession [94]. Fire can alter vegetation patterns, which additionally affect the levels of evaporation and transpiration from soils and plants, altering the hydrology and ecology of burned areas [18]. The reduced transpiration and increased thermokarst formation can result in higher VWC in burned areas, while the thaw induced by fire can cause thicker active layers in burned areas, an effect that is particularly pronounced for areas that had thin ALTs pre-fire [88].

Trends in the Normalized Difference Vegetation index (NDVI) can be used to analyze relationships between permafrost and vegetation dynamics [105]. NDVI combines visible and infrared reflectance to detect chlorophyll as a proxy for vegetation level. An increase in NDVI over time signifies greening or vegetation growth, while a decrease represents browning or vegetation decline. In the warming Arctic, some areas are greening, such as continuous permafrost regions in the tundra, while

others show browning, such as discontinuous permafrost regions in the interior of Alaska [54, 95, 77]. Permafrost thaw can result in either greening or browning [128, 99, 96, 15]. Increased ALT as permafrost thaws can increase nutrient availability and promote plant growth, resulting in greening [103]. On the other hand, increased WTD and decreased VWC associated with permafrost thaw can dry the near-surface soil and increase drought stress, resulting in browning [126]. External factors can partially explain permafrost and vegetation change: fires can lead to both permafrost thaw and browning, for example [107, 88, 74]. Ponding and elevated VWC associated with permafrost thaw can drown plants, resulting in browning [62]. Disentangling these complex relationships represents a significant challenge.

Permafrost characteristics vary with land cover and vegetation type [97, 26, 38]. For example, we expect higher VWC and lower ALT in wetlands compared to scrub, shrub, hedge, or grasslands. Cropland has higher ALT and subsidence because harvesting removes vegetation that would normally insulate the permafrost [96]. Understanding relationships between crop lands and permafrost is especially important in light of climate-driven northern expansion of agriculture [131]. Likewise, disturbance from human development can increase ALT and subsidence [78, 73]. Subsidence exceeding design limits can damage infrastructure, and permafrost thaw puts a significant portion of Arctic infrastructure at risk [56]. Heavily developed areas often form a talik, a layer of unfrozen ground below the active layer and above the permafrost, or eventually result in the disappearance of permafrost entirely [78]. Areas with a talik or completely thawed permafrost should have a smaller seasonal subsidence than similar areas without a talik.

The Arctic-Boreal Vulnerability Experiment's Permafrost Dynamics Observatory contains data about permafrost subsidence, active layer thickness, soil water content, and water table depth, derived from airborne radar measurements at 66 image swaths in 2017 [27]. With nearly 58,000,000 pixels available for analysis, this data set enables new discoveries and can corroborate findings from previous studies across the Arctic-Boreal region. We analyze the distributions of these variables and use a space-for-time substitution to enable interpretation of the effects of climate trends. Higher soil volumetric water content is associated with lower active layer thickness and subsidence, suggesting that Arctic soil may become drier as the climate warms. Soil volumetric water content is bimodal, with saturated soil occurring more commonly in burned areas, while unburned areas are more commonly unsaturated. All permafrost variables show statistically significant differences from one land cover type to another; in particular, cropland has thicker active layers and developed land has lower seasonal subsidence than most other land cover types, potentially related to disturbance and permafrost thaw. While vegetation browning is not strongly associated with any of the measured permafrost variables, more greening is associated with less subsidence and active layer thickness and with higher bulk soil volumetric water content.

In this chapter, we analyze relationships involving ALT, subsidence, VWC, and WTD. A few thousand *in situ* ALT and VWC measurements and a few hundred WTD measurements form the

basis of the relationships described above. The available *in situ* measurements appear broadly scattered in space and time, making it difficult to extract statistical relationships. Exploring these relationships in depth requires more data, but making additional *in situ* measurements has proven extremely difficult in remote permafrost regions. Instead, we statistically analyze the relationships using 58 million simultaneous measurements of ALT, subsidence, VWC, and WTD from the airborne radar-based Permafrost Dynamics Observatory (PDO) data set. We test a number of hypotheses related to these variables: that higher latitudes and elevations have decreased subsidence and ALT; that different land cover types have different permafrost characteristics, and developed and agricultural land has thicker ALTs and more subsidence; that burned areas are wetter and have thicker ALTs and more subsidence than unburned areas; that soil VWC is negatively correlated with subsidence and with ALT; that vegetation browning is associated with thicker ALTs, more subsidence, and either elevated or decreased soil moisture; finally, that vegetation greening is associated with more subsidence, thicker ALTs, and higher soil moisture. We test whether these hypotheses hold at the scale of the entire data set, to better understand these trends at the Arctic scale. Evidence supports our hypotheses about the relationships of subsidence and ALT to latitude, land cover, and VWC, and of VWC to burned versus unburned areas and greening; the permafrost variables have weak relationships to browning and elevation, and ALT and subsidence are similar between burned and unburned areas; and we find relationships that counter our hypotheses when relating greening to ALT and subsidence.

7.2 Methods

7.2.1 Generating the PDO Data set

The PDO data set estimates ALT, subsidence, VWC, and WTD and associated uncertainties by combining L-band and P-band airborne radar as part of NASA's Arctic-Boreal Vulnerability Experiment (ABoVE) [85, 28]. The PDO data set consists of 66 image swaths in 51 locations across Alaska and Northwest Canada with a spatial resolution of 30 m, shown in Figure 7.1 [91]. It was generated using methods outlined in [87] and [28]. The data are derived from L-band interferometric synthetic aperture radar (InSAR) and P-band polarimetric SAR (PolSAR) data from early and late summer 2017 acquired with NASA's Uninhabited Aerial Vehicle Synthetic Aperture Radar (UAVSAR) instrument, which is processed to produce seasonal subsidence at L-band and co- and cross-polarization backscatter at P-band. These three variables are used as input to invert for ALT, seasonal subsidence, VWC to three depths, and WTD using physics-based models. Average values of the VWC are derived using a soil composition model for three depths: integrated from the surface to 12 cm (VWC_{12}), to 20 cm (VWC_{20}), and to the bottom of the active layer (VWC_{bulk}). Because the depth to the ALT varies, VWC_{bulk} is measured to varying depths; VWC_{12} and VWC_{20} are measured to a constant depth. The model defines VWC as saturation times porosity; because the

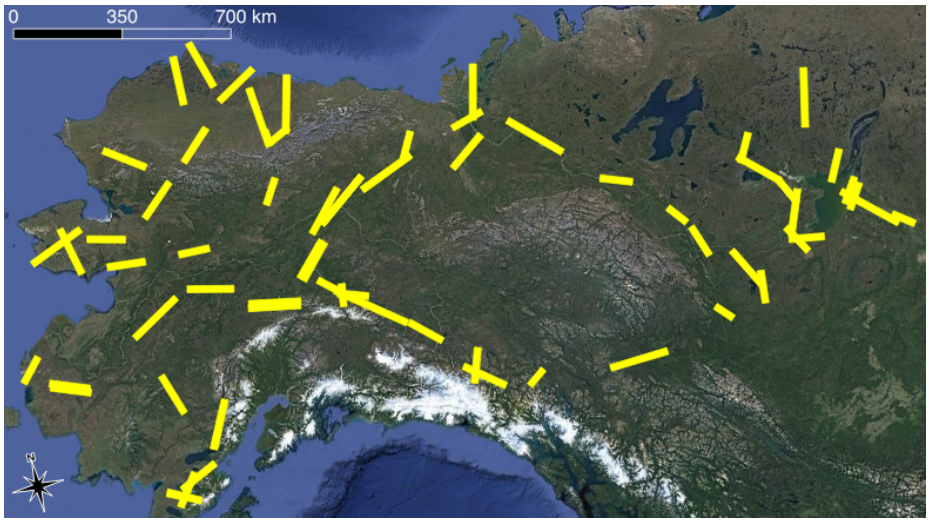

Figure 7.1: Swaths included in the Permafrost Dynamics Observatory's ABoVE: Active Layer Thickness from Airborne L- and P- band SAR, Alaska, 2017, Ver. 3 product. Background map Google Earth, includes data from Landsat / Copernicus, SIO, NOAA, U.S. Navy, NGA, GEBCOIBCAO

porosity in the soil composition model does not always extend to 1, fully saturated soil is shown in the data as approximately 0.9. Coherence data from the L-band InSAR is used for masking out pixels over water, changing vegetation, and other environments where measurements of subsidence would not be reliable. The retrieval also screened out forested pixels. The final data set contains seasonal subsidence, ALT, VWC_{12}, VWC_{20}, VWC_{bulk}, and WTD at 30 m resolution in all 66 image swaths and nearly 58 million pixels. We refer to these six variables collectively as the PDO variables. The PDO team validated the results at several sites in Alaska using in situ measurements and ground-penetrating radar [51, 23, 63, 88, 102].

The model used to generate the PDO data assumes that the permafrost table is present and well-defined because this results in any volumetric change during freezing to manifest as vertical-up heave [75]. It is possible that in some of the swaths in the PDO data set, particularly in Yellowknife, where the PDO team's field campaigns observed little to no permafrost within the first 1.5 m of the surface, there is no permafrost and only ground that seasonally freezes and thaws. The ALT may then represent the depth of winter freeze rather than the depth of summer thaw. The soil expansion model used to estimate ALT, VWC, and WTD assumes a well-defined thaw table, and it may give different results than the true soil expansion model for areas of seasonal freeze/thaw. The PDO model also assumes that, for the swaths near the coasts, waves and tidal events have minimal effects on the variables.

7.2.2 Elevation and Derived Topographic Data

We compare the PDO variables to elevation found from the ArcticDEM (digital elevation model) data set [106]. The digital elevation models encode elevation at 2 m resolution. We use the RichDEM python package to derive slope (measured in %) from the ArcticDEM data [6]. Plots comparing permafrost variables to elevation and slope can be found in the appendix.

7.2.3 Land Cover

We analyze how the PDO variables vary across different land cover types in Alaska. The land cover data is from the National Land Cover Database (NLCD) [125] and was created using Google Earth Engine composites of Landsat imagery from 2011-2016. Because the definitions of land cover types differ between Alaska and Canada, we analyze only the Alaska swaths.

Comparing the developed land cover types to all other land cover types lends some insight into how infrastructure and disturbance affects permafrost. Developed land classes are pixels dominated by human infrastructure, and the levels of development are determined by percentage of land area cover by impervious surfaces: "Developed, Open Space," where impervious surfaces account for less than 20% of total land cover, "Developed, Low Intensity," which is 20-49% impervious, and "Developed, Medium Intensity," which is 50-79% impervious. Only 4 pixels are in "Developed, High Intensity" land (80-100% impervious), so we exclude it from all measurements. Over the "Developed, Medium Intensity" land, we report subsidence from InSAR, which is accurate over buildings, but we do not analyze the other PDO variables, which rely on PolSAR measurements of soil moisture and may be inaccurate where built structures cover most of the soil. We also exclude forest, bare rock, and perennial ice/snow pixels from analysis because the PDO algorithm is not designed for those surface conditions. The land cover types we use to analyze the PDO variables are: developed, low intensity; developed, open space; cultivated crops; shrub/scrub; dwarf scrub; grassland/herbaceous; sedge/herbaceous; woody wetlands; emergent herbaceous wetlands; moss; barren (rock/sand/clay).

7.2.4 Fire

Shapefiles of fires come from the Alaska Large Fire Database and the Canadian Wildfire Information System [60, 71]. All pixels are filtered by burned and unburned, and the distributions of burned and unburned pixels compared for all PDO variables. The fire perimeters are an incomplete catalogue, especially for older fires: the archive dates back to the 1940s, but there are several data gaps especially prior to 1990. As a result, some pixels may be incorrectly categorized as unburned when they have been burned in unrecorded fires. Additionally, unburned inclusions within fire scars or other details of the fire scar polygon boundaries may be imprecise, which could result in misclassification of pixels as burned or unburned. Finally, the time since fire is another factor that would influence its effect on the permafrost variables. In this study, we perform a binary filter on fire history, but a space-for-time

swap would likely provide further insight into its effects, as in [88].

7.2.5 Greening and Browning with NDVI

In this study, NDVI trends are produced at the Landsat (30-m) scale in North America Arctic and Boreal Region [35]. We use all available Tier 1 data from 1984 to 2022 in Landsat Collection 2 (C2) hosted on Google Earth Engine. To accommodate calibration discrepancies between sensors, all surface reflectance data from Landsat 5 Thematic Mapper (TM) and Landsat 8 Operational Land Imager (OLI) are corrected to align with the Landsat 7 Enhanced Thematic Mapper Plus (ETM+) sensor [121, 113]. NDVI trends are produced from Landsat time series data which has undergone Bidirectional Reflectance Distribution Function (BRDF) correction, cloud and cloud shadow removal, and saturation elimination during the nominal peak greenness period, i.e., between day of year 181 and 240 [149]. We extend the results of [66] and produce the long-term NDVI trends by applying a simple linear regression via ordinary least squares.

We test whether NDVI trend is associated positively or negatively with the permafrost variables measured in the PDO data set. We also separately test positive NDVI trend (i.e. greening) and negative NDVI trend (i.e. browning) and compare each to all PDO variables. To perform the separate comparisons of greening and browning, we mask the NDVI trend to only include NDVI trend greater than 0 for greening, and less than 0 for browning.

7.2.6 Data Analysis

The PDO variables (subsidence, ALT, VWC_{12}, VWC_{20}, VWC_{bulk}, WTD), along with latitude, elevation, slope, and NDVI trend, have continuous distributions. When comparing two continuous variables, we use two-dimensional histograms. Using 2D histograms allows us to characterize correlations and relationships across the data set, and easily visualize information from millions of data points. A 2D normal distribution with two independent variables would look like an ellipse whose axes are aligned with the x and y axes of the plot; if the plot is shaped differently, it implies either a non-normal distribution or a relationship between the two variables. We filter the histograms to include only bins with greater than 1000 elements. We standardize the histograms to have 100 bins on each axis.

We calculate the correlation coefficient (R-value) between each pair of variables we analyze. We calculate the p-value for these correlations, but because the data set is so large ($N \approx 58,000,000$), the p-value is significant in all cases ($p < 0.05$). The R-value is therefore a more useful metric; all correlations in this large data set are *statistically* significant, but the R-value is a better metric to determine which relationships are scientifically meaningful.

Where the 2D distributions approximate a linear relationship, we regress the two variables to fit a line, which we display as a solid red line over the 2D histogram, and we calculate and plot 95% prediction intervals as dotted red lines on the histogram. Prediction intervals are a variation on the

more commonly used confidence interval [20]. A confidence interval estimates the probability that the mean value of the data falls within a fixed range; with a very large data set, the confidence interval shrinks to a width of zero. Conversely, the prediction interval estimates the probability that any individual value in a data set falls within a given range. With a large data set, we can be very *confident* that we are accurately estimating the regression; however, this does not mean that our *predictions* of a y-value from a given x-value are in such a narrow range.

When comparing our distributions to categorical variables (e.g. land cover type, fire history), we use box plots to analyze the one-dimensional distributions within each category. The box plots display the 5th, 25th, 50th (median), 75th, and 95th percentiles of the data. To determine whether differences in the mean of categorical variables are significant, we apply Tukey's Honestly Significant Difference (HSD) test [122]. This test produces, among other metrics, 95% confidence intervals for the difference between the means of two different populations, assumed to be normally distributed and equal in variance. If the 95% confidence interval does not include 0, we conclude that the difference between the populations' mean values of a given parameter is statistically significant. Plots of the results of the HSD test are shown in the appendix (Fig. A.6).

The PDO data set was collected over the course of 2017, while the NDVI data is measured from 1984 to 2022. Comparing measurements from one year to a long-term trend may result in some representation errors, especially in places where, for example, vegetation succession has taken place during the time of the NDVI trend. One study found that between 1984 and 2012, 21.2% of the land surveyed in the ABoVE region experienced land cover change [127]. Given both the large amount of spatial data available and the absence of subsidence and ALT data from earlier decades over large swaths of the Arctic-Boreal region, we aim to determine what we can from the 2017 data. In our interpretations of our results, we consider a space-for-time swap, where we use the varying spatial characteristics of permafrost as a proxy for temporal variation. This allows us to discuss what *may* happen as permafrost thaws more, based on the behavior of permafrost that is currently more-thawed.

Likewise, when comparing soil moisture to ALT and subsidence, our interpretations include some discussion reliant on a similar space-for-time swap. Here, we ask ourselves how soil moisture behaves with more-thawed permafrost – and what that implies as permafrost thaws more deeply. Lacking this type of spatially dense data over a long time period, we aim to interpret what we can from the 2017 data, and the use of spatial trends to approximate temporal information is established within this field [100, 88].

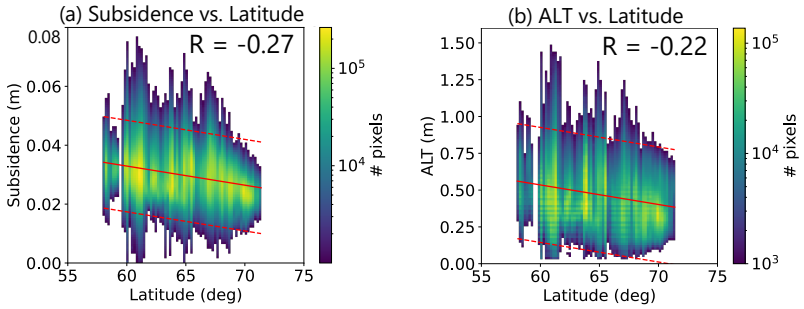

Figure 7.2: (a) 2D histogram of subsidence vs. latitude. The correlation coefficient is $R = -0.27$ and the best-fit line is characterized by $Subsidence = -6.5E-4Lat + 0.0719$. (b) 2D histogram of active layer thickness vs. latitude. The correlation coefficient is $R = -0.22$ and the best-fit line is characterized by $ALT = -0.013Lat + 1.33$.

7.3 Results and Discussion

7.3.1 Latitude

Subsidence and ALT tend to decrease with increasing latitude, as expected (See Figure 7.2). The regression lines for both relationships indicate a negative correlation. The correlation coefficients for all results are contained in Table 7.1. Subsidence and latitude have a correlation of -0.27 and ALT and latitude have a correlation of -0.22 (Fig. 7.2b). From the 2D histograms, the greatest concentration of pixels contain subsidence values between 0.02 m and 0.05 m, for ALT between 0.2 m and 0.7 m, and for latitudes ranging from 57 to 72 degrees. Because the concentration of pixels is plotted on a logarithmic scale, the densely concentrated areas of the plots (in bright green) and less-concentrated areas (in dark blue) are orders of magnitude different. The strongest correlation (-0.27) is between latitude and subsidence, with a similar level of correlation between latitude and ALT (-0.22). All correlations are statistically significant ($p < 0.05$). Correspondingly, the 95% prediction intervals shown with dotted lines are slightly narrower for the relationship between subsidence and latitude, and wider for the relationship between ALT and latitude.

Air temperature generally decreases with latitude, resulting in shallower active layers and decreasing ALT and subsidence. VWC and WTD show weaker relationships with latitude, with correlations in Table 7.1. VWC hovers near saturation for all latitudes (see appendix Fig. A.1), resulting in weak relationships between latitude and VWC and WTD.

7.3.2 Elevation

The correlations between all PDO variables and elevation and slope are very weak ($|R| < 0.1$). Although statistically significant because of the large number of pixels, these weak correlations do not provide great insight into the effects of elevation and slope. Slight negative correlations

Table 7.1: Correlation Coefficients among Permafrost Variables[a]

Variable	Subsidence	ALT	VWC_{12}	VWC_{20}	VWC_{bulk}	WTD
Subsidence	1					
Active layer thickness	**0.90**	1				
VWC_{12}	-0.08	**-0.47**	1			
VWC_{20}	-0.08	**-0.49**	**0.997**	1		
VWC_{bulk}	**-0.58**	**-0.83**	**0.76**	**0.81**	1	
Water table depth	**0.45**	**0.74**	**-0.81**	**-0.83**	**-0.79**	1
Latitude	**-0.27**	**-0.22**	-0.02	-0.02	**0.12**	**-0.13**
Elevation	0.08	0.08	-0.02	-0.02	-0.06	0.06
Slope	0.06	0.08	-0.05	-0.05	-0.07	0.06
NDVI trend	**-0.19**	**-0.15**	-0.03	-0.02	0.09	-0.08
NDVI trend masked > 0 (greening)	**-0.20**	**-0.20**	0.01	0.02	**0.11**	**-0.11**
NDVI trend masked < 0 (browning)	0.004	-0.002	0.04	0.04	0.02	-0.02
N. Slope NDVI trend > 0 (greening)	0.05	-0.08	**0.24**	**0.25**	**0.17**	**-0.21**

[a]Values are bolded where correlation coefficient $|R| > 0.1$.

between slope and the VWC variables appear consistent with increased drainage as slope increases. Subsidence, ALT, and VWC all show weak positive correlations with elevation of 0.08 or less. Since temperature generally decreases with elevation, we expected a negative relationship.

The weak correlations with elevation and slope may result from the relatively small influence these factors have on permafrost in this region compared to other factors like vegetation and latitude. Alternately, the weak correlations may simply reflect a sampling bias toward areas with minimal elevation effects. The elevation in most swaths is low because the aircraft acquisitions deliberately favored flat valleys and lowlands, which tend to have higher consequence of change [91]. Elevation and slope likely exert a much stronger influence in more mountainous terrain. Other studies have found that slope has a strong influence on thaw subsidence in Norway and the Qinghai-Tibetan plateau [112, 25]. Plots of elevation and slope compared to the PDO variables can be found in the appendix (Figs. A.2 and A.3).

7.3.3 Land cover

Figure 7.3 shows the distribution of the permafrost variables across different land cover types. The most represented land cover types are "Dwarf Scrub," "Scrub/Shrub," and "Sage/Herbaceous," with $\sim 10^7$ pixels in each land cover type. A plot showing the prevalence of each land cover type in the PDO data can be found in the appendix (Fig. A.4).

The lowest median subsidence occurs over "Developed, Medium Intensity" land, while the "Developed, Low Intensity" and "Developed, Open Space" land cover types have median subsidence in the middle of the data range. Therefore, more-developed land does indeed have lower subsidence than other land cover types. According to the Tukey HSD 95% significance metric, the mean subsidence over "Developed, Medium Intensity" land significantly differs from all land cover types except

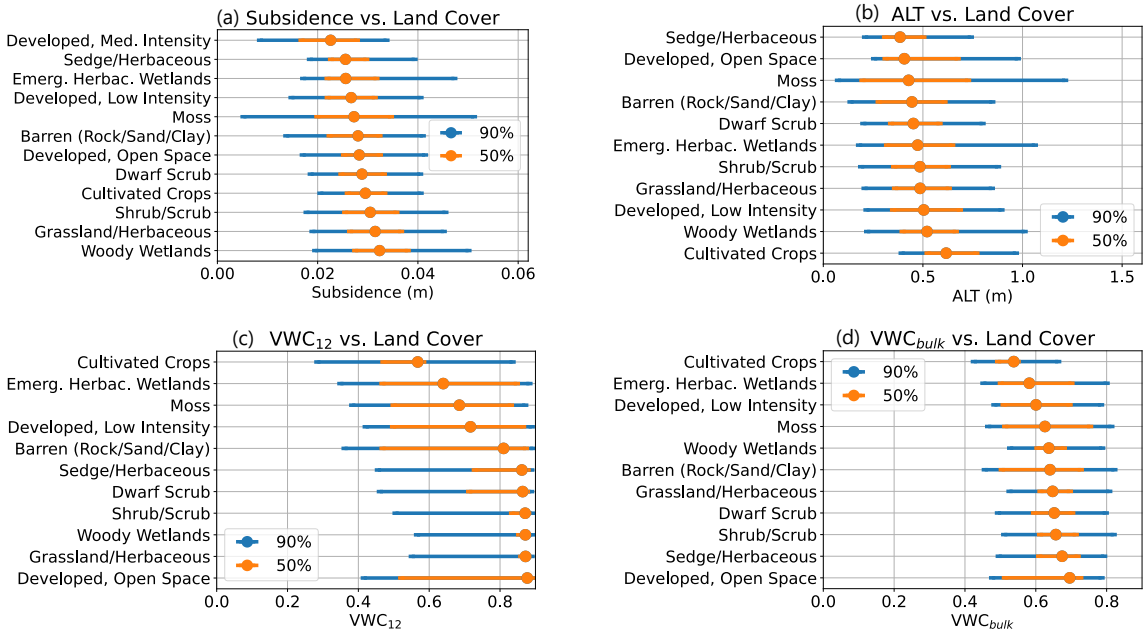

Figure 7.3: Distributions of permafrost variables, categorized by land cover type. (a) Distribution of subsidence data for each land cover type (b) Distribution of ALT data for each land cover type (c) Distribution of VWC_{12} for each land cover type (d) Distribution of VWC_{bulk} for each land cover type. Distributions of VWC_{20} closely resemble those of VWC_{12}, and are included in the appendix (Fig. A.5a), as are distributions of WTD by land cover type (Fig. A.5b).

"Developed, Open Space" and "Cultivated Crops." Plots showing the Tukey significance of each relationship are shown in the appendix (Fig. A.6). The low subsidence over "Developed Medium-Intensity" land (e.g., roads and buildings) suggests that seasonal subsidence over more-developed land is lower, because there is less permafrost and fewer taliks under those land cover types [120].

Less-developed land may respond differently to disturbance. "Developed, Open Space" land has thinner median ALTs than most other land cover types, while "Developed, Open Space" and "Developed, Low Intensity" land have middling value of median subsidence [78]. The difference in mean between the "Developed" land cover types and all naturally vegetated land cover types (i.e. vegetated land excluding crops) is statistically significant to a 95% confidence level.

The highest subsidence levels occur over "Woody Wetlands" and "Grasslands/Herbaceous." While cultivated crop land does not have the highest subsidence, it does have the thickest active layers. The difference in mean ALT between cultivated cropland and all non-developed land cover types is statistically significant. The thicker average active layers found in cropland suggests that agricultural practices may have a similar effect to the removal of insulating vegetation discussed in [96]; they may also result from phenomena that the PDO algorithm did not account for, such as ground ice content.

Unexpectedly, "Shrub/Scrub" and "Grasslands/Herbaceous" land cover types report higher VWC_{12} than "Emergent Herbaceous Wetlands." We expect near-surface soil moisture to be higher in wetlands than grasslands, so this may be a result of inaccuracies in the PDO model over wetlands, perhaps in the assumed vertical distribution of organic matter or in our scattering assumptions.

Vegetation type, broadly, has an effect on permafrost variables: the different mean values of all permafrost variables measured (subsidence, ALT, VWC_{12}, VWC_{20}, VWC_{bulk}, and WTD) were found to be statistically significant in many cases [38]. For a more specific breakdown of which cases are statistically significant, Figure A.6 in the appendix shows the results of a test of the difference in mean values of PDO variables among land cover types to 95% confidence. The big data in the PDO data set could be a valuable puzzle piece in understanding relationships between thawing permafrost and both vegetation type and infrastructure development.

7.3.4 Fire

Pixels in burned areas have, on average, higher soil volumetric water content than unburned pixels, as seen in Figure 7.4 (see also Fig. A.7), as found in other studies [70]. The VWC_{12} was on average 0.83 in burned areas and 0.79 in unburned areas; the bulk VWC was on average 0.67 in burned areas and 0.65 in unburned areas. Moreover, the bimodality observed in the histograms of soil moisture (e.g. in Figure 7.5) may be partially described by populations of burned vs. unburned pixels. Recovery seems to be on a long timescale: we found that the disparity become more apparent when we incorporated known fire scars from 1940 onwards than from 1990 onwards, although the data set is missing some fires between 1940-1990. Burned areas may be wetter because of reduced

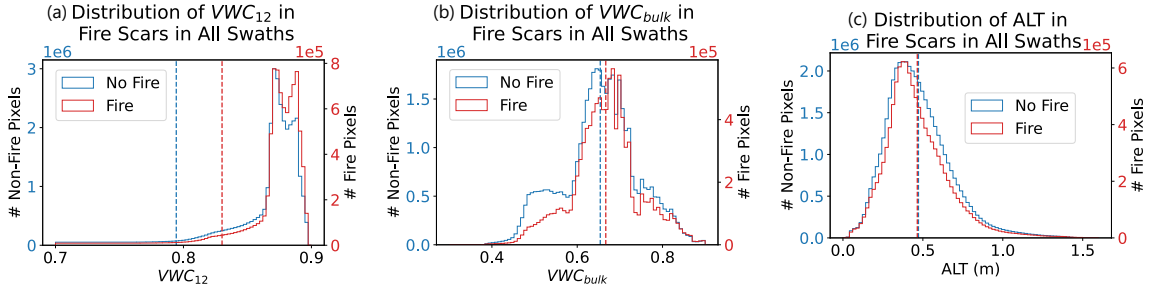

Figure 7.4: Comparison of VWC_{12}, VWC_{bulk} and ALT variables to in burned vs. unburned pixels across all sites. (a) VWC_{12} in burned (mean = 0.83) vs. unburned (mean = 0.79) areas. (b) VWC_{bulk} in burned (mean = 0.67) vs. unburned (mean = 0.65) areas. (c) Active layer thickness in burned (mean = 0.465) and unburned (mean = 0.472) pixels.

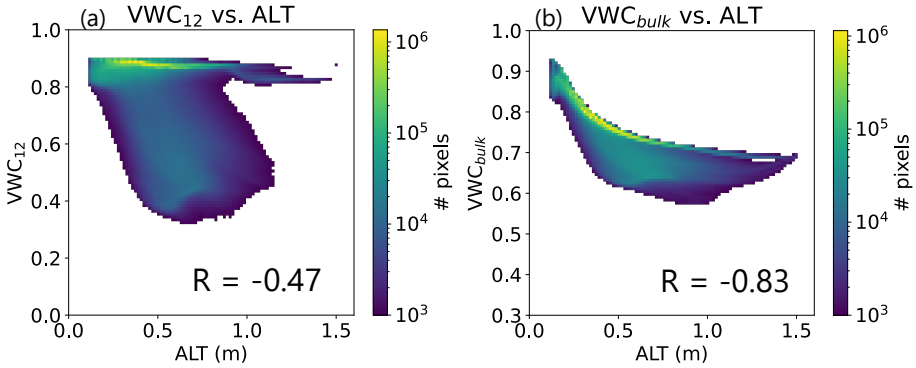

Figure 7.5: (a) 2D histogram of VWC_{12} vs. ALT (b) 2D histogram of VWC_{bulk} vs. ALT

transpiration from vegetation, or because of increased thermokarst, which tends to have higher water content [18, 64]. Burned areas may also be wetter because, after the organic layer is burned off, the water table appears closer to the surface [57, 31].

The ALT distribution for burned areas appears narrower than for unburned areas. The difference in the mean ALT between burned and unburned areas appears very slight (0.465 for burned vs. 0.472 for unburned). [70] and [88] found that burned areas have thicker active layers. This data set does not corroborate this finding on an Arctic scale, but it is consistent with [32], which found little difference in ALT between sites with and without fire history. The difference in mean subsidence between burned and unburned areas is also very slight: 0.0301 m for burned areas and 0.0298 m for unburned areas.

7.3.5 Soil Moisture

VWC decreases on average with thicker active layers, as shown in Figure 7.5. A linear regression does not adequately describe the curved shape of the distribution in the VWC_{bulk} plot. The curved shape of VWC_{bulk} results from the vertical distribution of organic matter and porosity in the soil model. The retrieval assumes a 10 cm surface organic layer with 90% porosity decreasing exponentially to pure mineral soil at 30 cm depth with 55% porosity. With nearly saturated soils, the VWC_{bulk} represents the average porosity over the entire active layer. Small ALT reflects the 90% porosity of organic soil, with corresponding high VWC_{bulk}. As ALT increases, the average porosity and VWC_{bulk} decreases, asymptotically approaching the 55% porosity of mineral soil. The correlation coefficient between ALT and VWC_{12} is -0.47, while the correlation between ALT and VWC_{bulk} is -0.83. Both correlations are statistically significant ($p < 0.05$). The appendix contains figures for all remaining comparisons of ALT, VWC, WTD, and subsidence (Fig. A.8, A.9, A.10, A.11). Subsidence anticorrelates with VWC at all depths, but the strength of this relationship varies. ALT and VWC_{bulk} show the strongest relationship with a correlation of 0.58.

The relationship between ALT and VWC_{12} appears bimodal. The vast majority of pixels lie close to saturation with a weak negative correlation. A smaller population of pixels show a strong negative correlation between ALT and VWC_{12}. The VWC_{bulk} also shows a bimodal distribution, but much smaller than VWC_{12}. Based on *in situ* measurements, we expected a positive correlation between ALT and VWC_{12} and a negative correlation with VWC_{bulk} [32]. We instead found a negative correlation between ALT and VWC at all depths. One reason we may find decreased bulk VWC with increased ALT is that, as soil thaws, the same or similar soil water content is distributed over a larger volume of soil.

These results suggest a warming climate will result in drier soil in the Arctic-Boreal region, even without any change in precipitation. Ignoring rapid thaw mechanisms such as thermokarst, ALT will increase as temperatures in permafrost regions increase. ALT and WTD show a positive correlation because as ALT increases, water drains downward from the upper soil layers, increasing the WTD [114]; the maximum possible water table depth in permafrost is the depth of the active layer. This means deeper active layers will have drier surface soils [2]. Some models find that thicker active layers also are associated with drier soils at depth [109]; our data finds drier soils at all depths with thicker active layers. The question of whether the Arctic will become wetter or drier in a warming climate often centers on precipitation, but other mechanisms affecting soil moisture may also play a role [49]. If rising temperatures result in deeper active layers, which are associated with drier soil, then Arctic soil may become drier with climate warming even in the absence of changing precipitation.

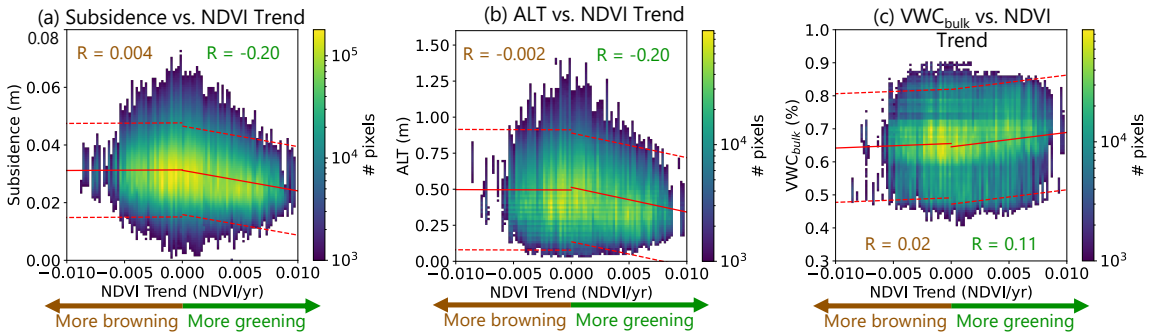

Figure 7.6: (a) 2D histogram of NDVI trend vs. subsidence, with fit lines to greening (positive) and browning (negative) sides of distribution. The correlation coefficient with browning is 0.004 and the regression equation is $Subsidence = 0.02(Trend_{NDVI}) + 0.03$. The correlation coefficient with greening is -0.20 and the regression equation is $Subsidence = -0.71(Trend_{NDVI}) + 0.03$. (b) 2D histogram of NDVI trend vs. ALT, with greening and browning fit lines. The correlation coefficient with browning is -0.002 and the regression equation is $ALT = -0.28(Trend_{NDVI}) + 0.49$. The correlation coefficient with greening is -0.20 and the regression equation is $ALT = -17.12(Trend_{NDVI}) + 0.51$. (c) 2D histogram of VWC$_{bulk}$ vs. NDVI trend, with fit line. The correlation coefficient with browning is 0.02 and the regression equation is $VWC_{bulk} = 1.37(Trend_{NDVI}) + 0.66$. The correlation coefficient with greening is 0.11 and the regression equation is $VWC_{bulk} = 4.35(Trend_{NDVI}) + 0.65$.

7.3.6 Greening and Browning: NDVI

Figure 7.6 shows 2D histograms relating NDVI trend to subsidence, ALT, and VWC$_{bulk}$. A positive NDVI trend (> 0) represents greening, while a negative trend (< 0) represents browning. Because the PDO data set was collected only in 2017, we assume that the long-term NDVI change measurement is representative of NDVI trends during 2017. Regressing the PDO variables against the greening trends represents a space for time swap. We separately regress each permafrost variable with greening and browning, and we find that the PDO variables have stronger relationships to greening than to browning: the slope of each regression is steeper on the positive side of the plot. For greening, both subsidence and ALT have a negative correlation with positive NDVI trend of -0.20, while VWC$_{bulk}$ has a positive correlation of 0.11. VWC$_{12}$, VWC$_{20}$, and WTD also have positive, but weaker correlations with positive NDVI trends; histograms comparing these variables to NDVI trend are shown in the appendix (Fig. A.12). For browning, all the parameters show near zero correlations with negative NDVI trend.

The processes that tie permafrost dynamics to greening and browning are complex and spatially varying, so it is very likely that our data includes many smaller trends that may dominate in a particular area, but not across the entire region [77, 54]. While we expected thicker ALT and more subsidence to be associated with greening [103, 128, 99, 9], the opposite relation occurs in greening regions on average. Moreover, browning is not associated with permafrost thaw or thicker active layers, as in [96, 15] – the relationship between negative NDVI trend and both subsidence and ALT

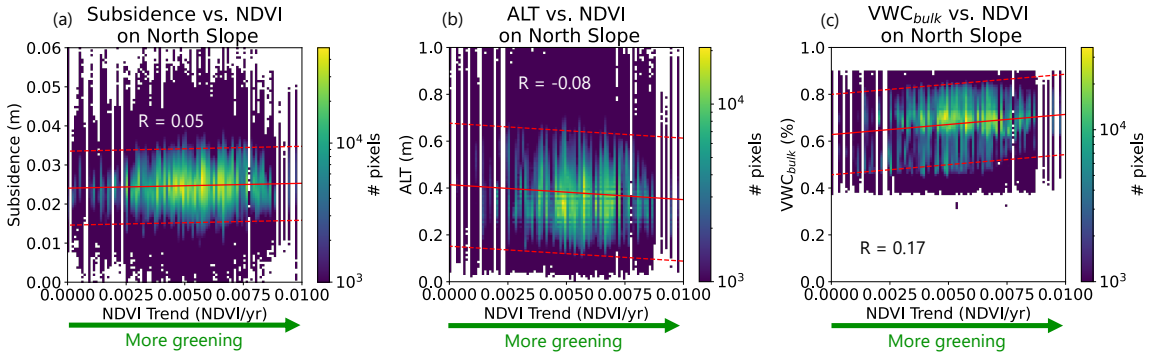

Figure 7.7: (a) 2D histogram of NDVI trend vs. subsidence on the North Slope, with fit line to greening (positive) side of distribution. The correlation coefficient is 0.05 and the regression equation is $Subsidence = 0.12(Trend_{NDVI}) + 0.02$. (b) 2D histogram of NDVI trend vs. ALT on the North Slope, with greening fit line. The correlation coefficient is -0.08 and the regression equation is $ALT = -6.71(Trend_{NDVI}) + 0.42$. (c) 2D histogram of VWC$_{bulk}$ vs. NDVI trend on the North Slope, with fit line. The correlation coefficient is 0.17 and the regression equation is $VWC_{bulk} = 8.76(Trend_{NDVI}) + 0.63$.

is very weak. One explanation could come from [99], which found that the greening associated with permafrost thaw was not sustained after prolonged periods of thaw, particularly once the thaw depth surpassed the root zone. Other complexities could result from the different types of permafrost being imaged (continuous vs. discontinuous), as in [77], or from regional differences between the interior of Alaska [126] versus the tundra [54, 96, 15]. External factors may also be important: in [129]'s study area, the limiting factors of temperature and water explained less than 50% of the variation in vegetation growth trends.

The positive correlation between VWC$_{bulk}$ and greening supports the hypothesis that greater water availability allows more greening. These findings are consistent with [103] and [9], which found that higher soil moisture was associated with greening. Our results are less definitive regarding the relationship between VWC and browning, so we were unable to validate [126], which found that browning in interior Alaska was related to lower soil moisture. We also found that [62]'s results that elevated soil water was associated with browning in a permafrost region did not hold at the scale of our data.

A 2D histogram of only the swaths in interior Alaska did not exhibit a visible trend. A 2D histogram of only the swaths in the North Slope, which is almost exclusively greening (95% of pixels greening), found that greening was positively correlated with subsidence and with VWC at all depths, and negatively correlated with ALT (Figure 7.7). We only plot greening because very few North Slope pixels are browning. Results from the North Slope region validate our expectations that subsidence is associated with greening, though this relationship is opposite to the relationship in the overall data – an example of a dominant trend in a region that does not extend to the full

data.

7.4 Conclusions

Large remote sensing data sets have potential for understanding permafrost at scale. The ABoVE Permafrost Dynamics Observatory data set enables us to test hypotheses about relationships between permafrost subsidence, active layer thickness, soil moisture, water table depth, latitude, elevation, slope, land cover, burned and unburned areas, and NDVI trend. Even a simple analysis of the statistical distributions of these variables can expand on conclusions from previous studies over smaller areas of the Arctic-Boreal region.

VWC at all depths decreases with higher ALT; a space-for-time swap suggests that a warming climate with deeper active layers may result in drier soil in the Arctic-Boreal region, even in the absence of changing precipitation. VWC is bimodal, with burned regions having on average more saturated soil, and unburned areas less saturated. Permafrost variables vary depending on land cover and vegetation type – for example, medium-intensity developed land has lower subsidence, cropland has thicker active layers, and VWC can be higher in scrub and herbaceous land cover types than in wetlands. The relationship between permafrost variables and browning is weak, but more greening is associated with lower subsidence, thinner active layers, and higher VWC_{bulk}.

We hope that other researchers can use the Permafrost Dynamics Observatory data set, or subsets of it relevant to their own research area, to answer their own research questions about permafrost.

Chapter 8

Conclusions

In this dissertation, I have shown the potential of interferometric phase to measure moisture in soil and vegetation, and discussed how this can enable newly fine-resolution measurements of moisture, enabling improved sensing for agriculture, wildfires, and permafrost. I presented a simple SAR scattering model for closure phase arising from the interference of surface and subsurface scattering in a dielectric, and used this model to show that cumulative InSAR closure phase time series can be used to estimate soil moisture. I also applied this simple model to show that asymmetric patterns of soil wetting and drying lead to long-term trends in closure phase and apparent biases in InSAR time series. Understanding this apparent bias will help reduce errors in time series measuring Earth's deformation from processes like earthquakes, volcanoes, permafrost heave, and subsidence from fluid extraction.

Following the principles of the model, we can use cumulative InSAR closure phase time series in real data to estimate soil and vegetation moisture. We can estimate soil moisture from closure phase in a variety of land cover types over a large swath in Oklahoma. We may be able to estimate soil or vegetation dielectric constant (depending on which dominates) from closure phase, as I showed in the Harvard Forest example. For cases like on Mt. Diablo, California, where we have in situ soil moisture, we can also invert for fuel moisture from a combination of InSAR closure phase and independent soil moisture measurements. All of these studies bring us closer to large-scale, fine-resolution measurement of moisture in soil and vegetation, bringing us closer to a world where we can better manage water resources and wildfires alike.

Measuring moisture is important over permafrost, where soil moisture informs permafrost dynamics, and vegetation greening and browning are indicators of changing landscapes as permafrost hydrology changes. In a case study interpreting a large-scale L- and P-band study of permafrost, I found that a warming climate with deeper permafrost active layers may lead to drier soil in the Arctic-Boreal region; that more greening of permafrost landscapes is associated with lower subsidence, thinner active layers, and higher bulk soil moisture; and that burned regions have more

water-saturated soil.

In the future, these methods could be scaled up to measure soil and vegetation moisture in a variety of environments. InSAR closure phase could be expanded to include multiple polarizations or frequencies to enhance analysis and improve discrimination among layers of canopy and soil. Closure phase-based moisture analysis could also be supplemented with SAR polarimetry and amplitude-based indices, optical data, or other remotely sensed data to deliver simultaneous measurements of water content in soil and vegetation. These supplementary data sources could also be used to discriminate where only one type of water content can successfully be detected (for example, in places with very thick vegetation or no vegetation). Further analysis could also be done with varying the temporal baselines used to calculate closure phase – these techniques are common in removing deformation, but have not yet been fully explored for measurement of moisture. Gaining a better understanding of InSAR closure phase can also enable more informed decisions on the best ways to remove moisture nuisance signals from deformation measurements. The removal of nuisance deformation signals and the analysis of moisture signals would both be helpful in complex environments like permafrost, where soil moisture modulates surface motion dynamics. Future development of the ability to independently capture soil and vegetation water content, and separate these signals from deformation, would enable large-scale analysis of changes in permafrost dynamics from active layer changes to thaw slumps to vegetation greening and browning. Future developments in measuring soil and vegetation moisture with InSAR closure phase could also enable better management of natural disasters like wildfires, landslides, droughts, and flooding.

InSAR closure phase can enable us to better measure soil and vegetation moisture, and understanding how soil and vegetation moisture fit into the larger landscape of Earth can help us unlock new insights into our planet, its ecosystems, and our own role in managing resources wisely.

Appendix A

Appendix: Additional Figures from The Permafrost Dynamics Observatory: Remote Sensing Big Data for the Active Layer, Soil Moisture, and Greening and Browning

Contents of this file

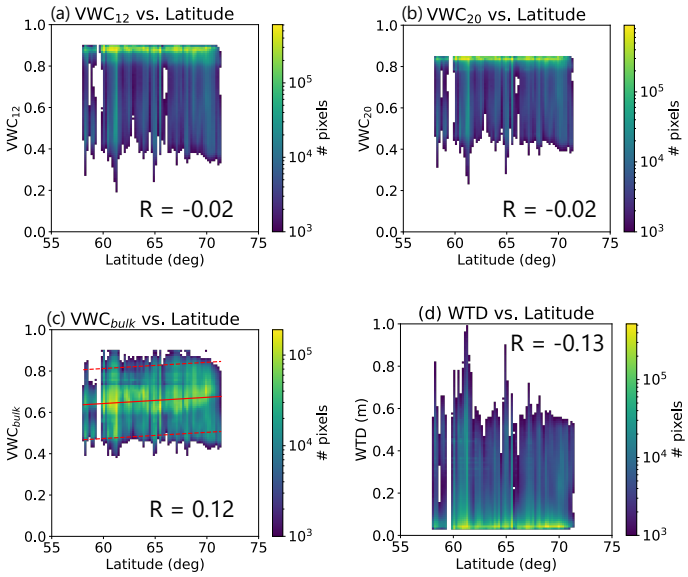

Figure A.1: Latitude compared to water-related permafrost variables at all sites. (a) VWC_{12} vs. latitude. The correlation coefficient is -0.02. (b) VWC_{20} vs. latitude. The correlation coefficient is -0.02. (c) VWC_{bulk} vs. latitude. The correlation coefficient is 0.12 and the regression equation is $VWC_{bulk} = 3.0E-3Lat+0.46$ (d) WTD vs. latitude. The correlation coefficient is -0.13.

9. Figure A9: VWC vs. Subsidence
10. Figure A10: VWC_{20} vs. ALT
11. Figure A11: Histograms of VWC and WTD
12. Figure A12: VWC vs. NDVI Trend

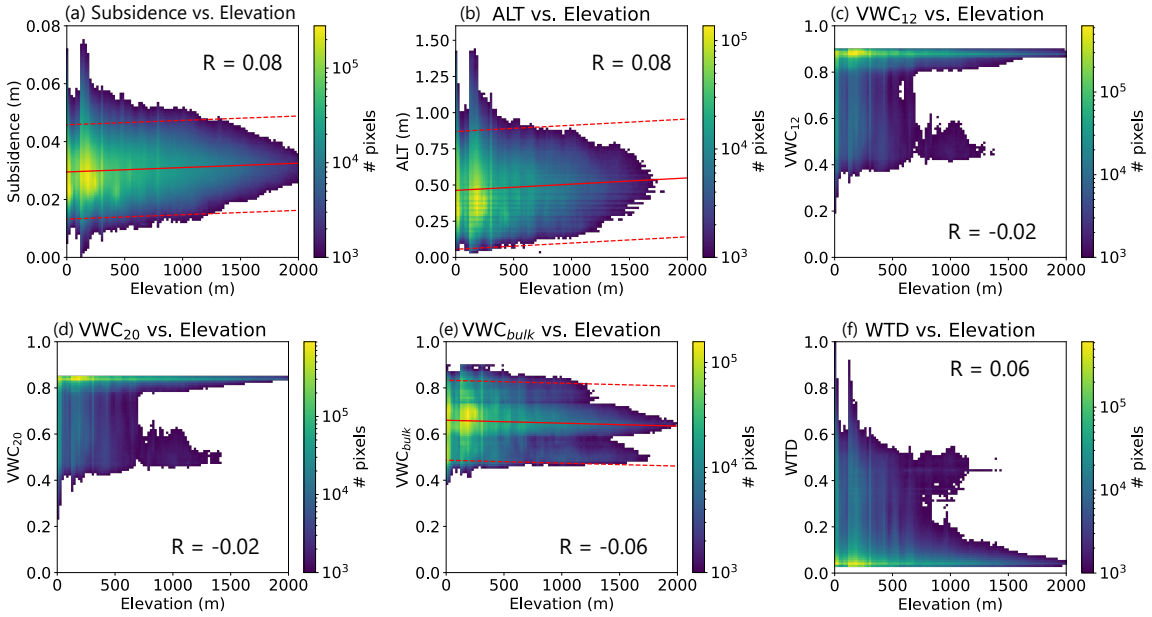

Figure A.2: (a) 2D histogram of subsidence vs. elevation. The correlation coefficient is 0.08 and the regression equation is $Subsidence = 1.5E-6Elevation + 0.030$. (b) Permafrost active layer thickness vs. elevation. The correlation coefficient is 0.08 and the regression equation is $ALT = 4.3E-5Elevation + 0.46$. (c) Elevation vs. VWC_{12}. The correlation coefficient is -0.02. (d) Elevation vs. VWC_{20}. The correlation coefficient is -0.02. (e) VWC_{bulk} vs. elevation. The correlation coefficient is -0.06 and the regression equation is $VWC_{bulk} = -1.3E-5Elevation+0.66$. (f) WTD vs. elevation. The correlation coefficient is 0.06 and the regression equation is $WTD = 2.4E-5Elevation + 0.15$. Near the surface ($VWC_{12}$ and VWC_{20}), the vast majority of points are close to saturation, but at low elevations, there is another population that is partially saturated.

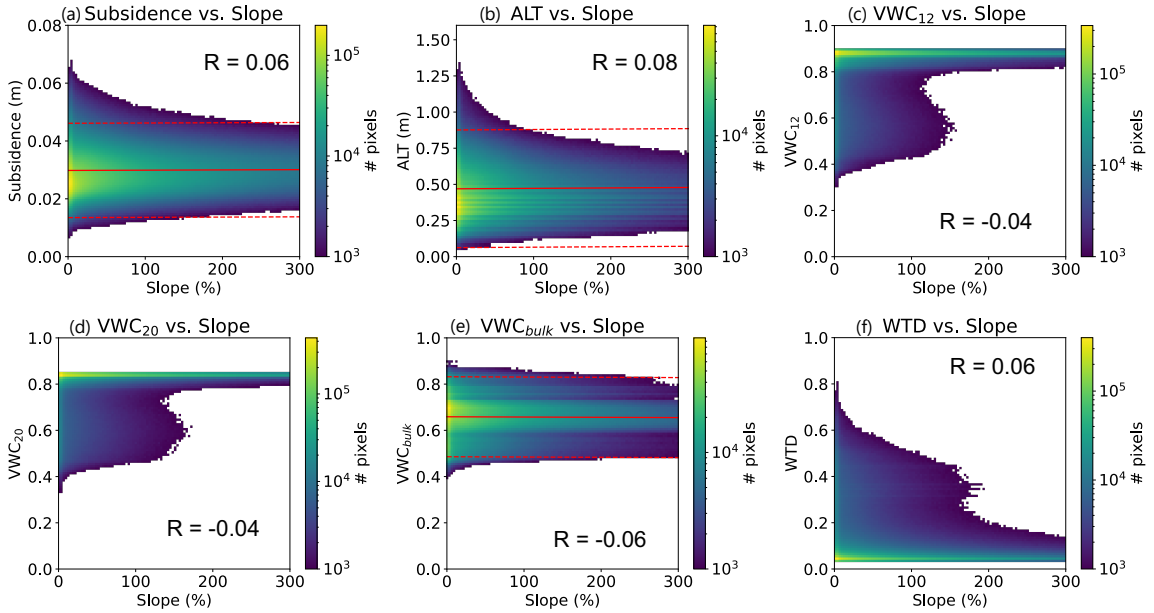

Figure A.3: Comparison of slope to PDO variables across all sites. (a) Slope vs. subsidence. The correlation coefficient is 0.06 and the regression equation is $Subsidence = 9.0E-7Slope + 0.030$. (b) Slope vs. active layer thickness. The correlation coefficient is 0.08 and the regression equation is $ALT = 3.1E-5Slope + 0.47$. (c) Slope vs. VWC_{12}. The correlation coefficient is -0.05. (d) Slope vs. VWC_{20}. The correlation coefficient is -0.05. (e) Slope vs. VWC_{bulk}. The correlation coefficient is -0.07 and the regression equation is $VWC_{bulk} = -1.2E-5Slope + 0.66$. (f) Slope vs. WTD. The correlation coefficient is 0.06.

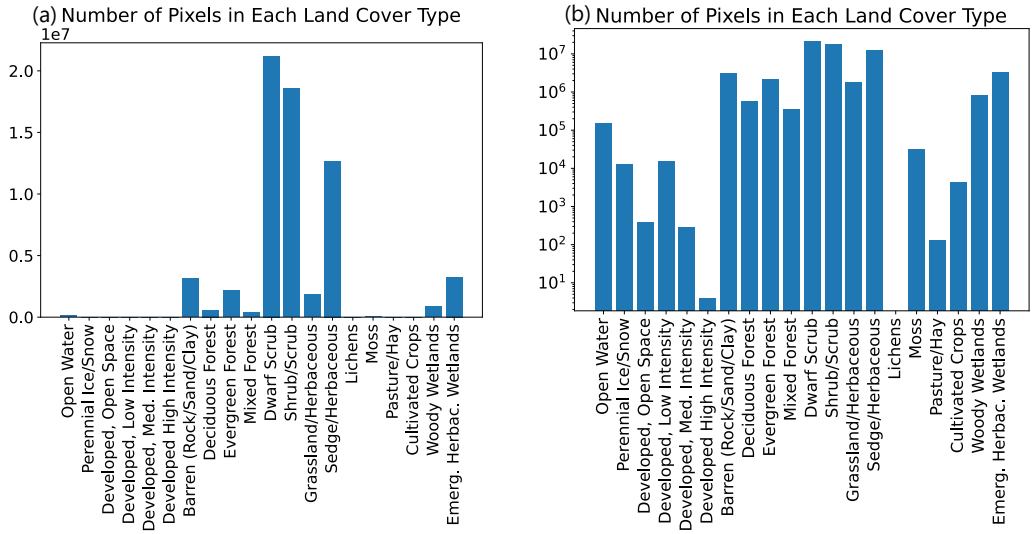

Figure A.4: (a) Linear and (b) logarithmic plots showing the number of pixels of each land cover type in swaths in Alaska covered by ABoVE PDO

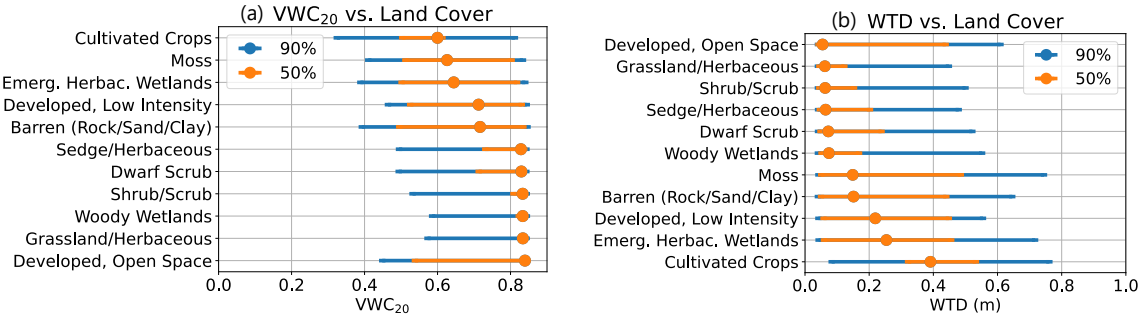

Figure A.5: (a) Distribution of VWC_{20} data for each land cover type. (b) Distribution of WTD for each land cover type.

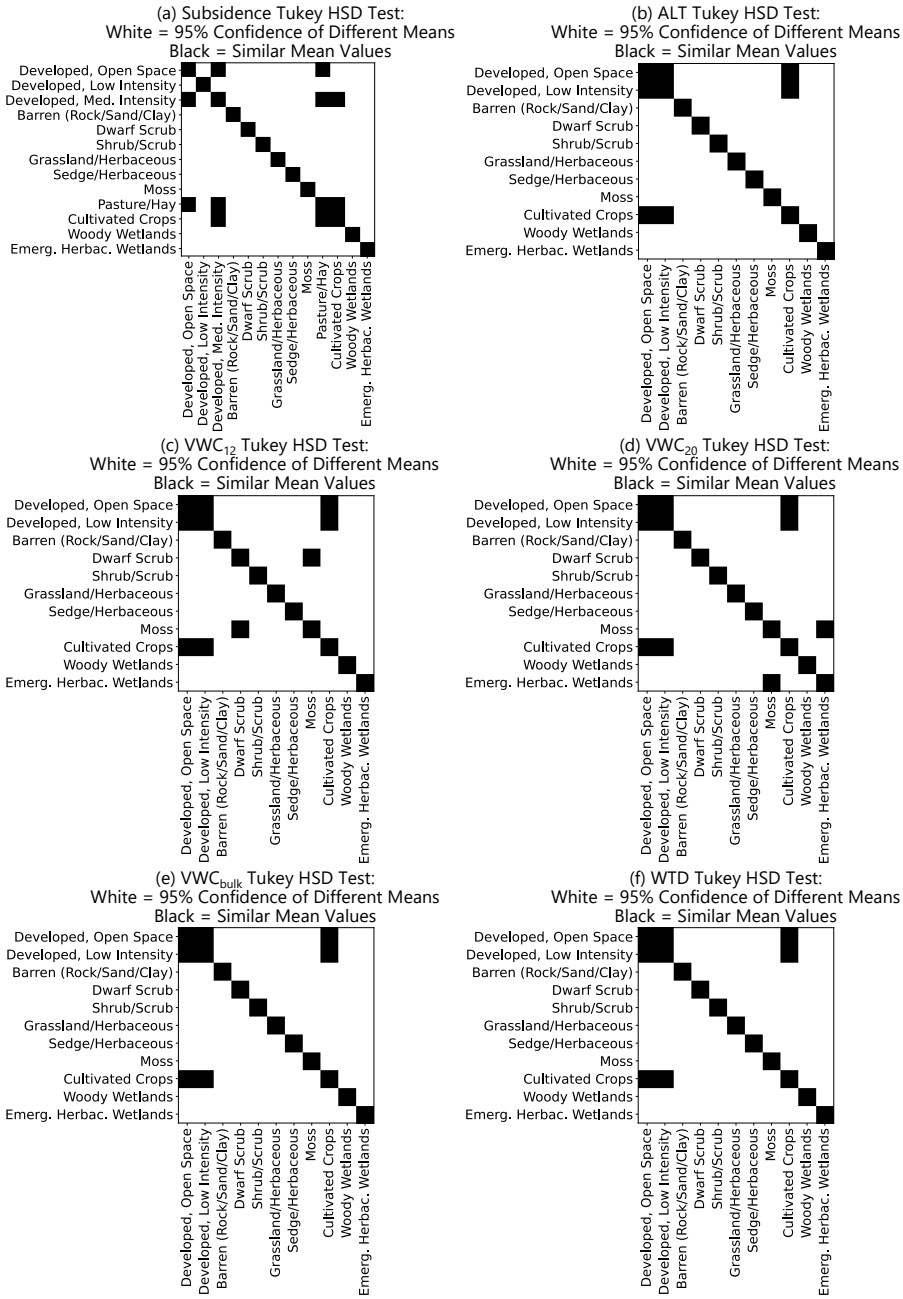

Figure A.6: Tukey's Highly Significant Difference Test: 95% confidence that the difference between the mean value of a variable (e.g. subsidence) in two compared categories has a non-zero difference. (a) Subsidence (b) ALT (c) VWC_{12} (d) VWC_{20} (e) VWC_{bulk} (f) WTD.

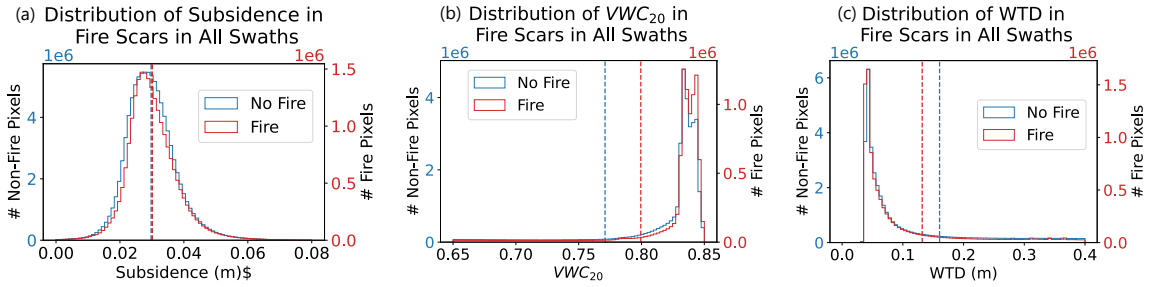

Figure A.7: Populations of PDO variables in burned and unburned areas. (a) Subsidence in burned (mean = 0.0301) and unburned (mean = 0.0298) pixels. (b) VWC_{20} in burned (mean = 0.80) and unburned (mean = 0.77 areas. (c) Water table depth in burned (mean = 0.13) and unburned (mean = 0.16) areas.

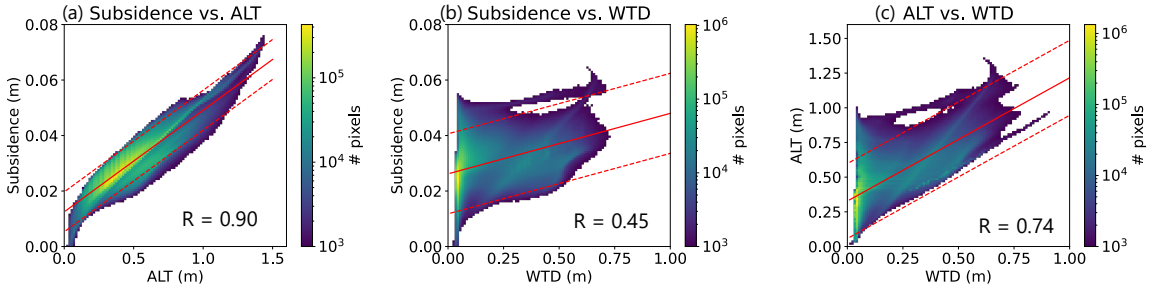

Figure A.8: (a) 2D histogram of subsidence vs. active layer thickness. Correlation coefficient is 0.90 and regression equation is $Subsidence = 0.037ALT + 0.012$. (b) 2D histogram of subsidence vs. WTD. Correlation coefficient is 0.45 and regression equation is $Subsidence = 0.022WTD + 0.026$. (c) 2D histogram of active layer thickness vs. WTD. Correlation coefficient is 0.74 and regression equation is $ALT = 0.89WTD + 0.33$. The strongest correlation (0.90) is between subsidence and ALT, and clear correlations exist between subsidence and WTD (0.45) and ALT and WTD (0.74). Thicker active layers are associated with deeper water tables and greater seasonal subsidence. The frozen soil expansion model used in the PDO retrieval tightly constrains the estimated ALT to the measured subsidence, resulting in the high correlation. The WTD varies more freely in the retrieval because it depends primarily on the P-band reflectance. However, the permafrost underneath the active layer is impermeable to water, so the retrieval ensures the WTD never exceeds ALT. These plots indicate most pixels have a shallow water table within the active layer.

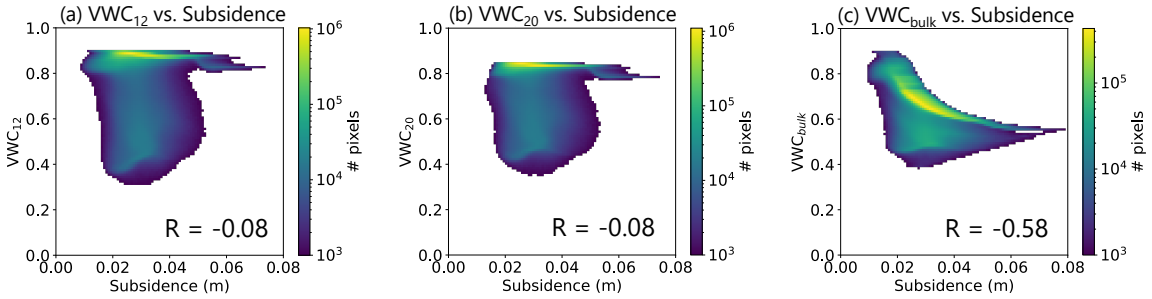

Figure A.9: (a) VWC_{12}. vs. subsidence. (b) VWC_{20} vs. subsidence. (c) VWC_{bulk} vs. subsidence. The relationships between VWC and subsidence appear similar to those between VWC and ALT, in the main body of the text.

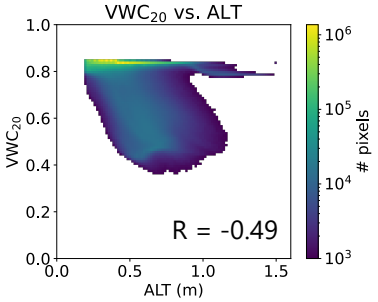

Figure A.10: VWC_{20} vs. active layer thickness.

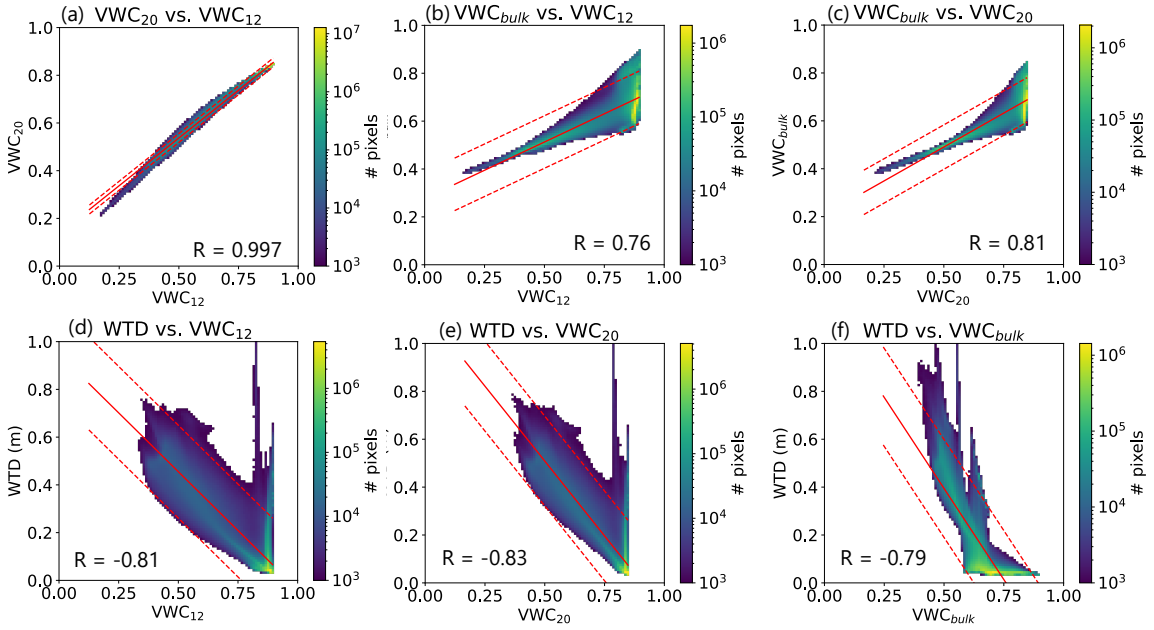

Figure A.11: VWC is highly correlated among different depths. The histogram of VWC_{12} and VWC_{20} appears as a line in the plot. There is a wider spread of possible VWCs at ALT for soil that is highly saturated at lower depths. Low VWC is correlated with high WTD. (a) VWC_{20} vs. VWC_{12}. The correlation coefficient is 0.997 and the regression equation is $VWC_{20} = 0.80VWC_{12} + 0.14$. (b) VWC_{bulk} depth vs. VWC_{12}. The correlation coefficient is 0.76 and the regression equation is $VWC_{bulk} = 0.47VWC_{12} + 0.27$. (c) VWC_{bulk} depth vs. VWC_{20}. The correlation coefficient is 0.81 and the regression equation is $VWC_{bulk} = 0.57VWC_{20} + 0.21$. (d) WTD vs. VWC_{12}. The correlation coefficient is -0.81 and the regression equation is $WTD = -0.98VWC_{12} + 0.95$. (e) WTD vs. VWC_{20}. The correlation coefficient is -0.83 and the regression equation is $WTD = -1.25VWC_{20} + 1.13$ (f) WTD vs. VWC_{bulk}. The correlation coefficient is -0.79 and the regression equation is $WTD = -1.52VWC_{bulk} + 1.15$.

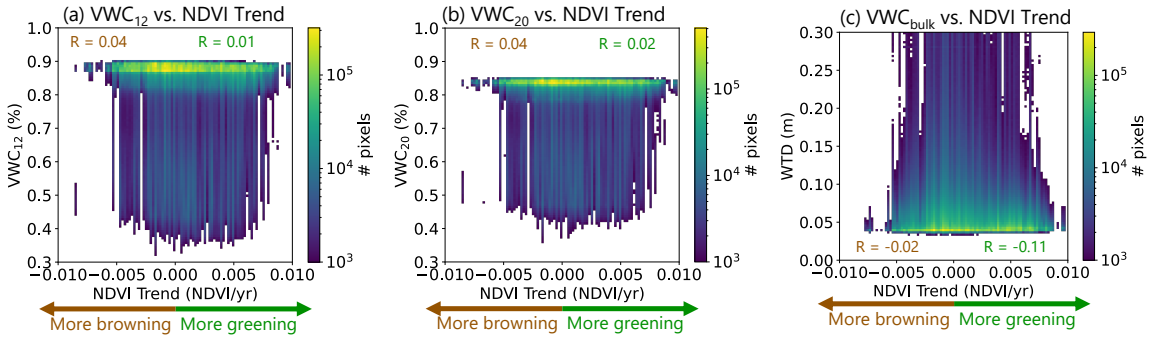

Figure A.12: (a) 2D histogram of VWC_{12} vs. NDVI trend, with fit line. (b) 2D histogram of VWC_{20} depth vs. NDVI trend, with fit line. (c) 2D histogram of WTD vs. NDVI trend, with fit line.

Bibliography

[1] A. Alharthi and J. Lange. Soil water saturation: Dielectric determination. *Water Resources Research*, 23(4):591–595, 1987.

[2] Christian G. Andresen, David M. Lawrence, Cathy J. Wilson, A. David McGuire, Charles Koven, Kevin Schaefer, Elchin Jafarov, Shushi Peng, Xiaodong Chen, Isabelle Gouttevin, Eleanor Burke, Sarah Chadburn, Duoying Ji, Guangsheng Chen, Daniel Hayes, and Wenxin Zhang. Soil moisture and hydrology projections of the permafrost region – a model intercomparison. *The Cryosphere*, 14(2):445–459, 2020.

[3] Homa Ansari, Francesco De Zan, and Richard Bamler. Efficient Phase Estimation for Interferogram Stacks. *IEEE Transactions on Geoscience and Remote Sensing*, 56(7):4109–4125, July 2018.

[4] Homa Ansari, Francesco De Zan, and Alessandro Parizzi. Study of Systematic Bias in Measuring Surface Deformation With SAR Interferometry. *IEEE Transactions on Geoscience and Remote Sensing*, 59(2):1285–1301, February 2021.

[5] NOAA Physical Sciences Laboratory Data and Image Archive. NOAA Hydrometeorology Testbed.

[6] Richard Barnes. RichDEM: Terrain Analysis Software, 2016.

[7] Brian W. Barrett, Edward Dwyer, and Pádraig Whelan. Soil Moisture Retrieval from Active Spaceborne Microwave Observations: An Evaluation of Current Techniques. *Remote Sensing*, 1(3):210–242, September 2009.

[8] P. Berardino, G. Fornaro, R. Lanari, and E. Sansosti. A new algorithm for surface deformation monitoring based on small baseline differential SAR interferograms. *IEEE Transactions on Geoscience and Remote Sensing*, 40(11):2375–2383, November 2002.

[9] Logan T. Berner, Richard Massey, Patrick Jantz, Bruce C. Forbes, Marc Macias-Fauria, Isla Myers-Smith, Timo Kumpula, Gilles Gauthier, Laia Andreu-Hayles, Benjamin V. Gaglioti,

Patrick Burns, Pentti Zetterberg, Rosanne D'Arrigo, and Scott J. Goetz. Summer warming explains widespread but not uniform greening in the Arctic tundra biome. *Nature Communications*, 11(1):4621, 2020.

[10] Rowan Biessel. An Intensity Triplet for the Prediction of Systematic InSAR Closure Phases. Master's thesis, University of Alaska Fairbanks, United States – Alaska, 2023. ISBN: 9798379484873.

[11] Rowan Biessel and Simon Zwieback. An Intensity Triplet for Prediction and Correction of Systematic InSAR Closure Phases, June 2023.

[12] Rowan Biessel and Simon Zwieback. Simulations of Insar Velocity Bias Due to Dielectric Changes and Heterogenous Velocities. In *IGARSS 2023 - 2023 IEEE International Geoscience and Remote Sensing Symposium*, pages 7872–7874, July 2023. ISSN: 2153-7003.

[13] Lindy Blackburn, Dominic W. Pesce, Michael D. Johnson, Maciek Wielgus, Andrew A. Chael, Pierre Christian, and Sheperd S. Doeleman. Closure Statistics in Interferometric Data. *The Astrophysical Journal*, 894(1):31, May 2020.

[14] Philip Blankenau. Evaluation of greenness by NDVI at Oklahoma Mesonet stations., 2016.

[15] D. Blok, M. M. P. D. Heijmans, G. Schaepman-Strub, A. V. Kononov, T. C. Maximov, and F. Berendse. Shrub expansion may reduce summer permafrost thaw in Siberian tundra. *Global Change Biology*, 16(4):1296–1305, 2010.

[16] Olena Boiko, Stefanie Kagone, and Gabriel Senay. Soil properties dataset in the United States, 2021.

[17] Stephan Bojinski, Michel Verstraete, Thomas C. Peterson, Carolin Richter, Adrian Simmons, and Michael Zemp. The Concept of Essential Climate Variables in Support of Climate Research, Applications, and Policy. *Bulletin of the American Meteorological Society*, 95(9):1431–1443, 2014.

[18] Ben Bond-Lamberty, Scott D. Peckham, Stith T. Gower, and Brent E. Ewers. Effects of fire on regional evapotranspiration in the central Canadian boreal forest. *Global Change Biology*, 15(5):1242–1254, 2009.

[19] Fred V. Brock, Kenneth C. Crawford, Ronald L. Elliott, Gerrit W. Cuperus, Steven J. Stadler, Howard L. Johnson, and Michael D. Eilts. The Oklahoma Mesonet: A Technical Overview. *Journal of Atmospheric and Oceanic Technology*, 12(1):5–19, February 1995.

[20] James E. Burt and Gerald M. Barber. Inferential Aspects of Regression Analysis. In *Elementary Statistics for Geographers*, page 484. The Guilford Press, New York, second edition edition, 1995.

[21] Roland Bürgmann, Paul A. Rosen, and Eric J. Fielding. Synthetic Aperture Radar Interferometry to Measure Earth's Surface Topography and Its Deformation. *Annual Review of Earth and Planetary Sciences*, 28(Volume 28, 2000):169–209, May 2000. Publisher: Annual Reviews.

[22] Steven K. Chan, Rajat Bindlish, Peggy E. O'Neill, Eni Njoku, Tom Jackson, Andreas Colliander, Fan Chen, Mariko Burgin, Scott Dunbar, Jeffrey Piepmeier, Simon Yueh, Dara Entekhabi, Michael Cosh, Todd Caldwell, Jeffrey Walker, Xiaoling Wu, Aaron Berg, Tracy Rowlandson, Anna Pacheco, Heather McNairn, Marc Thibeault, Jose Martinez-Fernandez, Angel Gonzalez-Zamora, Mark Seyfried, David Bosch, Patrick Starks, David Goodrich, John Prueger, Michael Palecki, Eric Small, Marek Zreda, Jean-Christophe Calvet, Wade Crow, and Yann Kerr. Assessment of the SMAP Passive Soil Moisture Product. *IEEE Transactions on Geoscience and Remote Sensing*, 54(8):4994–5007, August 2016.

[23] Albert Chen, Andrew D. Parsekian, Kevin Schaefer, Elchin Jafarov, Santosh Panda, Lin Liu, Tingjun Zhang, and Howard Zebker. Ground-penetrating radar-derived measurements of active-layer thickness on the landscape scale with sparse calibration at Toolik and Happy Valley, Alaska. *Geophysics*, 81(2):H9–H19, 2016.

[24] Curtis W. Chen and Howard A. Zebker. Network approaches to two-dimensional phase unwrapping: intractability and two new algorithms. *JOSA A, Vol. 17, Issue 3, pp. 401-414*, March 2000. Publisher: Optica Publishing Group.

[25] Jie Chen, Tonghua Wu, Defu Zou, Lin Liu, Xiaodong Wu, Wenyu Gong, Xiaofan Zhu, Ren Li, Junming Hao, Guojie Hu, Qiangqiang Pang, Jing Zhang, and Sizhong Yang. Magnitudes and patterns of large-scale permafrost ground deformation revealed by Sentinel-1 InSAR on the central Qinghai-Tibet Plateau. *Remote Sensing of Environment*, 268:112778, January 2022.

[26] Jingyi Chen, Yue Wu, Michael O'Connor, M. Bayani Cardenas, Kevin Schaefer, Roger Michaelides, and George Kling. Active layer freeze-thaw and water storage dynamics in permafrost environments inferred from InSAR. *Remote Sensing of Environment*, 248:112007, 2020.

[27] Richard H. Chen, R.J. Michaelides, J. Chen, A.C. Chen, L.K. Clayton, K. Bakian-Dogaheh, L. Huang, E. Jafarov, L. Liu, M. Moghaddam, A.D. Parsekian, T.D. Sullivan, A. Tabatabaeenejad, E. Wig, H.A. Zebker, and Y. Zhao. ABoVE: Active Layer Thickness from Airborne L- and P- band SAR, Alaska, 2017, Ver. 3, 2022. Dataset.

[28] Richard H. Chen, Roger J. Michaelides, Yuhuan Zhao, Lingcao Huang, Elizabeth Wig, Taylor D. Sullivan, Andrew D. Parsekian, Howard A. Zebker, Mahta Moghaddam, and Kevin M. Schaefer. Permafrost Dynamics Observatory (PDO): 2. Joint Retrieval of Permafrost Active Layer Thickness and Soil Moisture From L-Band InSAR and P-Band PolSAR. *Earth and Space Science*, 10(1):e2022EA002453, 2023.

[29] Petr Chylek, Chris Folland, James D. Klett, Muyin Wang, Nick Hengartner, Glen Lesins, and Manvendra K. Dubey. Annual Mean Arctic Amplification 1970–2020: Observed and Simulated by CMIP6 Climate Models. *Geophysical Research Letters*, 49(13):e2022GL099371, 2022.

[30] J. Cihlar and F. T. Ulaby. Dielectric properties of soils as a function of moisture content. Technical Report NASA-CR-141868, NTRS - NASA Technical Reports Server, November 1974.

[31] Leah K. Clayton, Xuhui Lee, and Kevin Schaefer. Recovery of Alaskan Tundra Post-Fire in the Yukon-Kuskokwim Delta, 2023.

[32] Leah K. Clayton, Kevin Schaefer, Michael J. Battaglia, Laura Bourgeau-Chavez, Jingyi Chen, Richard H. Chen, Albert Chen, Kazem Bakian-Dogaheh, Sarah Grelik, Elchin Jafarov, Lin Liu, Roger John Michaelides, Mahta Moghaddam, Andrew D. Parsekian, Adrian V. Rocha, Sean R. Schaefer, Taylor Sullivan, Alireza Tabatabaeenejad, Kang Wang, Cathy J. Wilson, Howard A. Zebker, Tingjun Zhang, and Yuhuan Zhao. Active layer thickness as a function of soil water content. *Environmental Research Letters*, 16(5):055028, 2021. Publisher: IOP Publishing.

[33] Andreas Colliander, Michael H. Cosh, Laura Bourgeau-Chavez, Victoria R. Kelly, Simon Kraatz, Paul Siqueira, Victoria A. Walker, Xingjian Chen, Alexandre Roy, Tarendra Lakhankar, Kyle C. McDonald, Nicholas Steiner, Mehmet Kurum, Seung-bum Kim, Aaron Berg, Xiaolan Xu, Sidharth Misra, Mehmet Ogut, Cristina Vittucci, John S. Kimball, Dara Entekhabi, and Simon H. Yueh. SMAP Validation Experiment 2019–2022 (SMAPVEX19–22): Field Campaign to Improve Soil Moisture and Vegetation Optical Depth Retrievals in Temperate Forests. *IEEE Journal of Selected Topics in Applied Earth Observations and Remote Sensing*, 18:10749–10771, 2025.

[34] Copernicus sentinel data 2018-2021. Retrieved from ASF DAAC, some processing by ESA.

[35] Christopher J. Crawford, David P. Roy, Saeed Arab, Christopher Barnes, Eric Vermote, Glynn Hulley, Aaron Gerace, Mike Choate, Christopher Engebretson, Esad Micijevic, Gail Schmidt, Cody Anderson, Martha Anderson, Michelle Bouchard, Bruce Cook, Ray Dittmeier, Danny Howard, Calli Jenkerson, Minsu Kim, Tania Kleyians, Thomas Maiersperger, Chase Mueller, Christopher Neigh, Linda Owen, Benjamin Page, Nima Pahlevan, Rajagopalan Rengarajan, Jean-Claude Roger, Kristi Sayler, Pat Scaramuzza, Sergii Skakun, Lin Yan, Hankui K. Zhang, Zhe Zhu, and Steve Zahn. The 50-year Landsat collection 2 archive. *Science of Remote Sensing*, 8:100103, December 2023. Dataset.

[36] Calum X. Cunningham, Grant J. Williamson, and David M. J. S. Bowman. Increasing frequency and intensity of the most extreme wildfires on Earth. *Nature Ecology & Evolution*, 8(8):1420–1425, August 2024. Publisher: Nature Publishing Group.

[37] Narendra N. Das, Dara Entekhabi, and Eni G. Njoku. An Algorithm for Merging SMAP Radiometer and Radar Data for High-Resolution Soil-Moisture Retrieval. *IEEE Transactions on Geoscience and Remote Sensing*, 49(5):1504–1512, May 2011.

[38] Betsabe de la Barreda-Bautista, Doreen S. Boyd, Martha Ledger, Matthias B. Siewert, Chris Chandler, Andrew V. Bradley, David Gee, David J. Large, Johan Olofsson, Andrew Sowter, and Sofie Sjögersten. Towards a Monitoring Approach for Understanding Permafrost Degradation and Linked Subsidence in Arctic Peatlands. *Remote Sensing*, 14(3):444, 2022.

[39] Francesco De Zan and Giorgio Gomba. Vegetation and soil moisture inversion from SAR closure phases: First experiments and results. *Remote Sensing of Environment*, 217:562–572, November 2018.

[40] Francesco De Zan, Alessandro Parizzi, Pau Prats-Iraola, and Paco López-Dekker. A SAR Interferometric Model for Soil Moisture. *IEEE Transactions on Geoscience and Remote Sensing*, 52(1):418–425, January 2014.

[41] Francesco De Zan, Mariantonietta Zonno, and Paco López-Dekker. Phase Inconsistencies and Multiple Scattering in SAR Interferometry. *IEEE Transactions on Geoscience and Remote Sensing*, 53(12):6608–6616, December 2015.

[42] Myron C. Dobson, Fawwaz T. Ulaby, Martti T. Hallikainen, and Mohamed A. El-rayes. Microwave Dielectric Behavior of Wet Soil-Part II: Dielectric Mixing Models. *IEEE Transactions on Geoscience and Remote Sensing*, GE-23(1):35–46, January 1985.

[43] Francesco Falabella and Antonio Pepe. On the Phase Nonclosure of Multilook SAR Interferogram Triplets. *IEEE Transactions on Geoscience and Remote Sensing*, 60:1–17, 2022.

[44] Heresh Fattahi, Mark Simons, and Piyush Agram. InSAR Time-Series Estimation of the Ionospheric Phase Delay: An Extension of the Split Range-Spectrum Technique. *IEEE Transactions on Geoscience and Remote Sensing*, 55(10):5984–5996, October 2017.

[45] A. Ferretti, C. Prati, and F. Rocca. Permanent scatterers in SAR interferometry. *IEEE Transactions on Geoscience and Remote Sensing*, 39(1):8–20, January 2001.

[46] Andrew K. Gabriel, Richard M. Goldstein, and Howard A. Zebker. Mapping small elevation changes over large areas: Differential radar interferometry. *Journal of Geophysical Research: Solid Earth*, 94(B7):9183–9191, 1989.

[47] J.F. Galantowicz, D. Entekhabi, and E.G. Njoku. Tests of sequential data assimilation for retrieving profile soil moisture and temperature from observed L-band radiobrightness. *IEEE Transactions on Geoscience and Remote Sensing*, 37(4):1860–1870, July 1999.

[48] D. L. Galloway, K. W. Hudnut, S. E. Ingebritsen, S. P. Phillips, G. Peltzer, F. Rogez, and P. A. Rosen. Detection of aquifer system compaction and land subsidence using interferometric synthetic aperture radar, Antelope Valley, Mojave Desert, California. *Water Resources Research*, 34(10):2573–2585, 1998.

[49] Scott J Goetz, Charles Miller, Peter Griffith, Abhishek Chatterjee, Laura Bourgeau-Chavez, David Butman, Howard Epstein, Nancy French, Elizabeth Hoy, John S Kimball, Elisabeth Larson, Tatiana Loboda, Michelle Mack, Mahta Moghaddam, Paul Montesano, Michael Rawlins, Adrian V Rocha, and Brendan M Rogers. An overview of NASA's Arctic Boreal Vulnerability Experiment (ABoVE): Development, implementation, advances and knowledge gaps (in review). *Environmental Research Letters*, page 30, August 2021.

[50] Richard M. Goldstein, Hermann Engelhardt, Barclay Kamb, and Richard M. Frolich. Satellite Radar Interferometry for Monitoring Ice Sheet Motion: Application to an Antarctic Ice Stream. *Science*, 262(5139):1525–1530, December 1993. Publisher: American Association for the Advancement of Science.

[51] Alessio Gusmeroli, Lin Liu, Kevin Schaefer, Tingjun Zhang, Timothy Schaefer, and Guido Grosse. Active Layer Stratigraphy and Organic Layer Thickness at a Thermokarst Site in Arctic Alaska Identified Using Ground Penetrating Radar. *Arctic, Antarctic, and Alpine Research*, 47(2):195–202, 2015.

[52] M. Hallikainen, F. Ulaby, and M. Abdelrazik. Dielectric properties of snow in the 3 to 37 GHz range. *IEEE Transactions on Antennas and Propagation*, 34(11):1329–1340, November 1986.

[53] Martti T. Hallikainen, Fawwaz T. Ulaby, Myron C. Dobson, Mohamed A. El-rayes, and Lil-kun Wu. Microwave Dielectric Behavior of Wet Soil-Part 1: Empirical Models and Experimental Observations. *IEEE Transactions on Geoscience and Remote Sensing*, GE-23(1):25–34, January 1985.

[54] Monique M. P. D. Heijmans, Runa I Magnusson, Mark J. Lara, Gerald V. Frost, Isla H. Myers-Smith, Jacobus van Huissteden, M. Torre Jorgenson, Alexander N. Fedorov, Howard E. Epstein, David M. Lawrence, and Juul Limpens. Tundra vegetation change and impacts on permafrost. *Nature Reviews Earth & Environment*, 3(1):68–84, 2022.

[55] LAURA L. Hess, JOHN M. Melack, and DAVID S. Simonett. Radar detection of flooding beneath the forest canopy: a review. *International Journal of Remote Sensing*, 11(7):1313–1325, July 1990.

[56] Jan Hjort, Olli Karjalainen, Juha Aalto, Sebastian Westermann, Vladimir E. Romanovsky, Frederick E. Nelson, Bernd Etzelmüller, and Miska Luoto. Degrading permafrost puts Arctic infrastructure at risk by mid-century. *Nature Communications*, 9(1):5147, 2018.

[57] Jean E. Holloway, Antoni G. Lewkowicz, Thomas A. Douglas, Xiaoying Li, Merritt R. Turetsky, Jennifer L. Baltzer, and Huijun Jin. Impact of wildfire on permafrost landscapes: A review of recent advances and future prospects. *Permafrost and Periglacial Processes*, 31(3):371–382, 2020. _eprint: https://onlinelibrary.wiley.com/doi/pdf/10.1002/ppp.2048.

[58] Natan Holtzman, Alexandra Konings, Alexandre Roy, Michael Cosh, Simon Kraatz, Paul Siqueira, and Andreas Colliander. SMAPVEX19-22 Massachusetts Vegetation Optical Depth, Version 1, 2020.

[59] Nataniel M. Holtzman, Leander D. L. Anderegg, Simon Kraatz, Alex Mavrovic, Oliver Sonnentag, Christoforos Pappas, Michael H. Cosh, Alexandre Langlois, Tarendra Lakhankar, Derek Tesser, Nicholas Steiner, Andreas Colliander, Alexandre Roy, and Alexandra G. Konings. L-band vegetation optical depth as an indicator of plant water potential in a temperate deciduous forest stand. *Biogeosciences*, 18(2):739–753, February 2021. Publisher: Copernicus GmbH.

[60] Jennifer L. Hrobak, Gary Schmunk, and Mary Lynch. Alaska Large Fire Database, 2023. Dataset.

[61] Bradley G. Illston, Jeffrey B. Basara, Christopher A. Fiebrich, Kenneth C. Crawford, Eric Hunt, Daniel K. Fisher, Ronald Elliott, and Karen Humes. Mesoscale Monitoring of Soil Moisture across a Statewide Network. *Journal of Atmospheric and Oceanic Technology*, 25(2):167–182, February 2008.

[62] H. Iwasaki, H. Saito, K. Kuwao, T. C. Maximov, and S. Hasegawa. Forest decline caused by high soil water conditions in a permafrost region. *Hydrology and Earth System Sciences*, 14(2):301–307, 2010.

[63] E. E. Jafarov, A. D. Parsekian, K. Schaefer, L. Liu, A. C. Chen, S. K. Panda, and T. Zhang. Estimating active layer thickness and volumetric water content from ground penetrating radar measurements in Barrow, Alaska. *Geoscience Data Journal*, 4(2):72–79, 2017.

[64] Benjamin M. Jones, Guido Grosse, Christopher D. Arp, Eric Miller, Lin Liu, Daniel J. Hayes, and Christopher F. Larsen. Recent Arctic tundra fire initiates widespread thermokarst development. *Scientific Reports*, 5(1):15865, 2015. Publisher: Nature Publishing Group.

[65] M T Jorgenson and T E Osterkamp. Response of boreal ecosystems to varying modes of permafrost degradation. *Canadian Journal of Forest Research*, 35(9):2100–2111, 2005. Publisher: NRC Research Press.

[66] Junchang Ju and Jeffrey G. Masek. The vegetation greenness trend in Canada and US Alaska from 1984–2012 Landsat data. *Remote Sensing of Environment*, 176:1–16, 2016.

[67] Kleanthis Karamvasis and Vassilia Karathanassi. Soil moisture estimation from Sentinel-1 interferometric observations over arid regions. *arXiv preprint*, 2022.

[68] D. M. Lawrence, C. D. Koven, S. C. Swenson, W. J. Riley, and A. G. Slater. Permafrost thaw and resulting soil moisture changes regulate projected high-latitude CO2 and CH4 emissions. *Environmental Research Letters*, 10(9):094011, 2015. Publisher: IOP Publishing.

[69] Antoni G. Lewkowicz and Robert G. Way. Extremes of summer climate trigger thousands of thermokarst landslides in a High Arctic environment. *Nature Communications*, 10(1):1329, April 2019. Publisher: Nature Publishing Group.

[70] Anna Liljedahl, Larry Hinzman, Robert Busey, and Kenji Yoshikawa. Physical short-term changes after a tussock tundra fire, Seward Peninsula, Alaska. *Journal of Geophysical Research: Earth Surface*, 112(F2), 2007. _eprint: https://onlinelibrary.wiley.com/doi/pdf/10.1029/2006JF000554.

[71] John Little. National Fire Database Fire Polygon Data, 2023. Dataset.

[72] L. Liu, K. Schaefer, A. Gusmeroli, G. Grosse, B. M. Jones, T. Zhang, A. D. Parsekian, and H. A. Zebker. Seasonal thaw settlement at drained thermokarst lake basins, Arctic Alaska. *The Cryosphere*, 8(3):815–826, 2014.

[73] L. Liu, K. M. Schaefer, A. C. Chen, A. Gusmeroli, H. A. Zebker, and T. Zhang. Remote sensing measurements of thermokarst subsidence using InSAR. *Journal of Geophysical Research: Earth Surface*, 120(9):1935–1948, 2015.

[74] Lin Liu, Elchin E. Jafarov, Kevin M. Schaefer, Benjamin M. Jones, Howard A. Zebker, Christopher A. Williams, John Rogan, and Tingjun Zhang. InSAR detects increase in surface subsidence caused by an Arctic tundra fire. *Geophysical Research Letters*, 41(11):3906–3913, 2014.

[75] Lin Liu, Kevin Schaefer, Tingjun Zhang, and John Wahr. Estimating 1992–2000 average active layer thickness on the Alaskan North Slope from remotely sensed surface subsidence. *Journal of Geophysical Research: Earth Surface*, 117(F1), 2012.

[76] Lin Liu, Tingjun Zhang, and John Wahr. InSAR measurements of surface deformation over permafrost on the North Slope of Alaska. *Journal of Geophysical Research: Earth Surface*, 115(F3), 2010.

[77] Michael M. Loranty, Wil Lieberman-Cribbin, Logan T. Berner, Susan M. Natali, Scott J. Goetz, Heather D. Alexander, and Alexander L. Kholodov. Spatial variation in vegetation productivity trends, fire disturbance, and soil carbon across arctic-boreal permafrost ecosystems. *Environmental Research Letters*, 11(9):095008, 2016.

[78] J. Ross Mackay. Disturbances to the tundra and forest tundra environment of the western Arctic. *Canadian Geotechnical Journal*, 7(4):420–432, 1970.

[79] Yasser Maghsoudi, Andrew Hooper, Tim Wright, Milan Lazecky, and Homa Ansari. Characterizing and correcting phase biases in short-term, multilooked interferograms. *Remote Sensing of Environment*, 275:113022, June 2022.

[80] Didier Massonnet, Pierre Briole, and Alain Arnaud. Deflation of Mount Etna monitored by spaceborne radar interferometry. *Nature*, 375(6532):567–570, June 1995.

[81] Didier Massonnet, Marc Rossi, César Carmona, Frédéric Adragna, Gilles Peltzer, Kurt Feigl, and Thierry Rabaute. The displacement field of the Landers earthquake mapped by radar interferometry. *Nature*, 364(6433):138–142, July 1993.

[82] Kaighin A. McColl, Jur Vogelzang, Alexandra G. Konings, Dara Entekhabi, María Piles, and Ad Stoffelen. Extended triple collocation: Estimating errors and correlation coefficients with respect to an unknown target. *Geophysical Research Letters*, 41(17):6229–6236, 2014.

[83] Kaighin A. McColl, Wei Wang, Bin Peng, Ruzbeh Akbar, Daniel J. Short Gianotti, Hui Lu, Ming Pan, and Dara Entekhabi. Global characterization of surface soil moisture drydowns. *Geophysical Research Letters*, 44(8):3682–3690, 2017.

[84] Piyush Mehta, Stefan Siebert, Matti Kummu, Qinyu Deng, Tariq Ali, Landon Marston, Wei Xie, and Kyle Frankel Davis. Half of twenty-first century global irrigation expansion has been in water-stressed regions. *Nature Water*, 2(3):254–261, March 2024. Publisher: Nature Publishing Group.

[85] R. J. Michaelides, M. B. Bryant, M. R. Siegfried, and A. A. Borsa. Quantifying Surface-Height Change Over a Periglacial Environment With ICESat-2 Laser Altimetry. *Earth and Space Science*, 8(8):e2020EA001538, 2021.

[86] Roger Michaelides and Howard Zebker. Feasibility of Retrieving Soil Moisture from InSAR Decorrelation Phase and Closure Phase. In *IGARSS 2020*, pages 12–15, September 2020.

[87] Roger J. Michaelides, Richard H. Chen, Yuhuan Zhao, Kevin Schaefer, Andrew D. Parsekian, Taylor Sullivan, Mahta Moghaddam, Howard A. Zebker, Lin Liu, Xingyu Xu, and Jingyi Chen. Permafrost Dynamics Observatory—Part I: Postprocessing and Calibration Methods of UAVSAR L-Band InSAR Data for Seasonal Subsidence Estimation. *Earth and Space Science*, 8(7):e2020EA001630, 2021.

[88] Roger J Michaelides, Kevin Schaefer, Howard A Zebker, Andrew Parsekian, Lin Liu, Jingyi Chen, Susan Natali, Sarah Ludwig, and Sean R Schaefer. Inference of the impact of wildfire

on permafrost and active layer thickness in a discontinuous permafrost region using the remotely sensed active layer thickness (ReSALT) algorithm. *Environmental Research Letters*, 14(3):035007, 2019.

[89] Roger J. Michaelides, Howard A. Zebker, and Yujie Zheng. An Algorithm for Estimating and Correcting Decorrelation Phase From InSAR Data Using Closure Phase Triplets. *IEEE Transactions on Geoscience and Remote Sensing*, 57(12):10390–10397, December 2019.

[90] Roger John Michaelides, Howard A. Zebker, Rosemary Knight, Alexandra Konings, and Dustin Schroeder. *Quantifying permafrost processes and soil moisture with interferometric phase and closure phase*. PhD thesis, Stanford University, Stanford, California, 2020.

[91] Charles Miller, Peter C. Griffith, Elizabeth Hoy, Naiara S. Pinto, Yunling Lou, Scott Hensley, Bruce D. Chapman, Jennifer Baltzer, Kazem Bakian-Dogaheh, W. Robert Bolton, Laura Bourgeau-Chavez, Richard H. Chen, Byung-Hun Choe, Leah K. Clayton, Thomas A. Douglas, Nancy French, Jean E. Holloway, Gang Hong, Lingcao Huang, Go Iwahana, Liza Jenkins, John S. Kimball, Tatiana Loboda, Michelle Mack, Philip Marsh, Roger J. Michaelides, Mahta Moghaddam, Andrew Parsekian, Kevin Schaefer, Paul R. Siqueira, Debjani Singh, Alireza Tabatabaeenejad, Merritt Turetsky, Ridha Touzi, Elizabeth Wig, Cathy Wilson, Paul Wilson, Stan D. Wullschleger, Yonghong Yi, Howard A. Zebker, Yu Zhang, Yuhuan Zhao, and Scott J. Goetz. The ABoVE L-band and P-band Airborne SAR Surveys. *Earth System Science Data Discussions*, pages 1–37, 2023. Publisher: Copernicus GmbH.

[92] Kimberley R. Miner, Merritt R. Turetsky, Edward Malina, Annett Bartsch, Johanna Tamminen, A. David McGuire, Andreas Fix, Colm Sweeney, Clayton D. Elder, and Charles E. Miller. Permafrost carbon emissions in a changing Arctic. *Nature Reviews Earth & Environment*, 3(1):55–67, 2022.

[93] Kyle D. Murray, David P. S. Bekaert, and Rowena B. Lohman. Tropospheric corrections for InSAR: Statistical assessments and applications to the Central United States and Mexico. *Remote Sensing of Environment*, 232:111326, October 2019.

[94] I. H. Myers-Smith, J. W. Harden, M. Wilmking, C. C. Fuller, A. D. McGuire, and F. S. Iii Chapin. Wetland succession in a permafrost collapse: interactions between fire and thermokarst. *Biogeosciences*, 5(5):1273–1286, 2008. Publisher: Copernicus GmbH.

[95] Isla H. Myers-Smith, Jeffrey T. Kerby, Gareth K. Phoenix, Jarle W. Bjerke, Howard E. Epstein, Jakob J. Assmann, Christian John, Laia Andreu-Hayles, Sandra Angers-Blondin, Pieter S. A. Beck, Logan T. Berner, Uma S. Bhatt, Anne D. Bjorkman, Daan Blok, Anders Bryn, Casper T. Christiansen, J. Hans C. Cornelissen, Andrew M. Cunliffe, Sarah C. Elmendorf, Bruce C.

Forbes, Scott J. Goetz, Robert D. Hollister, Rogier de Jong, Michael M. Loranty, Marc Macias-Fauria, Kadmiel Maseyk, Signe Normand, Johan Olofsson, Thomas C. Parker, Frans-Jan W. Parmentier, Eric Post, Gabriela Schaepman-Strub, Frode Stordal, Patrick F. Sullivan, Haydn J. D. Thomas, Hans Tømmervik, Rachael Treharne, Craig E. Tweedie, Donald A. Walker, Martin Wilmking, and Sonja Wipf. Complexity revealed in the greening of the Arctic. *Nature Climate Change*, 10(2):106–117, 2020. Number: 2 Publisher: Nature Publishing Group.

[96] Ake L. Nauta, Monique M. P. D. Heijmans, Daan Blok, Juul Limpens, Bo Elberling, Angela Gallagher, Bingxi Li, Roman E. Petrov, Trofim C. Maximov, Jacobus van Huissteden, and Frank Berendse. Permafrost collapse after shrub removal shifts tundra ecosystem to a methane source. *Nature Climate Change*, 5(1):67–70, 2015.

[97] F. E. Nelson, N. I. Shiklomanov, G. R. Mueller, K. M. Hinkel, D. A. Walker, and J. G. Bockheim. Estimating Active-Layer Thickness over a Large Region: Kuparuk River Basin, Alaska, U.S.A. *Arctic and Alpine Research*, 29(4):367–378, 1997. Publisher: INSTAAR, University of Colorado.

[98] Frederick E. Nelson, Nikolay I. Shiklomanov, and Kelsey E. Nyland. Cool, CALM, collected: the Circumpolar Active Layer Monitoring program and network. *Polar Geography*, 44(3):155–166, 2021.

[99] Emily L. Ogden, Steven G. Cumming, Sharon L. Smith, Merritt R. Turetsky, and Jennifer L. Baltzer. Permafrost thaw induces short-term increase in vegetation productivity in northwestern Canada. *Global Change Biology*, n/a(n/a), 2023.

[100] Jonathan A. O'Donnell, M. Torre Jorgenson, Jennifer W. Harden, A. David McGuire, Mikhail Z. Kanevskiy, and Kimberly P. Wickland. The Effects of Permafrost Thaw on Soil Hydrologic, Thermal, and Carbon Dynamics in an Alaskan Peatland. *Ecosystems*, 15(2):213–229, March 2012.

[101] Jeonghwan Park, Rajat Bindlish, Alexandra Bringer, Dustin Horton, and Joel T. Johnson. Soil Moisture Retrieval using a Time-Series Ratio Algorithm for the Nisar Mission. In *IEEE Geophys. Rem. Sens. Symp. (IGARSS)*, pages 5873–5876, July 2021. ISSN: 2153-7003.

[102] Andrew D. Parsekian, Richard H. Chen, Roger J. Michaelides, Taylor D. Sullivan, Leah K. Clayton, Lingcao Huang, Yuhuan Zhao, Elizabeth Wig, Mahta Moghaddam, Howard Zebker, and Kevin Schaefer. Validation of Permafrost Active Layer Estimates from Airborne SAR Observations. *Remote Sensing*, 13(15):2876, 2021.

[103] Xiaoqing Peng, Tingjun Zhang, Oliver W. Frauenfeld, Shijin Wang, Lina Qiao, Ran Du, and Cuicui Mu. Northern Hemisphere Greening in Association With Warming Permafrost. *Journal of Geophysical Research: Biogeosciences*, 125(1):e2019JG005086, 2020.

[104] Karissa Pepin and Howard Zebker. Aliasing in InSAR 2-D Phase Unwrapping and Time Series. *IEEE Transactions on Geoscience and Remote Sensing*, 62:1–17, 2024.

[105] Nathalie Pettorelli, Jon Olav Vik, Atle Mysterud, Jean-Michel Gaillard, Compton J. Tucker, and Nils Chr Stenseth. Using the satellite-derived NDVI to assess ecological responses to environmental change. *Trends in Ecology & Evolution*, 20(9):503–510, 2005.

[106] Claire Porter, Paul Morin, Ian Howat, Myoung-Jon Noh, Brian Bates, Kenneth Peterman, Scott Keesey, Matthew Schlenk, Judith Gardiner, Karen Tomko, Michael Willis, Cole Kelleher, Michael Cloutier, Eric Husby, Steven Foga, Hitomi Nakamura, Melisa Platson, Michael Wethington, Cathleen Williamson, Gregory Bauer, Jeremy Enos, Galen Arnold, William Kramer, Peter Becker, Abhijit Doshi, Cristelle D'Souza, Pat Cummens, Fabien Laurier, and Mikkel Bojesen. ArcticDEM, Version 3, 2018. Dataset.

[107] Christopher Potter and Olivia Alexander. Changes in Vegetation Phenology and Productivity in Alaska Over the Past Two Decades. *Remote Sensing*, 12(10):1546, 2020.

[108] Stephen J. Pyne. *Introduction to Wildland Fire: Fire Management in the United States*. John Wiley & Sons, 1984.

[109] M. A. Rawlins, D. J. Nicolsky, K. C. McDonald, and V. E. Romanovsky. Simulating soil freeze/thaw dynamics with an improved pan-Arctic water balance model. *Journal of Advances in Modeling Earth Systems*, 5(4):659–675, 2013.

[110] Wesley J. Rondinelli, Brian K. Hornbuckle, Jason C. Patton, Michael H. Cosh, Victoria A. Walker, Benjamin D. Carr, and Sally D. Logsdon. Different Rates of Soil Drying after Rainfall Are Observed by the SMOS Satellite and the South Fork in situ Soil Moisture Network. *Journal of Hydrometeorology*, 16(2):889–903, April 2015.

[111] H. Rott and A. Siegel. Analysis of mass movements in alpine terrain by means of SAR interferometry. In *IEEE 1999 International Geoscience and Remote Sensing Symposium. IGARSS'99 (Cat. No.99CH36293)*, volume 4, pages 1933–1936 vol.4, June 1999.

[112] L. Rouyet, O. Karjalainen, P. Niittynen, J. Aalto, M. Luoto, T. R. Lauknes, Y. Larsen, and J. Hjort. Environmental Controls of InSAR-Based Periglacial Ground Dynamics in a Sub-Arctic Landscape. *Journal of Geophysical Research: Earth Surface*, 126(7):e2021JF006175, 2021. _eprint: https://onlinelibrary.wiley.com/doi/pdf/10.1029/2021JF006175.

[113] D. P. Roy, V. Kovalskyy, H. K. Zhang, E. F. Vermote, L. Yan, S. S. Kumar, and A. Egorov. Characterization of Landsat-7 to Landsat-8 reflective wavelength and normalized difference vegetation index continuity. *Remote Sensing of Environment*, 185:57–70, 2016.

[114] Kevin Schaefer, Lin Liu, Andrew Parsekian, Elchin Jafarov, Albert Chen, Tingjun Zhang, Alessio Gusmeroli, Santosh Panda, Howard A. Zebker, and Tim Schaefer. Remotely Sensed Active Layer Thickness (ReSALT) at Barrow, Alaska Using Interferometric Synthetic Aperture Radar. *Remote Sensing*, 7(4):3735–3759, 2015.

[115] Kevin Schaefer, Tingjun Zhang, Lori Bruhwiler, and Andrew P. Barrett. Amount and timing of permafrost carbon release in response to climate warming. *Tellus B*, 63(2):165–180, 2011.

[116] E. a. G. Schuur, A. D. McGuire, C. Schädel, G. Grosse, J. W. Harden, D. J. Hayes, G. Hugelius, C. D. Koven, P. Kuhry, D. M. Lawrence, S. M. Natali, D. Olefeldt, V. E. Romanovsky, K. Schaefer, M. R. Turetsky, C. C. Treat, and J. E. Vonk. Climate change and the permafrost carbon feedback. *Nature*, 520(7546):171–179, 2015.

[117] Edward A. G. Schuur, Jason G. Vogel, Kathryn G. Crummer, Hanna Lee, James O. Sickman, and T. E. Osterkamp. The effect of permafrost thaw on old carbon release and net carbon exchange from tundra. *Nature*, 459(7246):556–559, May 2009. Publisher: Nature Publishing Group.

[118] C. P. Scott, R. B. Lohman, and T. E. Jordan. InSAR constraints on soil moisture evolution after the March 2015 extreme precipitation event in Chile. *Scientific Reports*, 7(1):4903, July 2017.

[119] Ad Stoffelen. Toward the true near-surface wind speed: Error modeling and calibration using triple collocation. *Journal of Geophysical Research: Oceans*, 103(C4):7755–7766, 1998.

[120] Dmitry Streletskiy, Oleg Anisimov, and Alexander Vasiliev. Chapter 10 - Permafrost Degradation. In John F. Shroder, Wilfried Haeberli, and Colin Whiteman, editors, *Snow and Ice-Related Hazards, Risks, and Disasters*, Hazards and Disasters Series, pages 303–344. Academic Press, Boston, 2015.

[121] Damien Sulla-Menashe, Mark A. Friedl, and Curtis E. Woodcock. Sources of bias and variability in long-term Landsat time series over Canadian boreal forests. *Remote Sensing of Environment*, 177:206–219, 2016.

[122] John W. Tukey. Comparing Individual Means in the Analysis of Variance. *Biometrics*, 5(2):99–114, 1949.

[123] Fawwaz T. Ulaby and R. P. Jedlicka. Microwave Dielectric Properties of Plant Materials. *IEEE Transactions on Geoscience and Remote Sensing*, GE-22(4):406–415, July 1984.

[124] Fawwaz T. Ulaby, David G. Long, William Blackwell, Charles Elachi, Adrian Fung, Chris Ruf, Kamal Sarabandi, Howard A. Zebker, and Jakob van Zyl. *Microwave Radar and Radiometric Remote Sensing*. The University of Michigan Press, 2014.

[125] United States Geological Survey U.S.G.S. National Land Cover Database (NLCD) 2016 Land Cover - Alaska (ver. 2.0, July 2020), July 2020. Dataset.

[126] David Verbyla. Remote sensing of interannual boreal forest NDVI in relation to climatic conditions in interior Alaska. *Environmental Research Letters*, 10(12):125016, 2015.

[127] Jonathan A. Wang and Mark A. Friedl. The role of land cover change in Arctic-Boreal greening and browning trends. *Environmental Research Letters*, 14(12):125007, December 2019. Publisher: IOP Publishing.

[128] Shijin Wang and Xiaoqing Peng. Permafrost degradation services for Arctic greening. *CATENA*, 229:107209, 2023.

[129] Xiaoyun Wang, Shuhua Yi, Qingbai Wu, Kun Yang, and Yongjian Ding. The role of permafrost and soil water in distribution of alpine grassland and its NDVI dynamics on the Qinghai-Tibetan Plateau. *Global and Planetary Change*, 147:40–53, 2016.

[130] Zhijun Wang and Shusun Li. Detection of winter frost heaving of the active layer of Arctic permafrost using SAR differential interferograms. In *IEEE 1999 International Geoscience and Remote Sensing Symposium. IGARSS'99 (Cat. No.99CH36293)*, volume 4, pages 1946–1948 vol.4, June 1999.

[131] Melissa K. Ward Jones, Tobias Schwoerer, Glenna M. Gannon, Benjamin M. Jones, Mikhail Z. Kanevskiy, Iris Sutton, Brad St. Pierre, Christine St. Pierre, Jill Russell, and David Russell. Climate-driven expansion of northern agriculture must consider permafrost. *Nature Climate Change*, 12(8):699–703, 2022.

[132] U. Wegmuller, C. Werner, T. Strozzi, and A. Wiesmann. Ionospheric Electron Concentration Effects on SAR and INSAR. In *2006 IEEE International Symposium on Geoscience and Remote Sensing*, pages 3731–3734, July 2006. ISSN: 2153-7003.

[133] James Wickham, Stephen V. Stehman, Daniel G. Sorenson, Leila Gass, and Jon A. Dewitz. Thematic accuracy assessment of the NLCD 2016 land cover for the conterminous United States. *Remote Sensing of Environment*, 257:112357, May 2021.

[134] Elizabeth Wig, Roger Michaelides, and Howard Zebker. Fine-Resolution Measurement of Soil Moisture From Cumulative InSAR Closure Phase. *IEEE Transactions on Geoscience and Remote Sensing*, 62:1–15, 2024.

[135] Elizabeth Wig, Roger Michaelides, and Howard Zebker. Measuring Changes in Vegetation Moisture from Insar Closure Phase Time Series. In *IGARSS 2024 - 2024 IEEE International Geoscience and Remote Sensing Symposium*, pages 11479–11481, July 2024. ISSN: 2153-7003.

[136] Elizabeth Wig, Kevin Schaefer, Roger Michaelides, Richard Chen, Leah K. Clayton, Brittany Fager, Lingcao Huang, Andrew D. Parsekian, Howard Zebker, Yingtong Zhang, and Yuhuan Zhao. Permafrost Dynamics Observatory: 3. Remote Sensing Big Data for the Active Layer, Soil Moisture, and Greening and Browning. *Earth and Space Science*, 12(1), 2025.

[137] San Jose State University Wildfire Interdisciplinary Research Center. Fuel Moisture Repository Webportal.

[138] S A Wolfe, E Kotler, and F M Nixon. Recent warming impacts in the Mackenzie Delta, Northwest Territories, and northern Yukon Territory coastal areas. Technical Report 2000-B1, Geological Survey of Canada, Ottowa, Ontario, 2000.

[139] Chonggang Xu, Nate G. McDowell, Rosie A. Fisher, Liang Wei, Sanna Sevanto, Bradley O. Christoffersen, Ensheng Weng, and Richard S. Middleton. Increasing impacts of extreme droughts on vegetation productivity under climate change. *Nature Climate Change*, 9(12):948–953, December 2019. Publisher: Nature Publishing Group.

[140] H.A. Zebker and J. Villasenor. Decorrelation in interferometric radar echoes. *IEEE Transactions on Geoscience and Remote Sensing*, 30(5):950–959, September 1992.

[141] Howard A. Zebker. User-Friendly InSAR Data Products: Fast and Simple Timeseries Processing. *IEEE Geoscience and Remote Sensing Letters*, 14(11):2122–2126, November 2017.

[142] Howard A. Zebker. Insar Mission-Level Products on Demand - do we Need Range-Doppler? In *IGARSS 2018 - 2018 IEEE International Geoscience and Remote Sensing Symposium*, pages 68–71, July 2018. ISSN: 2153-7003.

[143] Howard A. Zebker and Richard M. Goldstein. Topographic mapping from interferometric synthetic aperture radar observations. *Journal of Geophysical Research: Solid Earth*, 91(B5):4993–4999, 1986. _eprint: https://onlinelibrary.wiley.com/doi/pdf/10.1029/JB091iB05p04993.

[144] Howard A. Zebker, Scott Hensley, Piyush Shanker, and Cody Wortham. Geodetically Accurate InSAR Data Processor. *IEEE Transactions on Geoscience and Remote Sensing*, 48(12):4309–4321, December 2010.

[145] Howard A. Zebker, Paul A. Rosen, Richard M. Goldstein, Andrew Gabriel, and Charles L. Werner. On the derivation of coseismic displacement fields using differential radar interferometry: The Landers earthquake. *Journal of Geophysical Research: Solid Earth*, 99(B10):19617–19634, 1994. _eprint: https://onlinelibrary.wiley.com/doi/pdf/10.1029/94JB01179.

[146] Howard A. Zebker, Paul A. Rosen, and Scott Hensley. Atmospheric effects in interferometric synthetic aperture radar surface deformation and topographic maps.

Journal of Geophysical Research: Solid Earth, 102(B4):7547–7563, 1997. _eprint: https://onlinelibrary.wiley.com/doi/pdf/10.1029/96JB03804.

[147] Michael Zemp. GCOS 2022 Implementation Plan. *World Meteorological Organization*, 85, 2022. Publisher: World Meteorological Organization.

[148] T. Zhang, J. A. Heginbottom, R. G. Barry, and J. Brown. Further statistics on the distribution of permafrost and ground ice in the Northern Hemisphere 1. *Polar Geography*, 24(2):126–131, 2000.

[149] Yingtong Zhang, Curtis E. Woodcock, Paulo Arévalo, Pontus Olofsson, Xiaojing Tang, Radost Stanimirova, Eric Bullock, Katelyn R. Tarrio, Zhe Zhu, and Mark A. Friedl. A Global Analysis of the Spatial and Temporal Variability of Usable Landsat Observations at the Pixel Scale. *Frontiers in Remote Sensing*, 3, 2022.

[150] Yongyong Zhang, Tyson E. Ochsner, Christopher A. Fiebrich, and Bradley G. Illston. Recalibration of Sensors in One of The World's Longest Running Automated Soil Moisture Monitoring Networks. *Soil Science Society of America Journal*, 83(4):1003–1011, 2019.

[151] Yujie Zheng, Heresh Fattahi, Piyush Agram, Mark Simons, and Paul Rosen. On Closure Phase and Systematic Bias in Multilooked SAR Interferometry. *IEEE Transactions on Geoscience and Remote Sensing*, 60:1–11, 2022.

[152] Simon Zwieback, Scott Hensley, and Irena Hajnsek. A Polarimetric First-Order Model of Soil Moisture Effects on the DInSAR Coherence. *Remote Sensing*, 7(6):7571–7596, June 2015.

[153] Simon Zwieback, Scott Hensley, and Irena Hajnsek. Soil Moisture Estimation Using Differential Radar Interferometry: Toward Separating Soil Moisture and Displacements. *IEEE Transactions on Geoscience and Remote Sensing*, 55(9):5069–5083, September 2017.

[154] Simon Zwieback, Xingyu Liu, Sofia Antonova, Birgit Heim, Annett Bartsch, Julia Boike, and Irena Hajnsek. A Statistical Test of Phase Closure to Detect Influences on DInSAR Deformation Estimates Besides Displacements and Decorrelation Noise: Two Case Studies in High-Latitude Regions. *IEEE Transactions on Geoscience and Remote Sensing*, 54(9):5588–5601, September 2016.

[155] Simon Zwieback and Franz J. Meyer. Top-of-permafrost ground ice indicated by remotely sensed late-season subsidence. *The Cryosphere*, 15(4):2041–2055, April 2021. Publisher: Copernicus GmbH.